[redacted]

Department of Physics
UNIVERSITY OF NEW HAMPSHIRE
Durham

MEASUREMENTS OF IONOSPHERIC CURRENTS

BY

NELSON CHARLES MAYNARD

B. S. in E. E., University of New Hampshire, 1950

M. S., Massachusetts Institute of Technology, 1962

A THESIS

Submitted to the University of New Hampshire

In Partial Fulfillment of

The Requirements for the Degree of

Doctor of Philosophy

Graduate School

Department of Physics

April, 1966

AN ABSTRACT OF

MEASUREMENTS OF IONOSPHERIC CURRENTS

Eight Nike-Apache sounding rockets were instrumented to investigate the vertical current distribution of the equatorial electrojet over India and off the coast of Peru, to investigate the vertical current distributions of the S_q current system at low latitudes off the coast of Peru, to determine if the lunar current system is separate from, or part of, the S_q system, and to correlate these measurements with simultaneous electron density measurements. Four rockets were launched near the dip equator from the Thumba Equatorial Rocket Launching Site near Trivandrum, India. The other four were launched off the coast of Peru, two near the dip equator (UNH 65-4 and UNH 65-5) and two to the north (UNH 65-2 and UNH 65-3), from the USNS Croatan, as part of the NASA Mobile Launch Expedition. A proton magnetometer measured the magnetic field, and a simple D.C. Langmuir probe monitored electron density.

A night flight over India (UNH 64-4) showed the effect of nighttime currents there to be less than 10γ. Other flights into the electrojet from India (UNH 64-1, UNH 64-2, and UNH 64-3) and from Peru (UNH 65-4 and UNH 65-5) indicated that the electrojet is an intense layer of current centered about 109 km with a more diffuse tail extending to higher altitudes (130 km in India; 135 km in Peru). The vertical distribution is thicker and centered higher than that found in previous measurements. A second layer may exist, centered between 140 and 145 km near the center of the electrojet, although evidence is not conclusive. Taking into account the finite width of the electrojet, the ratio, in India, of the contribution of the ionospheric currents at the ground to the total change in magnetic field on the ground is approximately 2/3. Since no reverse currents were observed on the flights at the time of maximum negative effect of the lunar current system (UNH 64-3)and UNH 65-4), it appears that the lunar system is either a modulation of the normal current, or that it may exist at a higher altitude (unlikely because of lower conductivity).

Maximums of electron density correlated with maximums of current density, although the reverse was not always evident. Evidence was found that the effect of the magnetic field on the Langmuir probe is dependent upon the length of the probe in the direction of the magnetic field.

It was found that the low latitude S_q currents can exist in two layers, one centered at 100 km and the other at 120 km (UNH 65-2). A reverse or negative current centered at the height of the maximum electrojet current (which may have been a return current from the electrojet) was observed to exist close to the electrojet (UNH 65-3).

ACKNOWLEDGMENTS

The author wishes to express his appreciation to Dr. Laurence J. Cahill, Jr., at whose suggestion this research was initiated, and under whose direction and patient guidance it was carried out.

A note of thanks is given to those who have supplied data, calculations and circuit design in support of this work, as mentioned in the text, and to the members of my thesis committee. Also, several informative discussions were held with Dr. M. Sugiura.

In the India launchings assistance is acknowledged from S. B. Marshall, III, of the UNH Physics Department, from T. S. G. Sastry and U. D. Desai of the Physical Research Laboratory, Ahmedabad, India, from the personnel of the Thumba Equatorial Rocket Launching Station under the direction of H. G. S. Murthy, and from R. Conrad and others of the Sounding Rocket Branch of the Goddard Space Flight Center.

Assistance in the Peru launchings is acknowledged from P. E. Lavoie of the UNH Physics Department and from the many people from Wallops Island and the Sounding Rocket Branch at the Goddard Space Flight Center who made up the shipboard launch crew under the direction of Robert Long.

The author would also like to express his appreciation to the staff of the UNH Physics Department who have assisted in various ways. Karl Flanders assisted on many of the mechanical details. The drawings were done by Herbert Scheibel and the typing by Mrs. Phyllis Warnock.

This research was supported under NASA Grant NSG-33-60 and Contract NAS-5-3043.

TABLE OF CONTENTS

LIST OF TABLES

LIST OF FIGURES

CHAPTER I

INTRODUCTION

Daily variations in the earth's magnetic field are found to exist at observatories around the world. On magnetically quiet days these variations follow definite patterns related to the phase of the sun and the moon. The dynamo theory of ionospheric currents was long ago proposed by Stewart (1882) to explain daily S_q variations (correlated with the sun) in the earth's magnetic field. Two current loops (one in each hemisphere), fixed in relation to the sun, were proposed; daily variations at ground observatories result as the stations pass under the current systems (Figure 1); (see, for example, Chapman and Bartels, 1940; Maeda and Matsumoto, 1962). Currents in the northern loop flow counter-clockwise and those in the southern loop clockwise, contributing to a net west-to-east flow where they combine near the equator. The global ionospheric conductivity, depending on the magnetic field direction, collision frequencies, and the electron density, together with the global pattern of tidal winds, determine the resulting current density.

Stratification in the ionosphere restricts the currents to flow primarily in horizontal layers; thus, the tensor conductivity can be reduced to

$$\underline{\underline{T}} = \begin{pmatrix} \sigma_{xx} & \sigma_{xy} \\ -\sigma_{xy} & \sigma_{yy} \end{pmatrix} \qquad (1)$$

where $\underline{J} = \underline{\underline{T}} \cdot \underline{E}$

Here, $\underline{E}$ is the electric field and the earth's magnetic field is in the XZ plane (Z being the vertical axis).

The components of the conductivity tensor may be expressed as

$$\sigma_{xx} = \frac{\sigma_0 \quad \sigma_1}{\sigma_0 \sin^2 \phi + \sigma_1 \cos^2 \phi} \tag{2}$$

$$\sigma_{yy} = \sigma_1 + \frac{\sigma_2^2 \cos^2 \phi}{\sigma_0 \sin^2 \phi + \sigma_1 \cos^2 \phi} \tag{3}$$

$$\sigma_{xy} = \frac{\sigma_0 \sigma_2 \sin \phi}{\sigma_0 \sin^2 \phi + \sigma_1 \cos^2 \phi} \tag{4}$$

where ϕ is the angle between the magnetic field vector and the X axis or the dip angle, σ_0 is the direct conductivity along the magnetic field vector, σ_1 is the Pederson conductivity along the direction of the component of the electric field perpendicular to the B field, and σ_2 is the Hall conductivity in a direction perpendicular to both $\underline{E}$ and $\underline{B}$ (Baker and Martyn, 1953; Ratcliffe and Weekes, 1960). Each of these conductivities depends directly on the density of electrons. The components of the conductivity tensor have their maxima in the E region, making the region between 90 and 150 km the most probable location for current flow (Figure 2).

An anomaly called the equatorial electrojet (Chapman, 1951) occurs near the magnetic dip equator where ϕ goes to zero. There, the earth's magnetic field is horizontal and generally northward, while the electric field and principal current flow are horizontal and perpendicular to this. The Hall effect produces a vertical current flow which sets up a space charge, effectively canceling

out the Hall voltage. Equations (2) through (4) become

$$\sigma_{xx} = \sigma_o \tag{5}$$

$$\sigma_{xy} = 0 \tag{6}$$

$$\sigma_{yy} = \sigma_1 + \frac{\sigma_2^2}{\sigma_1} = \sigma_3 \tag{7}$$

The result is an enhanced current in the narrow region where the magnetic field is nearly horizontal (Baker, 1953). These currents are strongest near 1100 hours local time.

The lunar current system is similar to that of the general S_q system. Tides controlled by the moon have the same dynamo action in the ionosphere. This could create a low intensity modulation of the normal S_q current system. The ratio, S_q/L is smaller in summer than in winter and varies considerably from day to day, suggesting that the lunar current might be at a different altitude. During part of the day the lunar effect is negative with respect to the S_q system (Chapman and Bartels, 1940). This effect varies in time from day to day depending on the phase of the moon.

The lateral extent of these currents, especially that of the electrojet, has been studied from the analysis of ground measurements from stations all over the world (for example, Forbush and Casaverde, 1962; Onwumechilli, 1959; Ogbuehi and Onwumechilli, 1963 and 1964). The vertical distribution of current density can be determined only by rocket measurements. Rocket measurements of currents are made through precise determination of the magnetic fields produced by the currents (Vestine et al., 1947; Chapman, 1954; Cahill, 1964).

The first direct measurement of ionospheric currents was made of the electrojet near the equator by Singer, Maple, and Bowen (1951). Subsequent measurements of the electrojet near Jarvis Island in the Pacific indicated the possibility of a two-layered structure, with the lower layer between 100 and 110 km and the upper layer above 120 km (Cahill and Van Allen, 1958; Cahill, 1959). On these early flights the peak altitude of the rockets did not allow complete penetration of the current layers. Recently, detection of S_q currents has been made at Woomera, Australia (Burrows and Hall, 1965), and at Wallops Island, Virginia (Davis et al., 1965).

The purpose of the experiment reported here was four-fold:

1. to investigate the vertical current distribution of the electrojet over India and off the coast of Peru to a greater altitude than previously achieved,
2. to investigate the vertical current distribution of the S_q current systems off the coast of Peru,
3. to determine if the lunar current system is in a separate layer, or if it is a part of the S_q system, and
4. to correlate these measurements with simultaneous electron density measurements.

Four flights were launched from the southern tip of India, and four were launched from the USNS Croatan as part of the NASA Mobile Launch Expedition off the coast of Peru.

CHAPTER II

PHYSICAL BACKGROUND

Recognition of the existence of the earth's magnetic field dates back several centuries; however, it was 1833 when Gauss and others first established a magnetic observatory and made daily measurements. Systematic measurements at observatories around the world since that time have broadened the knowledge of the magnetic field. Recently, rocket and satellite measurements have added a third dimension to observational data.

These systematic measurements have led to the recognition of many classifications of variations in the geomagnetic field. These have been labeled according to the apparent cause of the variations. (For discussions of the earth's magnetic field and variations, see Chapman and Bartels, 1940, or Sugiura and Heppner, 1965).

The earth's magnetic field is believed to originate within its molten core. The interaction of thermodynamic fluid motions and electric currents could give rise to the earth's field (Elsasser, 1956). The earth's field can be expressed in the region exterior to the earth in a series of spherical harmonics with the magnetic dipole term being the dominant one. The expansion was first performed by Gauss, although many recalculations of the coefficients of the harmonics have been done since. Two of these - those of Leaton and Evans (Leaton, Malin, and Evans, 1965) and those of Finch and Leaton (1957) - have been used in this experiment, in later calculations of the magnetic field that the rockets would measure if

there were no ionospheric currents in the region of the flight.

Variations in the earth's magnetic field which are detected as year-to-year changes at an observatory are called secular variations. The overall pattern of these variations, as determined from averages of many years of data, shows that the dipole moment is decreasing, the general field pattern is drifting westward, and the dipole field is shifting northward (Sugiura and Heppner, 1965). These changes are attributed to changes of source of the main field in the earth's core.

Other fluctuations in the field are of much shorter durations, occurring on scales from days or hours to milliseconds. On some days, which are said to be quiet, the variations are smooth and regular. On others the changes are more irregular and these days are called active or disturbed. A certain type of highly disturbed condition is called a magnetic storm. Some variations have the period of the solar day and are classified by the letter S. Others have the period of the lunar day and are denoted by the letter L. A magnetic disturbance field is referred to by the letter D.

These general classes of variations are further broken down (see Sugiura and Chapman, 1960). The notation S_q refers to the solar variations under quiet magnetic conditions. If the average variation for the five most quiet days of the month is subtracted from the average of the five most disturbed days, the result is the SD variation (sometimes denoted S_D). This is called the disturbance daily variation. The magnetic storm or disturbance field is resolved into two parts, the D_{st} variation and the DS variation. If we call the

change in the field from quiet conditions to disturbed conditions df, the average value of df around a parallel of latitude at any time is denoted by D_{st} and is called the storm-time variation. The difference between df and D_{st} is called DS or disturbance longitudinal inequality. Thus, the geomagnetic axially symmetric part is called D_{st}, while the deviation from axial symmetry is called DS. The variation DS averaged with respect to the storm time over the storm days is equivalent to SD for those days.

The magnetic activity of a particular day is denoted by a number of character indices. The two most common of these are the K_p and A_p indices. K_p is the mean standardized K index from twelve observatories lying between 48° and 63° geomagnetic latitude (northern or southern). K indices are determined from the largest of the maximum ranges of the three field components over three-hour intervals. A quasi-logarithmic relation to the amplitude of the disturbance is used for K in order to include a wide range of activity in one-digit numbers. A corresponding linear amplitude index is a_p. A_p is derived from the average of 8 a_p values for one day over the observatories (see, for example, Davis and Sugiura, 1965).

The advent of the experimental discovery of the ionosphere and consideration of the effects of the geomagnetic field on the electrical conductivity led, in the 1920's to the concept of the currents (postulated as the source of these variations) flowing in the ionosphere. The layered structure of the ionosphere restricts the current flow in horizontal layers. Although S_q, L, and SD are believed to result from ionospheric currents, D_{st} is thought to result from a ring current flowing in the magnetosphere. There may also be

surface variations caused by the asymmetrical compression of the magnetosphere (Mead, 1964).

The atmosphere oscillates (due to gravitational forces) with a period of one-half of a solar or lunar day. In the atmosphere the solar semi-diurnal component is larger than the lunar - opposite from ocean tides. In the atmosphere there exist also solar heating and rapid variations of density with height. The resulting winds in the ionosphere have been roughly measured by examining the drift of vapor clouds released by a rocket and also by observation of movement of ionospheric irregularities (see Nordberg and Rasool, 1965). These large scale motions of the atmosphere and the ionosphere (mainly horizontal) in the presence of the earth's magnetic field induce an electric field perpendicular to the magnetic field and to the velocity of the air. The electric field, or dynamo field (field strength of the order of millivolts per meter) is able to drive a current system sufficient to account for the S_q magnetic variations in the ionosphere where the conductivity is large.

The amount of current driven by the dynamo field is dependent on the conductivity. As discussed in the introduction, the conductivity is a tensor quantity in the presence of a magnetic field. The various components of the tensor conductivity have their maxima in the E region of the ionosphere between 90 and 140 km. The conductivity is directly proportional to the electron density and is also dependent upon the mass and the collision frequency. The component of electric field perpendicular to the magnetic field produces a current, one component of which (along the electric field) results from the Pederson conductivity σ_1, and the other (perpendicular to both B and E) is in proportion to the Hall conductivity σ_2. Both of these

transverse conductivities depend on the angular gyro frequency of the particle and are smaller than the direct conductivity along the field line by factors of $\left[\nu^2/\left(\omega^2 + \nu^2\right)\right]$ and $\left[\nu\omega/\left(\omega^2 + \nu^2\right)\right]$, respectively, (where ν is the collision frequency and ω is the gyro frequency). Depending on the location and the coordinate system, these conductivities combine into expressions for the conductivity tensor terms as expressed in equations (2) through (4) on page 2.

Considering the dynamo field and the conductivity, one obtains the S_q current systems. The idealized model produces a pattern of current that remains stationary under the sun. A vortex of current is created in each hemisphere (Figure 1). Although the current at any point is relatively small, the total current flowing across the meridian plane between the two foci is about 120,000 amperes (Sugiura and Heppner, 1965). The current intensities in the summer hemisphere are greater than those in the winter hemisphere. These currents have recently been detected on rocket probes (as previously mentioned) in the E layer. One should note that the overhead currents induce sub-surface currents which also contribute to the ground magnetic variation. The induced current is thought to account for about one-third of the total effect.

$\underline{V} \times \underline{B}$ fields generated at middle and high latitudes by the patterns of winds combine to create an electric field in the equatorial region. This field is eastward near noontime. At the magnetic dip equator the magnetic field is horizontal and northward. The horizontal stratification of the ionosphere allows the Hall current to polarize the medium. The result is an area of enhanced conductivity with σ_3 (equation (7)), the Cowling conductivity, being the most

important. The effect is found to decrease rapidly away from a narrow belt at the dip equator called the electrojet. Recent work by Sugiura and Cain (1965) shows how the conductivities vary with latitude and height in the areas of the electrojet. Magnetic variations from the electrojet are much larger in Huancayo, Peru, than in other parts of the world. This is explained by a longitudinal variation in conductivity when the differences in the total magnetic field at the various observatories are considered (Sugiura and Cain, 1965).

Lunar tides also create a dynamo action (see Matsushita, 1962). The coupling of the vertical magnetic field with the lunar tidal wind system creates a current system which has the period of a lunar half-day. Effects that distinguish the lunar system from the S_q current system are: the foci are located higher in latitude in summer than in winter, the summer intensity is about three times that of winter, the intensity also varies greatly with the lunar phase. The variation changes characteristics from day to day, as the moon changes phase. The effect of the lunar current on the sunlit side is about one-tenth that of S_q. The amplitude of L over the dip equator is abnormally large from the same causes that create the electrojet. However, the amplification at the dip equator is larger for L than it is for S_q. While the lunar variations seem to be caused by ionospheric currents, as the S_q variations, the differences between the two lead one to look also for a separate current structure. Vestine (1960) has stated that S_q and L must be in different layers, since the changes with season, magnetic activity, and solar phenomena are not the same.

In the polar region the DS magnetic variations can be grouped into two classes: large changes, occurring over a large part of the auroral zones, with a time scale of several hours or longer, and rapid (and often large) fluctuations which are regional in character. The most notable DS feature is accounted for by an intense auroral electrojet. The detailed structure is not well known; however, the auroral electrojet is thought to be usually very narrow. Return currents complete this pattern and account for variations across the poles and at lower latitudes. The SD variation is an average of the DS variations. At low latitudes it may be a storm-time enhancement of the S_q system of currents. The dynamics of the magnetosphere must also be considered. Although at low latitudes the coupling to the ionosphere is weak, it may be dominant in the polar regions. (Sugiura and Heppner, 1965).

The equatorial ionosphere exhibits many characteristics which are different from the temperate zone ionosphere. Radio soundings of the ionosphere (ionograms) sometimes exhibit a spread appearance in the F-region echoes (spread F). This phenomenon has been associated with magnetic field-aligned irregularities in the electron density, although no definite physical cause has been defined (Aikin and Bauer, 1965). Sporadic E ionization is also characterized by field-aligned irregularities in the regions within five degrees of the dip equator. Equatorial E_s appears about 95% of the time on oblique incidence soundings. It has been suggested that the irregularities from which the E_s arises are present throughout the regions in which the electrojet flows (Egan and Peterson, 1962; Bowles and Cohen, 1962). Evidence from the study of equatorial

sporadic E indicates that the electrojet irregularities extend in a region from 100 to 107 km in height, that they are plane wave fronts parallel to the magnetic lines of force, that the irregularities are at least 200 meters in length along the magnetic field line, and that equatorial slant sporadic E (slanted trace on the ionogram) is from the same source as equatorial sporadic E irregularities and results from echoes in the equatorial plane. The mechanism of the instability has been suggested by Farley (1963) to be the two-stream instability. A plasma consisting of two or more interpenetrating streams of charged particles will be unstable if the mean velocity of the particles in one stream is sufficiently great, relative to the mean velocity in the other stream. In this case longitudinal waves will grow spontaneously. This simple picture is complicated in the ionosphere by collisions and the magnetic field, although the result is similar. VHF scattering measurements have been used to probe these effects in the lower E regions (Cohen and Bowles, 1963; Bowles et al., 1963). Recently, evidence has also been presented for the existence of VHF echoes at 140 to 150 km (Balsley, 1964; 1965).

From the above discussion it is evident that many characteristics of the ionosphere need to be verified and explained. The use of a rocket allows a measurement to be made directly within the ionosphere. Some of the pertinent questions that measurement of ionospheric currents can help to answer are listed below:

1. What is the vertical distribution of current density in the ionosphere?
2. What are the vertical profiles of conductivity and electric field which are directly related to the currents?

3. Do the L and SD magnetic variations stem from currents in layers separate from the S_q layer, or are the effects from a combined current in the same layer or layers?
4. Do measurements of electron density (which is directly related to conductivity) correlate with ionospheric current measurements?
5. How well do the ionospheric measurements of currents compare with ground magnetic measurements, and from this, how large are the induced sub-surface current effects?
6. What is the actual width of the electrojet, and how does the vertical current density profile vary over this width?
7. What is the cause of the longitudinal variation of the equatorial electrojet?
8. What correlations exist between observed electron density phenomena, such as equatorial sporadic E and the equatorial electrojet?
9. What are the structure, cause, and effects of ionospheric currents in the auroral regions?

In these two series of flights (from India and off the coast of Peru), answers were sought to questions 1, 3, 4, and 5, in the equatorial regions. Information pertaining to questions 2, 6, 7, and 8, was obtained in some cases.

CHAPTER III

EXPERIMENTAL DESIGN

A. General

The UNH rocket magnetometer payload consists of the two main experiments, the proton magnetometer and the Langmuir probe, and three supporting experiments, a barometric pressure switch and a radiation chamber densitometer (measuring air pressure) for trajectory determination, and a magnetic aspect sensor for rocket aspect information. The payload design and construction were a team effort of the University of New Hampshire Physics Department. A. B. White and S. B. Marshall, III, were responsible for much of the design, although they drew on earlier work done at UNH and elsewhere. Complete responsibility for the success of the experimental flights was borne by the author under the direction of L. J. Cahill, Jr., principal investigator, NASA Grant NsG-33-60 and Contract NAS 5-3043. A block diagram of the payload is found in Figure 3.

The signal from the magnetometer sensor is amplified and fed directly to the mixer for telemetering to the ground. The magnetic aspect sensor modulates a 22-kc subcarrier oscillator (SCO), while the densitometer information modulates a 40-kc SCO. The baroswitch is also used to switch the Langmuir probe amplifiers from a calibration resistor to the probe. The Langmuir information is put on a 70-kc SCO channel. The signals are combined in the mixer, amplified and fed into the transmitter. Information is

radioed back to ground through the circularly-polarized quadrupole antennas at the base of the payload.

In designing the physical layout of the payload (Figure 4), the prime consideration was to minimize the magnetic field from the payload at the magnetometer sensor location. A payload field less than 2γ was achieved. Each unit also had to function after large shocks and vibrations from the firing of the rockets. The magnetometer sensor was placed as far as possible up into the nose cone to separate it from the electronics. A fiberglass deck structure and housing were used, since any conductive loops around the magnetometer coil would destroy the signal. Each experiment was mounted on one or two decks which could be plugged, as separate units, into the raceway containing the interconnecting wiring harness (Figure 5). Interchangeability of decks between payloads was desired for convenience in field operations.

B. The Proton Magnetometer

1. Theory

The proton precession magnetometer of Packard and Varian (1953), and Waters (1955), (also Waters and Francis, 1958) is easily adaptable to rocket measurements. The sensor unit is simple and rugged, and the instrument requires no in-flight calibration, since the measurement is dependent upon nuclear constants.

If a sample of liquid, rich in hydrogen nuclei, is subjected to an external polarizing magnetic field several orders of magnitude larger than the earth's magnetic field, the spin axes of the protons in the sample will be aligned along the polarizing

field. Then, if the polarizing field is suddenly reduced to zero, the protons will commence to realign with the earth's field, and while so doing will freely precess about the earth's field. A small AC voltage at the precession frequency will be induced in any coil of wire around the sample.

The earth's magnetic field is related to the precession frequency by the Larmor relationship

$$B = \frac{2\pi f_p}{\gamma_p} \tag{8}$$

where f_p is the precession frequency, and γ_p ($2.67513 \pm .0002 \times 10^4$ radians/sec. gauss), the gyromagnetic ratio of the nucleus (Driscoll and Bender, 1958). Since γ_p is known to within two parts in 10^5, measurement of the precession frequency may limit the absolute accuracy of the measurement.

The same coil can be used for signal pickup and for establishing the polarizing field. A 700-turn coil, with several amperes polarizing current, produces a precessing signal of a few microvolts. The output voltage can be expressed by

$$V = 4\pi\ K\ N\ A\ X\ B_o\ \gamma_p\ B_e \cdot \sin^2\theta \cdot e^{-t/T^2} \sin(\gamma_p B_e t) \cdot 10^{-6} \text{ volts} \tag{9}$$

(Cahill and Van Allen, 1956), where

K = goemetric factor

N = number of turns

A = cross sections of sample

X = paramagnetic susceptibility of the protons

B_o = polarizing field

γ_p = geomagnetic ratio of the proton

B_e = earth's field

Θ = angle between coil axis and earth's field

T_2 = transverse relaxation time

t = time in seconds

Note that the amplitude of the signal falls off as $\sin^2\Theta$; hence, if the coil is aligned with the earth's field, there will be no signal. Also, the phase coherence of the precessing nuclei will decrease in time resulting in an exponential decay of the signal. The polarize cycle must be longer than the relaxation time to allow the protons to approach complete alignment with the polarizing field. In order to obtain a good signal, the polarization field must be removed in a time that is short compared to the period of one cycle of the precession frequency. In addition there should be no magnetic field gradients across the sample, since the resulting difference in precession frequency will destroy the coherence of the signal. A precession frequency of approximately 2000 cps is obtained in a 0.5 gauss (50,000 γ) field.

The accuracy to which the gyromagnetic ratio of the proton is known allows absolute measurement to within one gamma. Better relative accuracy can be obtained, depending only on precision of frequency measurement. Noise in the signal has been the limiting factor in frequency measurement with the miniature rocket magnetometer.

2. Design and Operation

A proton magnetometer designed for operation in rockets must meet the following requirements:

1. It must be able to withstand severe shock and vibration.
2. The low level (microvolt) of the precession signal demands considerable amplification to attain a volt-level signal for telemetry. The signal-to-noise ratio must be kept above two to one for precise frequency measurements.
3. The sensor magnetometer, electronics and the remainder of the payload must be free from magnetic materials which would create a field at the sensor.
4. Measurements must be made as frequently as possible without sacrificing the precision of frequency determination, since the rocket is traveling more than 1 km/sec during portions of the flight.

The specific magnetometer design to be described is principally the work of W. B. Dickinson. The design was based on the earlier work of Cahill (1956), Waters (1958) and Packard and Varian (1954). Dickinson's design was modified and improved as indicated by performance in early rocket flights.

Figure 6 depicts the block diagram of the magnetometer used on the University of New Hampshire flights. The programmer controls the relays, which alternately connect the amplifier or the polarizing supply to the sensor coil. During the polarizing period (about 0.7 sec), the polarizing batteries send a current of 4 amperes through the coil. The polarizing current is then

turned off, and the coil is connected during the read period of 0.7 second, to the high gain preamplifier. The signal from the coil is amplified to the 10 milli-volt level. In the tuned main amplifier the signal is amplified to 4 volts for mixing with the SCO signals and direct modulation of the FM transmitter.

a) Sensor Coil

The sensor coil (Figure 7) consists of ten layers, 70 turns each layer, of #16 wire, wound on a fiberglass tube and held in place by phenolic discs. A polyethylene sample bottle fits tightly inside the coil form. Kerosene, which has a relaxation time of about 0.7 second, is used as the sample. Water could be used, but it has a two-second relaxation time, making the repetition rate of the measurements too slow.

An electrostatic shield (Figure 8) completely encloses the coil to reduce noise pickup. This shield is made from copper-plated fiberglass board by etching away narrow strips of copper. Care must be taken to make sure that there are no complete conductive loops around the coil, as these will destroy the signal. The unit is then encased in foam and an outer protective cover.

b) Preamplifier Assembly

The electronics for the magnetometer is divided into two packages, one containing the preamplifier, programmer, and associated relays (Figure 9), and the other containing the tuned main amplifier.

The programmer is a standard astable multivibrator with the RC combinations, C_1R_2 and C_2R_3, adjusted so that the circuit

will remain in each state about 0.7 second. The output from the collector of TR_2 triggers a switch (TR_3) which controls the relays.

Relay RY_1 switches the polarizing power to the coil and controls the operation of RY_2. RY_2 is used in switching the amplifier to the coil and also to supply a 220 Ω resistor across the input to the amplifier during the polarize cycle, when the coil is disconnected, to prevent oscillation. Relay RY_2 is a G.E. 352791G200A5 Relay. RY_1, a Sigma 33RJ490FGSIL, was chosen for its low contact resistance, hence its ability to handle very small signals along with its high current rating (2 amps). Since it produces a strong magnetic field, it was necessary to enclose it in a MU-metal shield. A relay meeting all requirements and rated at a higher current was desirable, but it was not available. The capacitor across RY_2 delays the operation of RY_2 for about 20 milliseconds to allow suppression of transients from the switching. Contacts of RY_2 are arranged to cancel transients resulting from contact potentials in the relay.

To dissipate the inductive switching transient from the coil, a clipping network is employed across the coil. The diode CR_4, back-biased during the polarization, conducts the energy from the transient into C_4, which in turn dissipates it in R_5.

The preamplifier is a very low-noise tuned amplifier with a gain of about 3000. Because of the very low level signal, RCA 2N220, low-noise germanium transistors were used in all three stages to keep noise generation in the amplifier itself at a minimum.

The first stage is a common emitter, transformer-coupled,

tuned amplifier. The Triad TY55X (T-1) transformer is used to match the impedance of the coil to the input impedance of TR-1. Resistor R_{16} serves to bias the emitter and to limit the collector-to-emitter current to the RCA recommended value of 400 μa for lowest noise operation. Tuning is accomplished through series resonance of the secondary of T-1 and the base emitter junction capacity of TR-1. This is aided by C_{12} and R_{14}. Resistor R_{14} adjusts the bandwidth, while C_{12} shifts the frequency. For wide changes in frequency it is necessary to adjust R_8 and R_9, thus changing the biasing and therefore the junction capacity. In practice it was found best to leave out R_{14} and C_{12} during construction and to use substitution boxes to tune roughly to the desired frequency and bandwidth. Typical values for R_{14} and C_{12} are 180 Ω and 0.5 μf.

Transformer T_2 is used to couple the high output impedance of TR-1 to the low input impedance of TR-2. The second stage is a grounded emitter, untuned, voltage amplifier. Capacitor C_{15} further shapes the passband and helps the signal-to-noise ratio by limiting the high frequency response of the amplifier. This also served to limit interference from the transmitter power convertor which operated at about 3200 cps.

The third stage is an emitter follower to provide low output impedance and isolation of the other stages from loading effects.

Resistor R_{10} and Capacitors C_8 and C_4 stabilize the supply voltage to each transistor and decouple any signal voltages appear-

ing on the supply line that could cause feedback and oscillation. Bias for the circuit is -12v.

Printed-circuit construction was used for the circuitry, and the board was encased in foam for shock and vibration protection. A copper box covered the foamed circuit and served as an RF shield.

Wave traps were used on all signal leads entering and leaving the box to reduce RF interference. They were made from a ceramic 10-μμf capacitor with three turns of wire wrapped around (in parallel with) the capacitor. The traps were tuned to the transmitter frequency by changing the spacing between turns. The high gain tuned amplifier was subject to oscillation when modulating the FM transmitter. The feedback apparently was through leakage of the RF signal into the circuit boxes and demodulation there. It is recommended for future flights that these traps be in all leads, power leads as well as signal leads, entering the copper box. Oscillation can also occur if the sensor coil is improperly connected to the first stage of the amplifier.

c) Main Tuned Amplifier

Figure 10 shows the schematic for the main amplifier. The four-stage amplifier was designed to amplify the output of the preamp to the 4-volt level necessary to feed into the telemetry system and to further reduce noise on the signal. Resistor R_1 controls the overall gain of the system and is used to adjust the output to the desired level for feeding into the telemetry system. Capacitor C_2 is used to limit further the high

frequency response of the circuit.

The first stage (TR_1) is a common emitter voltage amplifier. The output is capacitive-coupled into the second stage. The second stage is identical with the first stage with the exception of R_8. This stage is meant to be driven into saturation and cut-off to clip the signal. R_8 is used to adjust the peak voltage value of saturation and cut-off. R_6 and R_7 are adjusted to obtain symmetrical clipping. RCA 2N217 germanium transistors are used throughout.

Variations in amplitude of the output signal are effectively removed by clipping. Preservation of the amplitude of the signal is not necessary, since all the information is contained in the frequency. (The output at the collector of TR_2 should be a square wave of amplitude 2 volts, peak to peak). The clipping lessens the effect of noise in the signal and thus effectively lengthens the useful portion of the exponentially decaying signal. Clipping continues until the precession signal has decayed below the level set by R_8, and the output will be of constant amplitude until this time.

The output of the second stage is directly coupled into TR_3, which is used in an emitter follower configuration for isolation and impedance matching into the band-pass filter. The band-pass filter, designed from equations given by Terman (1943), serves to select the fundamental frequency from the square wave and to further remove noise of frequencies outside the band-pass region. The center frequency can best be adjusted by varying C_7 and C_9, while the band width is set by R_{12}. In practice each adjustment will slightly affect the other. The inductors used are high Q, toroidal coils, manufactured by Collins Radio Company.

The final stage is an emitter follower used to provide a low output impedance and to match to the output impedance of the band-pass filter. The signal is capacitor-coupled to the telemetry system. The same power supply is used for the main amplifier as was used for the preamplifier. Large tantalum capacitors keep the supply impedance low and prevent feedback between stages and between the amplifiers. The amplifier was constructed on a printed circuit board and encased in foam inside a copper box (Figure 11). As in the preamplifier wave traps were employed on the signal leads to reduce RF interference.

3. Tuning and Associated Problems

These payloads have been flown at several different sites around the world. At each place the field is different, so the magnetometer must be tuned to the magnetic field at the launching site. The bandwidth must be wide enough to accommodate the expected field variations during flight. The UNH magnetometers have been tuned with a bandwidth of 400 cycles, and with the center of the band set to give optimum performance near the 100-km point of the flight, the region where currents are most probable.

Tuning must be done in two stages. The individual units must be tuned and then retuned when combined. The preamplifier is tuned by inducing a variable-frequency oscillator signal in the pickup coil with one turn of wire, while the coil is in a permalloy shield (to prevent 60-cycle pickup and other noise). Care must be taken to keep the input signal below 50 μa, so as not to overdrive the amplifier. For an overall bandwidth of 400 cycles, the preamplifier is adjusted to obtain a bandwidth of 600 to 700 cycles. For initial

tuning of the main amplifier, a 10-mv audio-oscillator signal is introduced at the input, and the filter is adjusted as previously described to obtain the desired 400-cycle bandwidth. The units are then connected together, with the oscillator signal feeding into the coil, for a system bandwidth check. Minor adjustments may have to be made to the main amplifier filter for the desired band-pass shape. For signals in the center of the band-pass, 4 to 5 volts output is obtainable with a precession signal-to-noise ratio of three or four to one.

As was noted in the theory of operation, gradients in the field over the dimensions of the sensor will destroy the signal. One can always check the output to be sure that it is a precession signal by holding a steel wrench next to the sensor, thus destroying the signal. For shipboard launchings the large field gradients caused by the steel hull prevent observation of the magnetometer signal until the rocket has left the launcher.

Since the majority of testing is done in Durham, some means must be created to set up a magnetic field the same as that to be encountered in flight. Included in the University's Magnetic Field Observatory is a Fanselau coil system for establishing any desired field in the range between zero and one gauss to an accuracy of one gamma. A less elaborate, but effective system was used to test the instruments in the field. It consists of five coils (turns ratio 19-4-9-4-19) equally spaced on a cubical coil form (Rubens, 1945). If the axis of the coils is aligned with the main component of the field, the field can be canceled or strengthened to any desired level. A four-foot diameter cube is of sufficient size.

C. Langmuir Probe

1. Theory

In the early 1920's Langmuir and his colleagues developed the theory of probes protruding into a plasma (Langmuir and Mott-Smith, 1924; Mott-Smith and Langmuir, 1926). Recently, Langmuir probes have been used to investigate electron density in the ionosphere (see, for example, Smith, 1963a)

In the treatment of the probe, negative and positive ions are neglected, as their contribution to the probe current is negligible. The random current density to the probe, for a single probe in a plasma, may be expressed by

$$j_e = N_e \left(\frac{e\bar{V}_e}{4} \right) \tag{10}$$

where N_e is the electron density

e is the electronic charge

and $\bar{V}_e$ is the mean electron velocity

If we assume a Maxwell distribution (and thus, thermal equilibrium) for the electrons,

$$\bar{V}_e = \left(\frac{8kT_e}{m_e} \right)^{1/2} \tag{11}$$

where

T_e is the electron temperature

m_e is the electron mass

k is the Boltzman constant

When the probe is negative with respect to the plasma, only electrons with energies greater than the retarding potential will strike the probe. The current may be expressed by

$$j = j_e \exp\left(\frac{eV}{kT_e}\right) \tag{12}$$

where V is the retarding potential.

Note that in this case the current is independent of the electrode configuration, and the slope of the current voltage characteristic is proportional to the electron temperature.

For accelerating potentials the size and shape of the electrodes becomes important. The two limiting cases are a plane where

$$j = j_e \tag{13}$$

and a small sphere where

$$j = j_e \left(1 + \frac{eV}{kT}\right) \tag{14}$$

For all other geometries the currents fall between these two limits. For any given configuration the current is proportional to the electron density, if we neglect changes in electron temperature.

In an actual experiment it is easier to use two probes and measure the current voltage characteristic of the pair. If the area ratio of the two probes is large, the smaller of the probes can be treated as a single probe, and the larger serves to establish a constant reference potential. To obtain a large area ratio in rocket investigations of the ionosphere, a small tip probe is used for the

small electrode, and the rocket motor housing constitutes the large electrode.

Since knowledge of the fine structure of the electron density was desired for correlation with the magnetic field measurements, the probe was kept in the DC mode as much as possible. The use of a constant DC potential on the probe is difficult to justify theoretically, but it is simple to achieve experimentally. The results agree with those obtained by other methods (Smith, 1963a).

2. Design

The area of prime interest for comparison of electron density and electric current measurements (by magnetometer) was the E region of the ionosphere. In order to accommodate the expected changes of electron density in this region, two linear scales were used, covering two orders of magnitude instead of the usual logarithmic amplifier. The probe amplifier was switched periodically between the two ranges. Since the rocket travels at speeds greater than 1 km/sec in the lower E region, it was necessary to switch rapidly between scales to avoid losing data. A repetition rate of five cycles per second was chosen - one-tenth of a second for each scale. Since continuous measurements were desired, the amplifiers were DC-coupled and had to be as free as possible from changes in the zero level of the DC output. It was also necessary to find a means of switching that would not change the level of the DC signal. Overall requirements of a magnetically clean payload also had to be met.

Design, construction, and testing of the Langmuir probe were done by the author. Reference to the work of Dr. L. G. Smith (private communication) was most helpful. Electronic circuits

used in amplification and switching are an original contribution of the author in this application.

Figure 12 shows a block diagram of the Langmuir probe electronics. The multi-vibrator controls the amplifiers which feed into a common output. The signals are fed to the amplifiers from the sensor. The multi-vibrator output is scaled by a factor of eight to drive a one-shot multi-vibrator. This in turn triggers a ramp generator which applies a ramp voltage to the probe, sweeping from -3 volts to a DC level of 2.7 volts. This ramp allows measurement of the electron temperature. When the probe is negative to the plasma, the electron temperature is inversely proportional to the slope of the current voltage characteristic of the probe (equation (12)).

a) Amplifiers

The circuit diagram for the ampflier deck is shown in Figure 11. The amplifiers are DC-coupled, differential amplifiers, similar to the one described in Transistor Circuit Design, by the staff of Texas Instruments. This amplifier was chosen for its high input impedance (250 kΩ), along with reasonable gain (100 to 150). An input of 20 to 30 millivolts from sensing resistor provides full-scale modulation of the subcarrier. Tests on the amplifier indicate DC drift to be less than 200 microvolts (μv), equivalent input voltage, and temperature stability better than 75 $\mu v/^{o}$ C equivalent input voltage.

The first stage on each side of the balanced amplifier configuration is an emitter follower to give high input impedance. The second stages are common emitter amplifiers fed by a current source

in the emitter for stability. The 10Ω potentiometer connecting the emitters is used for balancing. The output is taken between the two collectors of the second stages. Silicon transistors, 2N338, are used throughout. It was noticed that General Electric 2N338 consistently had higher gain and lower leakage, resulting in more amplifier gain and a higher input impedance. For stability in this amplifier, it is necessary to keep both sides of the amplifier as nearly as possible in balance. The transistors and resistors should be in matched pairs. The one-kilohm (kΩ) resistors on the side of the amplifier tied to the ground must be adjusted to match the sensing resistor used for the input to the other side. Since the two amplifiers are tied together in parallel, the collector resistors in the second stages are twice the optimum value for the circuit.

b) Switching

Switching between the amplifiers is accomplished by using the multivibrator to switch on and off the bias to the current generators in the amplifiers. The multivibrator is a standard astable circuit similar to that used in the programmer of the magnetometer. Each side of the multivibrator drives an emitter follower, used as a current switch to apply the bias to the amplifiers. This type of switching results in no DC level change, since the amplifier is completely off when not in use.

c) Ramp Generation

Figure 14 shows Deck 2 of the Langmuir probe electronics containing the circuitry for generation of the ramp and the sensing resistors. The output from the multivibrator is channeled

into the scalers where it is scaled by a factor of eight. The scalers are bistable multivibrators in which diode steering insures that the incoming pulse will go to the proper transistor for switching to occur. The scaled output triggers a one-shot multivibrator. The signal is then fed through an emitter follower into the ramp generator. This circuit depends on the slope of an exponential charging characteristic being nearly linear over a short range. The resulting ramp is inverted in the last stage and applied to the probe. The 5-kΩ potentiometer serves to adjust the amplitude of the ramp.

d) Sensor

The expected probe current and the voltage desired at the input of the amplifiers determine the sensing resistors. The maximum probe current during the flight in the E region is about 30 microamperes (μa). The two ranges were set for 0 to 5 μa and for 0 to 50 μa. The maximum voltage drop across the sensing resistor in each case must be enough to cause the amplifier to modulate the subcarrier fully. A 10-kΩ resistor with 5-μa current will establish a 50-mv signal for the amplifier. Note that this is well below the 250-kΩ input impedance of the amplifier, so no appreciable loading will occur. The sensing resistors are Corning type C, 2% glass resistors.

e) Probe

A detailed view of the Langmuir probe at the top of the payload is shown in Figure 15. The nose cone for the payload was necessarily made of fiberglass. To obtain a well-defined geometry

and a large electric area ratio, it was decided to place (adjacent to the nose tip electrode) a stainless steel ring, electrically connected with the payload base and rocket motor. The steel ring was separated by one inch of Teflon from the tip probe. A coaxial cable was used to bring the electrodes to the electronics package in the payload.

f) In-Flight Calibration

Since the DC amplifier is inherently subject to drift, it was desired to provide a means of in-flight calibration. It was also useful as a check of the densitometer altimeter to provide a determination of the time the rocket passed a given altitude on the upward and downward legs of the flights. Both objectives were accomplished with the use of a barometric pressure switch set at 70,000 feet. The baroswitch used was a College Hill Industries Model 6617A, modified by the factory to make it magnetically clean. A 499-kΩ, 1% Corning type N resistor was placed between the probe and the rocket ground, and it was removed from the circuit at 70,000 feet by the baroswitch operation. This allowed a check of the preflight calibration on both the upward and downward legs.

D. Associated Experiments

An ionization chamber densitometer was employed to provide an alternate means of trajectory determination through pressure altitude measurement. NRC type 8717 Alphatron digital transducer was modified to obtain higher pulse rate and therefore, better accuracy when the pressure is changing rapidly (Figure 5). The instrument consists of an ionization chamber, containing a

radioactive source and an electrometer, in a blocking oscillator circuit. At low pressures the number of molecules ionized in the chamber is small, resulting in a small electrometer current and a small pulse rate. At higher pressures the pulse rate increases as more current is detected by the electrometer tube.

Figure 16 shows the modified circuit. L_1 and R_1 were inserted to change the pulse frequency. The voltage on the chamber was also lowered to 30 volts. Other modifications were found to have a greater effect on the frequency; however, they resulted in circuit instabilities. The values used for L_1 and R_1 varied with each unit, as the circuit was very sensitive to the gain of the electrometer and the β of the transistor. R_4, $C_1$and C_2 were used to shape the output pulses for the subcarrier oscillator. Wave traps (described in the magnetometer section) were used to reduce RF interference.

The baroswitch, discussed in C, (f), also provided pressure altitude at two points of the trajectory. Also included in the payload was a magnetic aspect sensor (Heliflux magnetic aspect sensor type RAM-5C, made by the Schonstedt Instrument Company). The unit is designed to monitor one component of the field - along the axis of the sensor. The sensor was mounted with its axis perpendicular to the spin axis of the rocket, hence also perpendicular to the axis of the polarizing field. Thus, the axial magnetic field generated in the magnetometer coil would not affect the transverse component measurement of the aspect sensor. Figure 17 shows the aspect deck with the sensor on the right, the aspect sensor electronics on the left, and the baroswitch at the bottom. The output

of the sensor is a sine wave at the spin frequency of the rocket. Precession of the rocket is measured by noting the changes in amplitude of the sine wave as the spin axis changes its angle with the earth's field.

E. Telemetry

An FM-FM telemetry system was employed to send the information back to the ground. Information from the Langmuir probe, aspect sensor, and densitometer modulated three voltage-controlled oscillators (Dorsett Model 018D-3). These were equipped with non-magnetic aluminum cases.

The output of the subcarriers and the magnetometer signal are combined in the mixer (Figure 18). As the Langmuir probe reference potential is not at the rocket common ground potential, the 70-kc SCO circuit is floating and operates from a separate battery. Transformer coupling is necessary at the mixer. The 70-kc signal is then fed through a common base amplifier before mixing with the other signals. The 50-K Ω potentiometer provides additional adjustment of the magnetometer signal. The 47-K Ω resistors in the input of the SCO's are necessary to provide the proper loading impedance for the oscillators. The resulting composite signal is amplified in a common emitter circuit and passed through an emitter follower stage to lower the output impedance. Composite signal level is adjusted by the 10-K Ω potentiometer.

The transmitter used was a Bendix TXV 13. The composite signal was introduced into a compensated phase modulation input. This provided a reasonably flat modulation vs. frequency

characteristic. Lower frequencies required slightly more input level than did higher frequencies for the same output level. Plate voltage for the transmitter tubes was supplied by a Sun-Air power supply. A Zener diode was placed across the output of the supply to regulate the voltage and prevent transient voltages from damaging the transmitter. The transmitter and power converter were mounted in the base antenna section, while the SCO's and the mixer were above on a separate deck. (Figure 2).

F. Power

Since not all payload circuits were at a common ground potential, it was desirable to use separate sources of power. Silver cells (Yardney HR-3NM) supplied the power for polarizing the magnetometer coil and for the power converter supplying the transmitter. Mercury cells mounted in a separate pack on the SCO deck supplied power to the Langmuir electronics. One battery deck consisted of mercury cells for the magnetometer electronics supply, an alkaline 28-volt pack for the SCO supply, mixer and aspect sensor, and a separate 30-volt battery for the 70-kc (Langmuir) SCO. Densitometer batteries were in a separate pack in the densitometer enclosure.

For safety reasons it was required that no payload power be on while the assembled rocket was being mounted on the launcher. It was necessary, therefore, to have a means of holding power off until flight. Magnetic latching relays were not desirable, due to large stray magnetic field. However, it was possible to effect an electrical latch by using one of the set of contacts on the power control relay. Figure 19 shows a schematic of the main battery deck.

The hold current was supplied by Yardney, HR-1NM, silver cells on the silver cell deck. A turn-on pulse to the T-relays causes the hold current to be applied to all the relays except the X-relays which turn on payload power. A turn-off pulse to the X-relays causes the hold current to be broken, and the power to the payload to be turned off. All the relays are GE 3S2791G200A5 "postage-stamp" relays. They have a very low external field in the "on" state and were placed back-to-back for cancellation of any magnetic dipole moment. Throughout the power control circuits two relays were used in parallel to prevent accidental dropout during flight.

G. Testing

Testing the payload was divided into three main phases:

1. Magnetic field tests.
2. Shock and vibration tests.
3. Individual unit and complete payload tests.

Although operation under extreme temperature conditions was not a prime design consideration in the instruments, due to the short time of flight (about six and a half minutes), thermal tests were made on all the units, and temperature effects were minimized where possible.

1. Magnetic Field Tests

In order that fields from the vehicle would not distort the ambient field to be measured, magnetic fields due to the payload were kept small. Tests of each payload deck were made in the University of New Hampshire magnetic test facility. Zero field was first established (to within 1 γ). The instrument was then passed under a

three-axis flux gate magnetometer sensor. The outputs of the magnetometer were recorded (Figure 20) on an oscillograph. At the distance of closest approach of the instrument to the magnetometer, the vector field of the tested instrument can be determined. For example, the record in Figure 20 is interpreted as an indication of a five-gamma field due to a permanent dipole moment oriented along the X-axis of the instrument. It was found that even the Subminax coaxial cable supplied as antenna harness produced a stray field (due to its steel center conductor) and it was replaced with a copper-conductor coaxial cable. A final check of the completed payload was made after "degaussing." Payload fields were kept to less than 2 gammas.

2. Shock and Vibration Tests

The instruments must withstand 15 to 20 G vibration, and over 50 G shocks. Initial tests were made by dropping the payload onto a pad; the acceleration was measured by a miniature accelerometer mounted on the payload. This was not convenient for routine tests of subassemblies. An effective rough check is to slam the deck down on a lab bench several times; if it does not function after this test, then a more sturdy mounting is needed. Vibration tests of a complete payload were accomplished on a shake table.

3. Individual Unit and Complete Payload Performance Checks

Each unit was individually tested and calibrated for performance of its proper function. It was also necessary to test each unit assembled in the payload with the other instruments running. Interference problems, especially RF interference in the magnetometer and the densitometer, were effectively reduced by the copper boxes

and the wave traps.

A complete check of all instrumentation through telemetry was done before each payload was packed for shipment to the launch area. At the launch area further tests through the telemetry were made before final assembly. At the time of final assembly screws and nuts were cemented in place, and "RTV" compound was applied to all wiring harnesses for strain distribution. One short final check of payload operation was made while the rocket was horizontal on the launcher. From the time of final assembly to launch, the battery voltages were monitored through the umbilical cord at the test box. This box was also used to turn power off and on in the rocket.

CHAPTER IV

EXPERIMENTAL PROCEDURE

A. Flight Locations

1. India

Four rockets were launched from the Thumba Equatorial Rocket Launching Site near Trivandrum, Kerala State, India (8.52° N lat.; 76.87° E long.). Measurements by Pisharoty and Srinivasan (1962), indicate that the center of the electrojet passes through the point, 8.70° N lat. and 77° E long., about 0.2° north of the launch site. The magnetic dip equator crosses southern India from the southwest to the northeast (Figure 21). All four rockets were fired at a corrected elevation (for wind) of 80° and a corrected azimuth of 270°. The approximate range of these flights was 75 nautical miles. Thus, the downward leg of each flight was closer than the upward leg to the center of the electrojet.

Two flights were launched close to the peak intensity of the electrojet: UNH 64-1 (NASA 14.79 UE, INCOSPAR 20.01) on 25 January, 1964, at 1100 hours Indian Standard Time; and UNH 64-2 (NASA 14.80 UE, INCOSPAR 20.02) on 27 January, 1964, at 1000 hours. UNH 64-3 (NASA 14.81 UE, INCOSPAR 20.03) was launched in the afternoon at 1530 hours on 29 January, 1964, into slightly disturbed magnetic conditions (second 28-day recurrence of the December 2, 1963, storm). UNH 64-4 (NASA 14.82 UE, INCOSPAR 20.04) was launched in the evening, at 1900 hours on 31 January, 1964, to investigate the existence of nighttime currents.

Figures 22 through 25 are copies of preliminary magnetograms from the Trivandrum, India, Magnetic Observatory for the four launch dates (Subramanian, 1964). The launch times are noted on the magnetograms.

January 27 was one of five selected quiet days for the month. January 29 was active from the recurrence of the storm; January 31 was also active during the day, but it quieted down at the time of flight. A_p indices for the flight days were: 16 on the 25th; 4 on the 27th; 21 on the 29th; and 26 on the 31st.

2. Peru

Two of the Peru flights were launched from north of the geomagnetic equator. Flight UNH 65-2 (NASA 14.85 UE) was launched due west at 1136 hours local time on March 9, 1965, from 3^{o} 07' S latitude and 84^{o} 22' W longitude. This was more than 8^{o} north of the magnetic dip equator, hence well to the north of the equatorial electrojet (extending 3^{o} north and south of the dip equator (Forbush and Casaverde, 1961). Flight UNH 65-3 (NASA 14.83 UE) was launched due west at 1100 hours on MArch 10, 1965, from 6^{o} 30' S latitude and 84^{o} 32' W longitude. This still was more than four and one-half degrees north of the dip equator.

Two more flights were launched on March 12, 1965, from nearly the same point, close to the magnetic dip equator. UNH 65-4 (NASA 14.07 UE) left the ship at 0830 hours, from a position 11^{o} 23' S latitude and 81^{o} 25' W longitude. This was at a time of maximum negative effect of the lunar current system for that day. UNH 65-5 (NASA 14.84 UE) was launched at 1100 hours from 11^{o} 25' S latitude

and 81° 20' W longitude. The locations of the four Peru flights are shown in Figure 26.

The period from March 9, through March 12, was magnetically very quiet; magnetograms from the Peruvian stations of Huanuco (9.9° S; 76.3° W), Casma (9.5° S; 78.3° W), and Canete (13.1° S; 76.4° W) for this period are shown in Figures 27 through 30 (courtesy of S. E. Forbush, Dept. of Terr. Mag., Carnegie Inst.). Some disturbance is noted between 0730 and 0900 on March 12. Launch times are noted on the respective magnetograms. Canete is located closest to the magnetic dip equator. March 10 and 11 were two of the five quiet days for March, and March 9 was included in the ten quiet days for the month. A_p indices for the period are: March 9 - 4; March 10 - 2; March 11 - 4; and March 12 - 4.

B. Data Handling

1. Trajectory

Since radar was not available for some of the flight, a barometric pressure switch and a densitometer were included to determine the trajectory. The baroswitch gives the two times when the vehicle crosses 70,000 feet. The densitometer output is a series of pulses, the frequency of which is proportional to the barometric pressure; hence, the portion of the trajectory in the atmosphere is obtainable, assuming a standard atmosphere (U. S. Standard Atmosphere, 1962).

A computer program was developed to calculate a variable g (g = acceleration due to gravity) free fall trajectory, given the time of apogee and a particular time and altitude (see Appendix A). To correct for drag from the atmosphere, 0.5 second was subtracted

from the baroswitch times (Smith, 1963b). The program computes the time for a given altitude. To obtain altitudes corresponding to the times of the various measurements, a straight time interpolation was done on the computer (the program is given in Appendix C). A comparison of radar data, baroswitch times, densitometer data, and the trajectory calculated from the baroswitch times is given for two of the Peru flights in Appendix B.

2. Magnetometer

Recorded along with the video output of the tracking receivers was a 100-kc standard signal. This was necessary for use with the magnetometer data as a reference standard for the frequency counter in the data reduction equipment (Figure 31). Since switching transients occur at the beginning of each magnetometer signal, the first few cycles of the signal were discarded. This was done with the aid of the "dual Preset" counter. The Muirhead frequency analyzer served as a very narrow band filter to select the precession signal from the complex video output and to reduce noise. A pass-band Q value of 150 is obtainable.

The frequency of each magnetometer signal was measured ten times, and the average of these was taken to obtain the measured magnetic field. A theoretical field was then subtracted from the measured field to separate effects from the currents from the normal variation of the magnetic field with altitude. Error bars were set by adding $\pm 1\ \gamma$ to the average deviation of the ten measurements of each signal. The current density was found by taking the slope of the graph of the difference field (the field resulting from the

currents) versus altitude. On the Peru flights, where the field was not well enough known to remove all of the normal altitude variations, the remaining slope was subtracted to get the actual current density.

For the Peru flights the theoretical field was calculated every five kilometers over the trajectory (private communication from Dr. Gilbert Mead, GSFC), and a computer was used to interpolate for the value corresponding to each magnetometer measurement. (The program given in Appendix C.)

3. Langmuir Probe

Data from the subcarriers were removed from the complex video output, using subcarrier discriminators, the output of which, along with the time code from the flight tape, was recorded on a high-speed oscillograph. The data from the Langmuir probe were recorded separately along with the time code. The amplitude of the signal was found and converted to probe current, using a preflight calibration. On the Peru flights the baroswitch was used for an in-flight calibration. The preflight calibration was linearly adjusted where necessary to fit the in-flight calibration check.

CHAPTER V

EXPERIMENTAL RESULTS

A. Description of India Flight Records

1. UNH 64-4

UNH 64-4 reached a peak altitude of 174 km. A reference magnetic field, calculated from the spherical harmonic analysis of Finch and Leaton (1957) was subtracted from the measured values of the field. The resulting difference field (Figure 32) showed no indication of distinct current on either the upward or the downward leg. If a diffuse layer of current existed between 100 and 170 km, it was too weak to produce a displacement of the magnetic field by as much as ten gammas.

The several fluctuations that appear on the flight record are approximately periodic in time. Their period is nearly the same as the rocket precession period for this flight - 39 seconds. These fluctuations may be due to rotation of the residual rocket and payload magnetic field, with respect to the geomagnetic field vector. The overall non-zero slope of the difference field is interpreted as an indication that the Finch and Leaton reference field does not adequately describe the geomagnetic field in this region. On the assumption that ionospheric currents were negligible, the data from this flight were smoothed for use as a corrected reference field for the other three flights.

The Langmuir probe current between 95 and 150 km, proportional to the electron density, was less than that observed on the morning

flights, by a factor of 20 or greater, except for the local maximums at 115 and 122 km on the upward leg (Figure 33) and at 122 km on the downward leg (Figure 34), which were less by a factor of 15. The upward leg also had a local maximum between 90 and 100 km. On the downward leg the lower maximum had moved up to between 99 and 108 km. An inflection point, corresponding to the upward maximum at 115 km, was observed. The electron density above 125 km was less on the downward leg, and a small maximum appeared at 135 km on this leg.

2. UNH 64-2

Preliminary results from UNH 64-2 indicated a strong west-to-east current, 55 to 60 km down from apogee (Maynard, Cahill, and Sastry, 1965). Using UNH 64-4 as the reference, a difference field was produced for detailed analysis of electric current evidence (Figure 35). The total field shift between 95 and 140 km was 68 ±4 γ. This would produce a 34 γ horizontal field contribution on the ground, on the assumption of a current layer of infinite extent. The actual departure of the horizontal component of the field from the nighttime value is (from Figure 23) 30 γ . Only two-thirds of this, 20 γ, is usually attributed to overhead currents, and the remainder to induced currents below the surface of the earth. The difference between ground-level contribution as determined by rocket measurements, 34 γ, and that determined from surface measurements, 20 γ, should be explained. The overhead current, at least the electrojet ribbon, is not infinite in extent. The electrojet width has been estimated as being greater than 300 km by Cahill (1959), and as 314 km by Ogbuehi and Onwumechilli (1964) from 1963 data over Africa. We

estimate, for a ribbon 300 km wide, a reduction of magnetic field from 34 γ to 20 γ at the earth's surface. The reduced electrojet field, 20 γ, fits the surface H observation. It also may be possible that induced subsurface currents may be less intense than elsewhere at this location, a boundary between land and sea, so that more than two-thirds of the 30 γ is due to overhead currents.

The slope of the difference curve is proportional to the current density (Figure 36). The current density plots are subject to the errors of the difference plots and errors in drawing an average curve through the data points. These current densities should be taken as approximations to the actual currents. The main current layer was found to be centered at 105 km on the upward leg and 109 km on the downward leg. This discrepancy in altitude may be due to systematic errors in trajectory determinations. At 105 km the estimated absolute error in trajectory is ± 3 km, while relative point-to-point errors are ± 0.1 km. The current decreases gradually with increasing altitude to reach zero between 130 and 140 km. Indications of a second layer are present, centered about 152 km on the upward leg and 145 km on the downward leg. The smaller changes which suggest the second layer may well be due to time variation in the main layer. However, the presence of a field change at similar altitudes on both the up and down legs of the flight lends support to interpretation of the field changes as due to spatial structure.

Langmuir probe current indicated the normal E region increase in electron density between 90 and 100 km (Figure 37). On the downward leg a local increase about 110 km was observed at the same altitude as the main body of the current on that leg. The peak

magnitude of the current (Figure 36) was correspondingly higher than on the upward leg. Measurements on the downward leg above 120 km showed a scatter greater than the expected error and not obviously correlated with flight effects or the magnetometer, indicating a possible fine structure in the electron density of the equatorial E layer.

3. UNH 64-1

Reaching an apogee of 163 km, UNH 64-1 showed the peak in current at 106 km on the upward leg and 109 km on the downward leg (Figures 38 and 39). The current layer on the downward leg was again more intense and thinner in altitude. Both portions of the flight record exhibited diffuse current up to about 130 km, while the bottom of the current layer decreased more abruptly. No attempt was made to estimate the current above 130 km due to scatter of the data. The total change in field on the upward leg was 70 ±4 γ, accounting for a 35 γ ground-level field contribution, and a 64 ±4 γ contribution, accounting for 32 γ on the ground, was seen on the downward leg. This is to be compared with the Trivandrum magnetogram departure from the night level of 33 γ at the time of flight. Correction for the finite width of the current layer gives reasonable agreement with ground measurements. The electron density profile (Figure 40) exhibited the same scatter above 120 km on the downward leg that was observed on UNH 64-2. It was also present above 140 km on the upward leg. The period of rocket spin was about 0.2 seconds, and the precession period about 50 seconds for UNH 64-1.

4. UNH 64-3

The record from UNH 64-3, flown in the afternoon, indicated two current layers on each leg (Figures 41 and 42). On the downward leg the lower current was centered at 107 km, and an upper layer was apparent at 140 km (corresponding to that of the downward leg on UNH 64-2). On the upward leg the center of the main current was at 103 km. A broad, diffuse layer appeared to be centered about 130 km. The lower current layers were reduced in magnitude by a factor of about four, from the morning flights, as was the electron density. The magnitude of the upper layers for Flight UNH 64-3 appears greater than that of Flight UNH 64-2, although the electron density is lower by a factor of four.

The upward leg electron density profile (Figure 43) has a maximum near 105 km and a gradual increase near 130 km, close to the peaks in current density. The downward leg profile has a maximum centered about 103 km and a distinct oscillatory variation superimposed on a gradual increase between 120 and 140 km. The fluctuations suggest changes of the order of 8 to 10% of the total electron density and have approximately a constant period of 1.55 seconds. The spin period for this flight was approximately .3 seconds and the precession period approximately 67 seconds. These fluctuations are directly correlated with the magnetometer period. The decrease in current coincides with the polarize part of the magnetometer period.

Full moon was on January 27, 1964; thus, UNH 64-3 was fired into the time of maximum negative effect (L current opposed to S_q current) of the lunar current system (L), (Chapman and Bartels, 1940).

No negative departure was evident on the ground magnetogram, probably due somewhat to disturbed magnetic conditions. The currents that were deduced from rocket observations were all flowing west to east.

B. Description of Peru Flight Records

1. Equatorial Flights

UNH 65-5, flown near the geomagnetic dip equator at 1100 hours, reached a peak altitude of 173 km. Radar data for the first two minutes of flight were extrapolated to find the range and the theoretical field was calculated over the resulting trajectory, using the coefficients of Leaton and Evans. The difference field (Figure 44) starts to change slope about 93 km, with the steepest slope at 108 km on the upward leg and 110 km on the downward leg. The discrepancy is believed to be due to errors in determining the trajectory. The total change in the field is about 120 γ, in comparison with the 60 to 70 γ for the mid-day India flights. At launch time a 102 γ departure of the field in Cañete, Peru, from the nighttime value was noted as a qualitative comparison. Twenty minutes earlier, the departure was 91 γ (allowing for the time difference between the launch site and Canete). The gently sloping tail above 130 km on the downward leg is the result of inaccuracies in the calculation of the theoretical field, presumably. The wide fluctuations below 85 km on the downward leg were apparently caused by rotation of the magnetometer sensor axis as the rocket spin axis overturned, since they are correlated with similar fluctuations in the magnetic aspect record.

Figure 45 depicts the current density derived from the slope of the difference field. A field of constant slope, 0.35 γ/km was

subtracted from the downward-leg data to remove the normal field which remained after the calculated theoretical field had been subtracted. The peak current density is twice that observed in India. The diffuse tail, observed in India, here extends to 135 km. No evidence of a second layer was observed.

UNH 65-4, launched at 0830 hours from nearly the same position as UNH 65-5, reached a peak altitude of 178 km. Radar data again was extrapolated for finding the trajectory for the calculation of the theoretical field. The resulting difference field is shown in Figure 46. The shape is nearly identical to that of UNH 65-5 with reduced magnitude, the maximum occurring at 108 km on the upward leg and 110 km on the downward leg. Total change in the field was 27 γ. Departure of the field from the nighttime values on the magnetogram records at Canete was 36 γ at the time of launch and 29 γ twenty minutes earlier. The greater scatter of the data points on this flight was due to noise on the signal.

A constant slope of 0.4 γ/km was subtracted from the downward-leg curve in obtaining the current density plot (Figure 47). The peak current was reduced by a factor of five from that observed by UNH 65-5. On this flight the diffuse tail was visible only out to 125 km, due to the reduced magnitude of the layer. No evidence of a second layer or of any reverse currents was observed. The flight was at the time of maximum negative effect of the lunar current system (Chapman and Bartels, 1940).

Figures 48-51 show the Langmuir probe current as a function of altitude for the two flights. On none of the graphs is there any significant peak in the electron density correlated with the observed

current. It is noted that, while the current density measured by UNH 65-4 was down by a factor of five from that of UNH 65-5, the probe current was reduced by less than a factor of two. Small fluctuations are observed on both the upward and the downward legs of UNH 65-5. Some modulation of the probe current at the spin rate (6.25 cps) of the rocket was observed. The sampling rate of the Langmuir electronics was 5.5 per second, leading to a beat frequency of approximately the period of one magnetometer signal. The fluctuations, however, have a period equivalent to two magnetometer periods. These fluctuations are stronger on the downward leg.

Ionogram profiles of electron density are included on the graphs of probe current for the Peru flights. These profiles were calculated from the records of the ionosonde aboard the USNS Croatan by J. W. Wright of the Aeronomy Laboratory of ESSA. Comments in regard to the profiles themselves are his. The proportionality constant between the probe current and electron density was determined by a visual best fit of the two types of curves. A slightly different scale factor was used to fit the data for UNH 65-3. There was no obvious justification for this; however, it was desirable for the purposes of comparison.

Two ionogram profiles are shown for UNH 65-5, those of 1050 hours (prior to launch) and of 1109 hours local time (after launch). The valley restart (method of obtaining profile when the echoes of a region are blanketed by a lower region) on the 1109 profile indicated a valley 11.5 km wide, but it does not define the depth of the valley. No indications of a valley were seen in the probe data. The general agreement between the curves is good.

The overall features of the curves of both methods were similar for UNH 65-4. The profiles for 0822 hours and 0838 hours local time are shown. The differences between the upleg and downleg probe data is partially due to trajectory error. A valley restart on the ionograms above the E peak at 115 to 119 km would have been preferable, but it was not possible due to complicated F region echoes. A slight valley is seen in the downward leg of the probe data just above this region.

On the downward leg of UNH 65-4, fluctuations in probe current of about 15% were observed between 125 and 145 km, similar to those of UNH 64-3. The period of these fluctuations coincided with that of the magnetometer signal. The probe current decreased during the polarizing period, when an axial field of about 0.7 gauss was created at the probe by the magnetometer coil. Similar but smaller fluctuations were seen between 98 and 103 km and above 155 km on the downward leg and between 140 and 150 km on the upward leg. The spin frequency was 6.9 cps, while the probe sampling rate was about 4.9 per second, eliminating the possibility of a beat frequency between the two. The fluctuations observed on UNH 65-5 were smooth and somewhat sinusoidal, while those on UNH 65-4 (and those on UNH 64-3) more nearly resembled a square wave.

2. Flights North of the Dip Equator

Launched more than 8^{o} to the north of the electrojet, UNH 65-2 reached an apogee of 163 km. Radar tracking data in the early portion of the flight, along with the apogee time taken as the time of minimum magnetic field (corrected for changes in the field over the range of

the vehicle) were used in computing the trajectory. The Leaton and Evans theoretical field was computed over the calculated trajectory.

The difference field is shown in Figure 52. Many of the small variations apparently are due to the precession of the rocket with a field of about 3 γ. The arrows over the curves denote the time of maximum positive effect of the precession, while the arrows under the curves denote the maximum negative effect. These times were taken from the precession record obtained from the magnetic aspect data. The total shift in field from passing through the current system was 45 γ on the upward leg and 38 γ on the downward leg. The difference is thought to arise from inaccuracies in the trajectory and hence in the calculated theoretical field. Also a result of this is the slight constant general slope of .15 γ/km, which was removed before computing the current density. Precession effects do not account for the change in slope around 110 km. This is interpreted as evidence of a double-layered current structure with the lower layer being centered at 100 km and the upper at 120 km. The current density - versus altitude graph (Figure 53) shows that the two layers are nearly equal in magnitude. The repetition of the pattern on the downward leg indicates that is is not the result of a time fluctuation in the magnetic field. The two points that widely deviate from the curve on the upward leg of the difference curve are believed to be the result of noisy magnetometer signals. The fluctuations below 65 km on the downward leg again are due to the overturning of the rocket spin axis.

UNH 65-3 was launched closer to the electrojet (about 4.5^{o} north of the dip equator), reaching an apogee of 172 km. The radar range was extrapolated and combined with the trajectory calculated

from the baroswitch data to use in computing the Leaton and Evans theoretical field. The plot of the difference field (FIgure 54) shows no changes until 105 km. The total shift in field from the current was 27 γ, with the maximum current at 114 km. The shift on the ground observed at Casma (the closest station) was 63 γ from the nighttime values at flight time; however, this station is significantly closer to the electrojet. Between 105 km and 108 km indications of a small reverse current appear on both legs of the flight. This is partially obscured on the downward leg by the constant slope of .67 γ/km which remains after subtraction of the theoretical field. The total change in field from the current system is 35 γ. Overturning of the rocket spin axis occurs below 70 km on the downward leg, causing the data to be scattered.

The current density derived from the difference field indicates the maximum current density of the reverse current to be between one-fourth and one-third that of the maximum normal current, although the total reverse current is much less than the normal current (Figure 55). The normal current is slightly lower in altitude and approximately the same in magnitude as that of the upper layer observed on UNH 65-2.

The electron density profiles for UNH 65-2 (Figures 56 and 57) showed a weak, sporadic E formation at 106 km on the downward leg but not on the upward leg. A local maximum was observed on both legs at 106 to 107 km. This correlates with the trough between the two current layers. Some small fluctuations with a period equal to the magnetometer period occurred between 140 and 150 km on the upward leg and between 125 and 135 and above 150 km on the downward leg.

These had the opposite correlation from those observed on the dip equator flights. Here, the probe current increased during the polarizing part of the magnetometer cycle.

Information from the ionograms of 1132 hours and 1145 hours local time was used to compute the plotted ionogram profile for UNH 65-2. Not included in the calculations because of the weak scattered nature of the echoes is the sporadic E layer observed. The scattered nature of the echoes suggests that it was not present everywhere, a fact confirmed by the observance of a weak sporadic E layer on the downward leg of the current profile but not on the upward leg. The height is slightly above 101 km, from ionogram data, while the probe data indicate it at 105 km. Evidence of sporadic E was present on both ionograms.

Probe results from UNH 65-3 (Figures 58 and 59) showed a region of electron concentration between 126 and 130 km on the upward leg and between 130 and 134 km on the downward leg, with the electron density increasing by 20%. The measured probe current was approximately two-thirds that of UNH 65-2 in the region between 95 and 105 km, where the lower layer was observed on UNH 65-2.

Ionograms for 1049 and 1107 hours local time are shown for UNH 65-3. As previously noted, a different proportionality constant was used in the comparison with the probe current. The 1049 calculation is taken up to the sporadic E layer above 120 km (seen in the probe current at a slightly higher altitude). This blankets the regions above, preventing further calculations. At 1107, however, three portions of the profile were computable in additions to the "monotonic" approximations. The lower segment is identical

with the monotonic calculations up to the lower E region maximum. The second segment is between 121 and 124.5 km, and the third segment begins at 129 km. The maximum was also much less pronounced on the downward leg probe current profile and was also shifted up in altitude.

CHAPTER VI

DISCUSSION

A. The Equatorial Electrojet

The results from the India flights indicate that the equatorial electrojet over India is an intense layer of current centered about 109 km, with a more diffuse tail extending up to about 130 km. A short distance away from the dip equator, as evidenced by the upward leg of these flights, the current appears thicker in vertical extent and lower in peak current density. The same vertical structure was observed in the two equatorial flights over Peru, the main difference being that the magnitude in Peru is about twice that observed in India. The change in conductivity with longitude due to the longitudinal variation of the earth's magnetic field has been shown by Sugiura and Cain (1965) to account for the change in magnitude. In Peru one could observe evidence of current up to 135 km because of the greater intensity. The vertical profile of the current from these measurements indicates an electrojet that is thicker and centered slightly higher than shown by previous results in the Pacific (80^{o} west in longitude from Peru), (Cahill, 1959). It was found from the India flights that the maximums in the altitude profiles of electron density were correlated with peaks in the current density, although the reverse was not always evident. This correlation was not observed in Peru, as the electron density profiles of the equatorial flights did not exhibit distinct maximums.

Near the center of the electrojet over India there may exist a second peak in current density about 10 km in vertical thickness

and centered at 140 to 145 km. Careful examination of the flight records of UNH 64-2 and UNH 64-3 leads one to believe that there are weak currents at these altitudes. The possibility of a second layer was first suggested by Cahill (1959), but his measurements indicated that the center was at a lower altitude. It is possible that time variations in the magnetic field (more apparent near apogee in flight records, where the rocket is moving relatively slowly) have caused the magnetic changes that appear to be currents. Relative maximums of electron density were observed at the altitude of the second current layer in each case, supporting the existence of the second layer. The height fluctuation of the second layer, observed on the upward legs, may have been caused by the change in the magnetic activity. Balsley (1964; 1965) has recently seen weak radar scattering centers over Peru at about 150 km in altitude, similar to those observed between 95 and 110 km and associated with the electrojet (Cohen and Bowles, 1963). However, no indications of a second layer were seen on the Peru equatorial flights.

A nighttime flight was included in the launchings over India, and there were no obvious currents observed. The maximum magnetic effect of nighttime current between 90 and 150 km was less than 10 γ.

The discrepancy between rocket and ground determination of the contribution by the electrojet to the horizontal magnetic field in India is probably due to the finite width of the electrojet. The width has been shown to decrease during periods of low solar activity (Ogbuehi and Onwumechilli, 1964). It has been estimated to be about 440 km over Nigeria in 1956 by Ogbuehi and Onwumechilli (1963), about 330 km over Nigeria in 1962 by Ogbuehi and Onwumechilli (1964),

and 600 km over Peru in 1958 by Forbush and Casaverde (1961). Another cause could be an anomalously low induced subsurface current contribution. In Peru comparison with the magnetogram values was difficult due to the separation of ship and ground stations. Since the earth rotates under ionospheric currents (see Introduction), the current effect that was seen over the ship would have been seen at ground stations in Peru at an earlier time. An attempt was made to allow for this delay by comparing the rocket results with magnetogram values 20 minutes prior to launch. The contributions from UNH 65-5 were two-thirds of the total ground departure. However, this does not allow for any reduction in magnitude due to the finite width of the electrojet. For UNH 65-4 the contribution was less than one-half of the ground value (observed 20 minutes prior to launch); however, percentage errors in measurements are magnified by the small size of the effect at this time of day.

Two flights, UNH 64-3 and UNH 65-4, were made near the time of maximum negative effect of the lunar current system (Chapman and Bartels, 1940). No reverse currents were observed on these flights. While this is not conclusive, it suggests that the lunar variations result from a modulation of the normal electrojet rather than from a separate current layer. One also notes that while the current observed by UNH 65-4 was less by a factor of five than that observed by UNH 65-5, the electron density in the range between 100 and 110 km was less by an average factor of about two. The electron density is directly related to conductivity; hence, the driving field must have been smaller, possibly from the negative lunar effect.

Values of σ_1 and σ_2, taken from the graphs of Maeda and

Matsumoto (1962) were used to calculate the Cowling conductivity σ_3 which is σ_{yy} on the dip equator (see Introduction). The resulting graph of σ_3 versus altitude is shown in Figure 60. The peak is slightly wider but the curve strongly resembles the current profiles of the equatorial flights of both India and Peru. The current profiles are also similar to the plot of $N\sigma_3$ (σ_3 in Figure 2 does not contain the electron density) given by Baker and Martyn (1953) and shown in Figure 2.

B. Langmuir Probe Results

Correlations between observed maximums in probe current and ionospheric current layers were found to exist; however, not all observed current layers had a definite corresponding maximum in probe current. In the India series, the afternoon flight showed a decrease in both the magnitude of the observed lower current layer and the Langmuir probe current (hence conductivity) of a factor of four from the corresponding values for the morning flight.

No sporadic E type increases in electron density were observed on the rocket records for the equatorial flights, confirming the supposition that equatorial sporadic E arises from echoes from small field-aligned irregularities throughout the current layer (see Chapter II). Small sporadic E increases were seen on both of the off-equator flights. In neither case was enhancement of the current layer observed.

Comparison of the Langmuir probe current profile of the Peru flights to shipboard ionogram profiles showed a general similarity in shape of the two types of profiles in each case. Using the same

proportionality constant of probe current to electron density resulted in close agreement in three cases and agreement within twenty percent in the fourth. Small differences in the altitude at which a feature of the profiles occurs can be accounted for by the errors in altitude determination in both methods. Equatorial sporadic E was seen on the surface ionograms for UNH 65-4 and UNH 65-5. Sporadic E was also observed on the ionograms for UNH 65-2; however, it was apparently patchy and could not be included in the profile (J. W. Wright, private communication).

The electron density observed on the night flight from India was less by a factor of twenty or more than that observed during the day over most of the profile. This supports the fact that no current layer was observed, since the conductivity would have been proportionately less. The structure of the nighttime profile showed large variations in the lower portion of the E region. The cause of these is not known at this time. Somewhat similar results were observed from the USNS Croatan off the coast of Peru by Blumle, Aikin and Jackson (1965).

Small fluctuations with a periodic structure were observed on several of the flights. On UNH 64-3 and on UNH 65-4 the fluctuation frequency coincided with the magnetometer sampling frequency. On UNH 65-5 the period of the fluctuations was twice that of the magnetometer period. On this flight fluctuations at the spin frequency of the vehicle were also found which, when combined with the sampling rate of the Langmuir electronics, could have produced fluctuations of a period equal to that of the magnetometer. The result was fluctuations that were not sharply defined as in the

other cases. It is noted in these examples that the probe current decreases during the polarizing portions of the magnetometer signal. On one flight, UNH 65-2, very small fluctuations of the opposite correlation were observed; however, these were on the order of the experimental error. At the time of polarization an axial field of .7 gauss is created at the probe in addition to the earth's field. The collision frequency between electrons and neutrals at 120 km is given by Belrose, et al. (1964) to be about 1×10^4 per second. This is significantly less than the cyclotron frequency for electrons (about 5 megacycles) in this region. The gyration diameter is about 6 cm, or approximately the dimension of the probe. Nobata (1963) states that, if the electron-cyclotron frequency exceeds the collision frequency of electrons with neutrals, then the probe current will be independent of the magnetic field when the probe length in the direction of the magnetic field is smaller that the average gyration diameter of the electrons, and the current will be determined by the gyration diameter when the probe length is greater than the gyration diameter. Hence, a slight precession (changing the length of the probe along the magnetic field) coupled with the slight increase in gyration diameter with height, could cause the magnetic effects to be present at some portions of the flight and absent at others, as observed. This is verified by the downward leg of UNH 65-4, where the fluctuation effect has maximums at about 160 km and 135 km which are 35 seconds or one precession period apart. The fact that these fluctuations occur most often on the downward leg may be the result of part of the probe being in vehicle wake.

C. S_q Currents

Two of the Peru series of flights (UNH 65-2 and UNH 65-3) were made north of the electrojet and provided experimental evidence of the S_q current systems at low latitudes. These flights were north of the lateral extent of the electrojet given by Forbush and Casaverde (1961), calculated from data at the time of solar maximum. The results from 65-2 show a two-layered structure with the upper layer centered about 120 km and the lower layer at about 100 km. The maximum current density in each layer is nearly the same. This two-layer structure is consistent with the recent calculations of conductivity of Sugiura and Cain (1965). Their results indicate that the conductivity at this latitude has a double maximum. Their graph of σ_{yy} as a function of altitude and latitude is shown in Figure 61. S_q currents observed at mid-latitude by Burrows and Hall (1965) and Davis et al. (1965) consisted of a single layer. It is also noted that the electron density measured during the UNH 65-2 flight has a maximum between the two layers, and that a weak sporadic E layer was seen at this position on the downward leg.

One day later and closer to the electrojet (UNH 65-3) the lower layer was not present and the upper layer was centered at 114 km. Also, there were indications of a reverse current centered about 108 km. Chapman (1951) has suggested that some of the return current from the electrojet could flow at nearly the same altitude as the maximum of the electrojet, but to the north and south of the electrojet, thus creating a reverse current.

The total change in the field passing through the current system was 27γ for UNH 65-3 compared with 45γ (upward leg) and 38γ

(downward leg) measured on UNH 65-2. The ground station magnetometer of Casma, Peru, recorded a much higher S_q variation in each case, but it is probably under the edge of the electrojet. The magnitude of the current in the upper layers in both flights was nearly the same.

Again, there was no correlation of the observed currents with the sporadic E conditions observed at approximately 130 km by both the Langmuir probe on UNH 65-3 and in the surface ionogram.

CHAPTER VII

MODELS

In order to see if the measurements made of the electrojet were consistent and in agreement with ground measurements, an attempt was made at formulating a simple model.

The first model of the electrojet by Chapman (1951) and later work by Onwumechilli (1963) assumed that the current exists in infinitesimally small wires of infinite length. If a current I flows through one of these wires, the field at a distance R from the wire is given by

$$|B| = \frac{2I}{R} \tag{15}$$

and is directed in the θ direction considering a cylindrical system with the current flowing along the Z axis. Using this relation, one can then sum up the contributions from all of the "wires" in the cross section of the electrojet. If we transpose into rectangular coordinates, the resulting integral from the summations defines the field at a point with coordinates (b, -a) as

$$\bar{B} = \int dx \int dy \; \frac{2J(x,y)}{R} \cos\theta \; \hat{i}_x + \int dx \int dy \; \frac{2J(x,y)}{R} \sin\theta \; \hat{i}_y \tag{16}$$

where

$$\frac{x-b}{y+a} = \tan\theta, \quad R = \sqrt{(x-b)^2 + (y+a)^2}$$

and J is the current density.

Since the rocket flights have not yet yielded detailed information about the horizontal distribution of current, it was decided to omit any x variation of the current density. This allowed immediate x integration, and the result for the x component of the field is expressed by

$$B_x = \int_0^{y_1} dy \quad 2\ J(y) \quad \left[\tan^{-1} \frac{x-b}{y+a} - \tan^{-1} \frac{x_1-b}{y+a} \right] \tag{17}$$

where x_1 and x_2 define the limits of the x integration and 0 and y_1 are the limits of the y integration. A similar expression may be obtained for the y component of the field.

A program was then developed (by Mrs Marilyn Wingersky, University of New Hampshire Physics Department) to compute the two integrals for an arbitrary J(y), using the method of Gaussian quadratures. This program is given in Appendix B.

The measured current densities resembled an over-damped sine wave in vertical distribution. After plotting many forms of damped sine waves, the best fit to the Peru experimental results was picked as

$$J(y) = 32.142e^{-(.064577y)} \quad \sin^4 \quad (.064577y) \tag{18}$$

These constants are the result of fitting the curve to the data. Calculations made assuming various widths of the electrojet are shown in Figure 62. The greater magnitude of the change in the field from the current in the model calculation (compared with the measured values) results from the actual current being narrower

about the maximum than the model current, and from the neglecting of the x variation in the model current density. It is noted that the regions above 140 km and below 80 km have a greater slope than that observed. The near zero slope of the observed values is most likely the result of inaccuracies in the trajectory (and therefore in the theoretical field also) rather than an abnormally wide electrojet.

Figure 63 shows the change in the north-south component of the field as one moves away from the center of the electrojet (the width being assumed as 500 km). At 50 km distance from the center there is almost no difference. At 450 km from the center (the approximate distance of UNH 65-3 from the dip equator was 500 km) there is little effect from the electrojet. From this it is seen that the magnetic effect interpreted as a reverse current (UNH 65-3) can not have been caused by the electrojet itself.

In comparison with ground data, Figure 62 indicates that there is a reduction of 25% or greater in the field at the ground, in relation to that at the altitude of the electrojet, due to the effect of the finite width of the electrojet. Such a reduction was observed in comparing the India flight records with the corresponding ground data.

CHAPTER VIII

CONCLUSIONS

From these measurements we may conclude about the equatorial electrojet that:

1. The electrojet is an intense layer of current centered about 109 km with a more diffuse tail extending up to 130 to 135 km. The maximum altitude at which currents are observed is dependent upon the intensity, since a low intensity results in changes in magnetic field that cease to be measurable.
2. The vertical current distribution is thicker, and the peak current density centered higher than that of previous measurements.
3. A second layer occasionally may exist, centered between 140 and 145 km near the center of the electrojet, although the evidence is not conclusive.
4. The finite width of the electrojet causes a decrease in the magnetic field change seen at the ground. Taking this into account, good correlation was found in India between ground data and flight data.
5. Since no reverse currents were observed on the flights at the time of the maximum negative effect of the lunar current system, it appears that the lunar current system is either a modulation of the normal current, or that it may exist at a higher altitude. (This is unlikely

because of the lower conductivity.)

6. Maximums of electron density were correlated with maximums of current density, although the reverse was not always evident.
7. Nighttime currents are small, with the total magnetic effect being less than 10γ.

Evidence was found to support the theory that, if the length of the Langmuir probe in the direction of the magnetic field is smaller than the average gyration diameter of the electrons, the probe current will be independent of magnetic fields. I the length along the field is larger than the average gyration diameter, then the current will be dependent on the gyration diameter.

It was also observed that for the S_q current system:

1. In low latitudes the S_q current can exist in two layers, one centered about 100 km in altitude and the other about 120 km in altitude.
2. A reverse or negative current was found to exist close to the electrojet, and at the same altitude as the main current of the electrojet, which may be a return from the electrojet.

REFERENCES

Aikin, A. C. and S. J. Bauer, The ionosphere, Introduction to Space Science, ed. by W. N. Hess, 133-164, Gordon and Breach, New York, 1965.

Baker, W. G., electric currents in the ionosphere, II, the atmospheric dynamo, Phil. Trans. Roy. Soc. London, A, 246, 294-305, 1953.

Baker, W. G. and D. F. Martyn, Electric currents in the ionosphere, I, the conductivity, Phil. Trans. Roy. Soc. London, A, 246, 281-293, 1953.

Balsley, B. B., Some additional features of radar returns from the equatorial electrojet, J. Geophys. Res., 70, 3175-3182, 1965.

Balsley, B. B., Evidence of a stratified echoing region at 150 km in the vicinity of the magnetic equator during daylight hours, J. Geophys. Res., 69, 1925-1930, 1964.

Belrose, J. S., L. R. Bodė, and L. W. Hewitt, Physical properties of the polar winter mesosphere obtained from low-frequency propagation and partial reflection studies, Radio Science Journal of Research, N. B. S., 68, 1319-1323, 1964.

Blumle, L. J., A. C. Aikin, and J. E. Jackson, Rocket observations of the equatorial ionosphere, Report on Equatorial Aeronomy, ed. by F. De Mendonca, 86-87, 1965.

Bowles, K. L., B. B. Balsley, and R. Cohen, Field-aligned E-region irregularities identified with acoustic plasma waves, J. Geophys. Res., 68, 2485-2501, 1963.

Bowles, K. L. and R. Cohen, A study of radio wave scattering from sporadic E near the magnetic equator, Ionospheric Sporadic E ed. by E. K. Smith and S. Matsushita, 51-77, MacMillan, New York, 1962.

Burrows, K. and S. H. Hall, Rocket measurements of the geomagnetic field above Woomera, South Australia, J. Geophys. Res., 70, 2149-2152, 1965.

Cahill, L. J., Jr., Technique for ionospheric current measurements, pub. NASA for COSPAR Work Group II for IQSY, 1964.

Cahill, L. J., Jr., Investigation of the equatorial electrojet by rocket magnetometer, J. Geophys. Res., 64, 489-503, 1959.

Cahill, L. J., Jr., and J. A. Van Allen, New rocket measurements of ionospheric currents near the geomagnetic equator, J. Geophys. Res., 63, 270-273, 1958.

Cahill, L. J., Jr., and J. A. Van Allen, High altitude measurements of the earth's magnetic field with a proton precession magnetometer, J. Geophys. Res., 61, 547-558, 1956.

Chapman, S., Rockets and magnetic exploration of the ionosphere, Rocket Exploration of the Upper Atmosphere, R. L. Boyd and M. J. Seaton (editors), Pergammon Press, London, 292-305, 1954.

Chapman, S., The equatorial electrojet as detected from the abnormal electric current distribution above Huancayo, Peru, and elsewhere, Arch. Meteorol. Geophys. Bioklimatol., A, 44, 368-390, 1951.

Chapman, S. and J. Bartels, Geomagnetism vol. I and II, Clarendon Press, Oxford, 1940.

Cohen, R. and K. L. Bowles, The association of plane-wave electron-density irregularities with the equatorial electrojet, J. Geophys. Res., 68, 2503-2525, 1963.

Davis, T. N., J. D. Stolarik, and J. P. Heppner, Rocket measurements of S_q currents at mid-latitude, J. Geophys. Res., 70, 5883-5894, 1964.

Davis, T. N. and M. Sugiura, Auroral electrojet activity index AE and its universal time variations, Goddard Space Flight Center Report X612-65-264, June, 1965.

Driscoll, R. L. and P. L. Bender, Gyromagnetic ratio of proton re-determined, N. B. S. Tech. News Bull., 42, 217-219, 1958.

Egan, R. D. and A. M. Peterson, Backscatter observations of sporadic E, Ionospheric Sporadic E, ed. by E. K. Smith and S. Matsushita, 89-109, MacMillan, New York, 1962.

Elsasser, W. M., Hydromagnetic dynamo theory, Rev. Mod. Phys., 28, 135-163, 1956.

Farley, D. T., Jr., A plasma instability resulting in field-aligned irregularities in the ionosphere, J. Geophys. Res., 68, 6083-6097, 1963.

Finch, H. F. and B. R. Leaton, The earth's main magnetic field, epoch 1955, Monthly Notices, Roy. Astron. Soc., Geophys. Suppl. 1, 314-317, 1957.

Forbush, S. E. and M. Casaverde, Equatorial electrojet in Peru, Carnegie Inst., Wash. Publ. 620, 1961.

Langmuir, I. and H. M. Mott-Smith, Studies of electric discharges in gases at low pressures, G. E. Review, 27, 449-455; 538-548; 616-623; 762-771; 810-820, 1924.

Leaton, B. R., S. R. C. Malin, and M. J. Evans, An analytical representation of the estimated geomagnetic field and its secular change for the epoch 1965.0, J. Geomag. and Geoelect., 17, 187-194, 1965.

Maeda, K. and H. Matsumoto, Conductivity of the ionosphere and current system, Rep. Ionosphere Space Res. Japan, Vol. 16, 1-26, 1962.

Matsushita, S., Lunar tidal variations of sporadic E, Ionospheric Sporadic E, ed. by E. K. Smith and S. Matsushita, 194-214, MacMillan, New York, 1962.

Maynard, N. C., L. J. Cahill, Jr., and T. S. G. Sastry, Preliminary results of measurements of the equatorial electrojet over India, J. Geophys. Res., 70, 1241-1245, 1965.

Mead, G. D., Deformation of the geomagnetic field by the solar wind, J. Geophys. Res., 69, 1181-1195, 1964.

Mott-Smith, H. M. and I. Langmuir, The theory of collectors in gaseous discharges, Phys. Rev., 28, 727-763, 1926.

Nobata, K., Characteristics of Langmuir probe in a strong magnetic field, Japanese J. of Appl. Phys., 2, 719-727, 1963.

Nordberg, W. and S. I. Rasool, Meteorology from space, Introduction to Space Science, ed. by W. N. Hess, 251-296, Gordon and Breach, New York, 1965.

Ogbuehi, P. O. and A. Onwumechilli, Daily and seasonal changes in the equatorial electrojet in Nigeria, J. Atmospheric Terrest. Phys., 26, 889-898, 1964.

Ogbuehi, P. O. and A. Onwumechilli, Recent measurements of the magnetic field of the equatorial electrojet in Nigeria, J. Geophys. Res., 68, 2421-2424, 1963.

Onwumechilli, A., A study of the equatorial electrojet - II, A model electrojet that fits H observations, J. Atmospheric Terrest. Phys., 13, 235-257, 1959.

Packard, M. and R. Varian, Free nuclear induction in the earth's magnetic field, Phys. Rev., 93, 341, 1954.

Pisharoty, P. R. and P. Y. Srinivasan, Width of the electrojet over South India, submitted to Indian J. Meteorol. Geophys., Sept. 1962.

Ratcliffe, J. A. and K. Weekes, The ionosphere, Physics of the Upper Atmosphere, ed. by J. A. Ratcliffe, 393-395, Academic Press, New York, 1960.

Rubens, S. M., Cube-surface coil for producing a uniform magnetic field, Rev. Sci. Inst., 16, 243-245, 1945.

Singer, S. F., E. Maple, and W. A. Bowen, Jr., Evidence for ionospheric current from rocket experiments near the geomagnetic equator, J. Geophys. Res., 56, 265-28-, 1951.

Smith, L. G., A DC probe for rocket measurements in the ionosphere, Geophys. Corp. Am. Tech. Rep. 63-19-N, June 1963.

Smith, L. G., A simple method of trajectory determination for sounding rockets, GCA Tech. Rep. No. 63-9-N, March, 1963.

Staff of Texas Instruments, Transistor Circuit Design, Chap. 8, McGraw-Hill, New York, 1963.

Stewart, B., Terrestrial magnetism, Encyclopedia Britannica, 9th ed. 36 pp., 1882.

Sugiura, M. and J. Cain, A model equatorial electrojet, submitted to J. Geophys. Res., Nov. 1965.

Sugiura, M. and S. Chapman, The average morphology of geomagnetic storms with sudden commencement, Abhandlungen der Akademie der Wissenschaften in Gottingen, Mathematisch-Physikalische, Klasse, Sonderheft Nr. 4, Vandenhoeck and Ruprecht, Gottingen, 1960.

Sugiura, M. and J. P. Heppner, The earth's magnetic field, Introduction to Space Science, ed. by W. N. Hess, 3-92, Gordon and Breach, New York, 1965.

Terman, F. E., Radio Engineers Handbook, McGraw-Hill, New York, 1943.

U. S. Standard Atmosphere, prep. under sponsorship of NASA, USAF, and U. S. Weather Bureau, Washington, D. C., 1962.

Vestine, E. H., The upper atmosphere and geomagnetism, Physics of the upper atmosphere, ed. by J. A. Ratcliffe, 471-512, Academic Press, New York, 1960.

Vestine, E. H., L. La Porte, I. Lange, and W. E. Scott, The geomagnetic field - description and analysis, Carnegie Institution of Washington Publ. 580, 1947.

Waters, G. S., A measurement of the earth's magnetic field by nuclear induction, Nature, 176, 691, 1955.

Waters, G. S. and P. D. Francis, A nuclear magnetometer, J. of Sci. Inst., 35, 88-93, 1958.

APPENDIX A

Trajectory determination presented a problem, in that no radar was available for the India flights. It was desirable to find a means of computing a variable g, free fall trajectory. The basic equation can be written as

$$m(t) \frac{d^2 y}{dt^2} = -m(t)\, g(y) \tag{A1}$$

where y is the vertical height above the earth,

g(y) is the acceleration due to gravity

m(t) is the mass of the vehicle

Employing the expression for the gravitational force, equation (A1) becomes

$$\frac{d^2 y}{dt^2} = \frac{C_1}{(y + C_2)^2} \tag{A2}$$

where C_1 and C_2 are known constants.

To integrate this, two transformations are made: first, $(y + C_2)$ is set equal to X, and second, since dy = dx,

$$\frac{d^2 x}{dt^2} = \frac{v dv}{dx} = \frac{C_1}{x^2}$$

Then carrying out the integrations, over x, one gets

$$v^2 = 2\left(\frac{C_1}{x} + C_3\right) \tag{A3}$$

where C_3 is an arbitrary constant.

In order that the velocity go to zero at apogee, C_3 must be a negative number. Define new constants: $2C_1 = K_1$, $-2C_3 = K_3$ (K_3 is arbitrary, K_1 is known). The expression now becomes

$$\frac{dx}{dt} = \frac{K_1 - K_3 x}{x} \tag{A4}$$

Two more transformations are necessary to easily integrate this: let $\frac{K_1}{K_3} = F^2$ and $\phi^2 = F^2 - x$.

$$-2 \sqrt{\frac{F^2 - \phi^2}{K_3}}\, d\phi = dt \tag{A5}$$

Integrating equation (A5), we get

$$\frac{1}{\sqrt{K_3}} \left[\phi\sqrt{F^2 - \phi^2} + F^2 \sin^{-1} \frac{\phi}{F} \right] = t + K_4' \tag{A6}$$

where K_4' is the second arbitrary constant.

This transforms back to

$$- \frac{K_1}{K_3\sqrt{K_3}} \frac{\sqrt{K_3 x}}{\sqrt{K_1}} \frac{\sqrt{K_1 - K_3 x}}{\sqrt{K_1}} + \sin^{-1} \frac{\sqrt{K_1 - K_3 x}}{\sqrt{K_1}} = t + K_4' \tag{A7}$$

A more condensed and convenient form is found by letting

$$R = \frac{K_3}{K_1}(x) = \frac{K_3}{K_1}(y + C_2)$$

$$\sqrt{R(1-R)} + \sin^{-1}\sqrt{1-R} = \frac{-K_3^{3/2}}{K_1}(t) + K_4 \tag{A8}$$

Here, K_3 and K_4 must be determined by the boundary conditions.

Baroswitch data give us the two times when the rocket is at

70,000 feet. The apogee time can be obtained from these by taking the mean of the two times. K_3 can easily be determined, if the apogee time (t_a) is known, from the equation (A3), (note $K_3 = -2C_3$) by noting that v = 0 at apogee. This leads to 1-R = 0 at t_a and that

$$R = \left(\frac{K_1}{t_a}\right)^{2/3}\left(\frac{y + C_2}{K_1}\right) K_4^{2/3} \tag{A9}$$

Using equations (A8) and (A9), and the time (given by the baro-switch), that the rocket passed 70,000,feet, K_4 can be determined.

The following program (Table A1) was written by Mrs. Marilyn Wingersky to calculate the times on each leg of the trajectory for any given Z, beginning at a specific altitude and incrementing until the apogee is reached. It was written in Fortran for the Load and Go subroutine for the IBM-1620 digital computer.

For each trajectory a data card is read in containing t_a (time of apogee in seconds) and Z (altitude in feet). K_4 is then computed by iteration as follows:

$$(K_4)_1 = 2$$

$$R = (K_4)_i^{2/3}\left[\frac{\left(\frac{K_1}{t_a}\right)^{2/3}}{K_1}\right]Z + C_2$$

$$(K_4)_{i+1} = \frac{\left/\sqrt{(1-R)R} + \tan^{-1}\left(\frac{\sqrt{1-R}}{\sqrt{R}}\right)\right/}{\left(1 - \frac{t}{t_a}\right)}$$

if $(K_4)_{i+1} - (K_4)_i > .0000001$,

set $(K_4)_{i+1} = (K_4)_i + .05\left((K_4)_{i+1} - (K_4)_i\right)$ and continue.

The times for the upward and downward legs are then computed, beginning with Z = 1.5 km and continuing every .5 km until R > 1, using equations (A10) and (A11).

$$t \text{ upward} = \left[\sqrt{(1-R)R} + \sin^{-1}\sqrt{1-R} - K_4\right]\left(\frac{-K_1}{K_3^{3/2}}\right) \qquad \text{(A10)}$$

$$t \text{ downward} = \left[-\sqrt{(1-R)R} - \sin^{-1}\sqrt{1-R} - K_4\right]\left(\frac{-K_1}{K_3^{3/2}}\right) \qquad \text{(A11)}$$

The altitude is then decreased by 2 kilometers, and the increment is multiplied by .1, and again the times are computed until R > 1. The distance is then decreased by the increment, and the increment is multiplied by .1. This is continued until the increment is less than .001. The output consists of t upward, t downward, and Z in kilometers.

TABLE A1

Rocket Trajectory Program

```
C       ROCKET FLIGHT, DETERMINES TIME AS A FUNCTION
C       OF DISTANCE
        HKON1=795866.
        C2=6378.388
   16   READ 1, TA,T,Z
        Z=.0003048006*Z
        TTH=2./3.
        HTT=3./2.
        GB=((HKON1/TA)**TTH)/HKON1
        GB=GB*(Z+C2)
        GAB=(1.-(T/TA))
        HKON4=.2
    2   R=(HKON4**TTH)*GB
        PUNCH 1, R
        RR=1.-R
        SE=SQRTF(RR*R)
        ER=SQRTF(RR/R)
        ERO=ATANF(ER)
        HKON5=SE+ERO
        HKON5=ABSF(HKON5)/GAB
        PUNCH 1, R,HKON5,SE,ER,ERO
        DF=ABSF(HKON4-HKON5)
        IF (DF-.0000005) 3,3,4
    4   HKON4=HKON4+.05*(HKON5-HKON4)
        PUNCH 1, HKON4
        GO TO 2
    3   HKON3=((HKON5*HKON1)/TA)**TTH
        PUNCH 1, TA,T,Z,HKON3,HKON5
        HKON4=HKON5
        CON2=6378.388
        W=HKON3/HKON1
        U=(HKON3*SQRTF(HKON3))/HKON1
        U=-1./U
   15   Z=1.
        ZINC=.5
   14   Z=Z+ZINC
        R=W*(Z+CON2)
        IF (R-1.) 5,5,6
    5   X=SQRTF(R-(R*R))
        Y=SQRTF(1.-R)
        Y=SINF(Y)
        S=ATANF(Y/SQRTF(1.-Y*Y))
        T=(X+S-HKON4)*U
        TT=(-X-S-HKON4)*U
        PUNCH 1, T,TT,Z
        GO TO 14
```

```
 6 IF (ZINC-.5) 20,21,21
21 Z=Z-2.
   ZINC=ZINC*.1
   GO TO 14
20 Z=Z-ZINC
   ZINC=ZINC*.1
   Z=Z-ZINC
   IF (ZINC-.001) 16,14,14
   END
```

APPENDIX B

Figure A1 shows the comparisons between the various means of trajectory determination for the UNH 65-5, at altitudes between 14 and 35 km. Radar plot-board data are rough results taken from a copy of the plot-board record. The computed radar is the final analysed radar track as supplied to us by NASA. The computed trajectory is that computed from the baroswitch times, using the program given in Appendix A. Densitometer data were converted from pressure to altitude using the U.S. Standard Atmosphere. It is noted that all methods are within two kilometers. Figure A2 depicts the region between 72 and 84 km of the same flight. The agreement between the methods is close until about 80 km, where the radar changes slope. Since this is well above appreciable atmosphere, it is believed that the radar is in error above this altitude.

Similar records are shown for UNH 65-3 in Figure A3. Here, the densitometer differs by almost two kilometers between 19 and 31 km. The radar and the baroswitch trajectories are within 0.3 km.

It is noted that the densitometer records are not always this close to the radar data. This might be improved with a more stable circuit and better calibration. It is useful in case all other means fail. The baroswitch proved to be a reliable means of trajectory determination and agreed closely with radar results where available.

APPENDIX C

The reduction of data from the flights resulted in the repetition of a number of similar calculations. The program for the trajectory (Appendix A) calculated a time for a given altitude. Since the time of each measurement was known and the altitude desired, it was necessary to interpolate between the calculated points. A program was written to do a linear interpolation for the altitude at a given time. The program was written in the Load and Go format for the IBM-1620 computer.

Three variations of the program were used. Table A2 lists the program for the calculation of the altitudes for the Langmuir probe measurements. N is the total number of data cards. The dimension is set by the number N. Line 100 is set to read the data cards in the form in which they are punched by the trajectory program. The times are then read in and the interpolation done for each one. It is to be noted that the times must be in sequence, continually increasing, and that the data cards must also be kept in sequence.

A similar program is shown in Table A3. In this case the times are read in with the number of each measurement (M) and the measured field (F). M and F are carried through and punched in the output for use in the next program. Since the data is to be used in a subsequent program, the Load and Go punch subroutine is used.

The theoretical field data were in a similar form, with the values being known every five kilometers. The third variation of the interpolation program is given in Table A4. Here, it was desired to find the theoretical field for the altitudes calculated by the

program in Table A3. The input data was that of the theoretical field F (K) at a given altitude Z (K). The information from the program in Table A3 was then read in and the theoretical field calculated for each point. The difference between the theoretical and the measured field was then taken and printed with the value for the theoretical field and the information read in.

TABLE A2

Program to Interpolate for the Altitude Corresponding to Each Langmuir Probe Measurement

```
C       LOAD AND GO INTERPOLATION -MAYNARD
C       N=NUMBER OF CARDS YOU INTERPOLATE WITH
        DIMENSION UPT(298),DOWNT(298),Z(298)
      1 READ 500, N
        DO 100 K=1,N
    100 READ 500, UPT(K),DOWNT(K),Z(K)
        READ 500, TIMES
      2 DO 8 K=2,N
        U=UPT(K)
        IF (TIMES-U) 3,7,8
      3 ZZ=Z(K)
        ALT=(Z(K-1)-ZZ)/(UPT(K-1)-U)
      4 ZP=(TIMES-U)*ALT+ZZ
      5 PRINT 500, ZP,TIMES
        READ 500, TIMES
        IF (TIMES) 6,1,6
      6 IF (TIMES-U) 4,7,8
      7 ZP=Z(K)
        GO TO 5
      8 CONTINUE
      9 IF (TIMES-DOWNT(N)) 10,10,12
     10 PRINT 500, Z(N),TIMES
        READ 500, TIMES
     11 IF (TIMES) 9,1,9
     12 DO 18 K=2,N
        M=N-K+1
        D=DOWNT(M)
        IF (TIMES-D) 13,17,18
     13 ZZ=Z(M)
        ALT=(Z(M+1)-ZZ)/(DOWNT(M+1)-D)
     14 ZP=(TIMES-D)*ALT+ZZ
     15 PRINT 500, ZP,TIMES
        READ 500, TIMES
        IF (TIMES) 16,1,16
     16 IF (TIMES-D) 14,17,18
     17 ZP=Z(M)
        GO TO 15
     18 CONTINUE
        END
```

TABLE A3

Program to Interpolate for the Altitude Corresponding to Each Magnetometer Measurement

```
C       LOAD AND GO INTERPOLATION -MAG -MAYNARD
C       N=NUMBER OF CARDS YOU INTERPOLATE WITH
        DIMENSION UPT(298),DOWNT(298),Z(298)
      1 READ 500, N
        DO 100 K=1,N
    100 READ 500, UPT(K),DOWNT(K),Z(K)
        READ 500, M,TIMES,F
      2 DO 8 K=2,N
        U=UPT(K)
        IF (TIMES-U) 3,7,8
      3 ZZ=Z(K)
        ALT=(Z(K-1)-ZZ)/(UPT(K-1)-U)
      4 ZP=(TIMES-U)*ALT+ZZ
      5 PRINT 500, M,TIMES,F,ZP
        READ 500, M,TIMES,F
        IF (TIMES) 6,1,6
      6 IF (TIMES-U) 4,7,8
      7 ZP=Z(K)
        GO TO 5
      8 CONTINUE
      9 IF (TIMES-DOWNT(N)) 10,10,12
     10 PRINT 500, M,TIMES,F,Z(N)
        READ 500, M,TIMES,F
     11 IF (TIMES) 9,1,9
     12 DO 18 K=2,N
        M=N-K+1
        D=DOWNT(M)
        IF (TIMES-D) 13,17,18
     13 ZZ=Z(M)
        ALT=(Z(M+1)-ZZ)/(DOWNT(M+1)-D)
     14 ZP=(TIMES-D)*ALT+ZZ
     15 PRINT 500, M,TIMES,F,ZP
        READ 500, M,TIMES,F
        IF (TIMES) 16,1,16
     16 IF (TIMES-D) 14,17,18
     17 ZP=Z(M)
        GO TO 15
     18 CONTINUE
        END
```

TABLE A4

Program to Interpolate for the Theoretical Field

```
C       LOAD AND GO INTERPOLATION -FIELD -MAYNARD
C       N=NUMBER OF CARDS YOU INTERPOLATE WITH
C       I=NUMBER OF THE APOGEE CARD
        DIMENSION Z(200),F (200)
      1 READ 500, N,I
        DO 100 K=1,N
    100 READ 500, Z(K),F(K)
        READ 500, M,T,F,ZS
      2 DO 9 K=2,I
        ZZ=Z(K)
        IF (ZS-ZZ) 3,8,9
      3 FF=F(K)
        FIELD=(F(K-1)-FF)/(Z(K-1)-ZZ)
      4 FT=(ZS-ZZ)*FIELD+FF
      5 DIFF=F-FT
        PRINT 500, M,T,F,FT,DIFF,ZS
        ZSI=ZS
        READ 500, M,T,F,ZS
        IF (ZS) 6,1,6
      6 IF (ZS-ZSI) 10,7,7
      7 IF (ZS-ZZ) 4,8,9
      8 FT=F(K)
        GO TO 5
      9 CONTINUE
     10 J=I+1
     11 DO 18 K=J,N
        ZZ=Z(K)
        IF (ZS-ZZ) 18,17,13
     13 FF=F(K)
        FIELD=(F(K-1)-FF)/(Z(K-1)-ZZ)
     14 FT=(ZS-ZZ)*FIELD+FF
     15 DIFF=F-FT
        PRINT 500, M,T,F,FT,DIFF,ZS
        READ 500, M,T,F,ZS
        IF (ZS) 16,1,16
     16 IF (ZS-ZZ) 18,17,14
     17 FT=F(K)
        GO TO 15
     18 CONTINUE
        END
```

APPENDIX D

Tables A5 and A6 give the main program and function subroutine for the calculation of the magnetic field from a model electrojet, given the function of the vertical current distribution. The program, written in Fortran II for the IBM-1620 computer by Mrs. Marilyn Wingersky, does the integration over the vertical distribution numerically by the method of Gaussian quadratures.

The expression for the vertical current distribution (BQZ) is placed in the function BXBY subroutine given in Table A6. The subroutine object deck is read in with the main program object deck and is automatically called by the main program when needed in the calculation. The information read in by the main program in statement 1 consists of the total number of data cards read in by the second read statement (N), the limits of the width of the electrojet in kilometers (X_1 and X_2), the limits of the integration over the vertical coordinate in kilometers (Y_1 and Y_2), and any constant additional field in the X direction which is desired to be added to the calculated magnetic field (BXE). The second read statement reads the coordinates of the point at which the field is to be calculated.

As the program now reads, stored information is lost during the calculation, and the program must be read into the computer for each A and B at which the calculation is desired. Time for each calculation on the IBM-1620 is about two minutes. Another suggestion for improvement is to read in BXE in the second read statement, so that it can be varied for each set of coordinates A and B for which the calculation is made.

TABLE A5

Electrojet Model Program

```
      DIMENSION W(4),T(2),T1(4)
      W(1)=.34785483
      W(2)=.65214516
      W(3)=.65214516
      W(4)=.34785483
      T(1)=-.86113633
      T(2)=-.33998100
1     READ 100, N,X1,X2,Y1,Y2,BXE
100   FORMAT(I3,5F10.2)
      DO 3 JJ=1,N
      READ 101, A,B
101   FORMAT(2F10.2)
      X11=X1-B
      X22=X2-B
      H=(Y2-Y1)*.16666667
      HP=H*.5
      T1(1)=T(1)*HP
      T1(2)=T(2)*HP
      T1(3)=-T1(2)
      T1(4)=-T1(1)
      SPX=0.
      SPY=0.
      DO 2 J=1,6
      G=(2.*Y1+H)*.5
      Y1=Y1+H
      DO 2 K=1,4
      T10=T1(K)+G
      T11=W(K)
      SPX=SPX+T11*BXBY(X11,X22,A,T10,1)
2     SPY=SPY+T11*BXBY(X11,X22,A,T10,2)
      SPX=HP*SPX
      SPY=HP*SPY
      T10=BXE+SPX
      B1=SQRTF(T10*T10+SPY*SPY)
3     PRINT 102,X1,X2,Y1,Y2,A,B,B1,SPX,SPY
102   FORMAT(6F10.2,3E17.8)
      GO TO 1
      END
```

TABLE A6

Electrojet Model Program Subroutine

```
      FUNCTION BXBY(X11,X22,A,Y,L)
      BQZ=32.142*EXPF(-.064577*Y)*((SINF(.064577*Y))**4)
      S10=Y+A
      GO TO (1,12),L
1     IF (S10) 2,3,2
2     BXBY=BQZ*2.*(ATANF(X22/S10)-ATANF(X11/S10))
      RETURN
3     IF (X22) 4,5,6
4     S1=-1.5707963
      GO TO 7
5     S1=0.
      GO TO 7
6     S1=1.5707963
7     IF (X11) 8,9,10
8     S2=-1.5707963
      GO TO 11
9     S2=0.
      GO TO 11
10    S2=1.5707963
11    BXBY=BQZ*2.*(S1-S2)
      RETURN
12    S10=S10*S10
      BXBY=BQZ*LOGF((X22*X22+S10)/(X11*X11+S10))
      RETURN
      END
```

FIGURE CAPTIONS

Figure 1. World maps of the ionospheric current systems corresponding to the solar daily magnetic variations in the sunspot minimum year 1902. The top chart is at the time of the equinoxes and the bottom at the June solstice (taken from Chapman and Bartels (1940) page 229).

Figure 2. Variation of the product of the number density of electrons and the various normalized conductivities (normalized by removing electron density variations) with altitude as calculated by Baker and Martyn (1953).

Figure 3. Block diagram of the UNH rocket magnetometer payload.

Figure 4. Picture and layout diagram of the payload, showing the location of each major instrument.

Figure 5. Photograph of the densitometer unit mounted on the antenna base section. The photograph also shows the bottom of the raceway with Cannon connectors for each deck.

Figure 6. Block diagram of the UNH proton precession magnetometer.

Figure 7. Photograph of the sensor coil showing it in its various stages of construction.

Figure 8. Drawing of the electrostatic shield used to encase the sensor coil for reduction of noise pickup.

Figure 9. Schematic of the preamplifier unit showing the preamplifier, programmer, associated relaying and the clipping network.

Figure 10. Schematic of the main tuned amplifier.

Figure 23. Magnetogram from Trivandrum, India, between 0830 and 2000 hours local time on January 27, 1964. Time of launch of UNH 64-2 is indicated.

Figure 24. Magnetogram from Trivandrum, India, of H, D, and V variations between 1000 and 2100 hours local time on January 29, 1964. Time of launch of UNH 64-3 is indicated.

Figure 25. Magnetograms from Trivandrum, India, of H, D, and V variations between 1500 hours, January 31, 1964, and 0300 hours, February 1, 1964. Launch time of UNH 64-4 is noted.

Figure 26. Map of Peru showing the location of the four flights. Also shown are several estimates of the magnetic dip equator and the locations of the magnetic observatories of Canete, Huancayo, Huanuco, and Casma.

Figure 27. Magnetograms from the Peruvian stations of Huanuco, Casma and Canete for March 9, 1965. The launch time of UNH 65-2 is noted.

Figure 28. Magnetograms from the Peruvian stations of Huanuco, Casma and Canete for March 10, 1965. Indicated by the arrows is the launch time of UNH 65-3.

Figure 29. Magnetograms from the Peruvian stations of Huanoco, Casma and Canete for March 11, 1965.

Figure 30. Magnetograms from the Peruvian stations of Huanuco, Casma and Canete for March 12, 1965. The times of launch of UNH 65-4 and UNH 65-5 are noted.

Figure 40. UNH 64-1 Langmuir probe current (proportional to electron density) as a function of altitude in kilometers. Note that there are two vertical and two horizontal scales.

Figure 41. The difference between the measured field and the UNH 64-4 measured field in gammas as a function of altitude in kilometers for UNH 64-3.

Figure 42. UNH 64-3 current density in amp/km^2 (derived from the slope of the difference curve in Figure 41), plotted against altitude in kilometers.

Figure 43. UNH 64-3 Langmuir probe current (proportional to electron density) as a function of altitude in kilometers. There are two vertical scales.

Figure 44. The difference between the measured field and the Leaton and Evans field in gammas for UNH 65-5, plotted against the altitude in kilometers.

Figure 45. The current density derived from the slope of Figure 44 in amp/km^2 versus the altitude in kilometers.

Figure 46. The difference between the UNH 65-4 measured field and the Leaton and Evans theoretical field in gammas as a function of altitude in kilometers.

Figure 47. UNH 65-4 current density (derived from the slope of Figure 46) in amp/km^2 versus the altitude in kilometers.

Figure 48. Langmuir probe current (proportional to electron density) in microamperes as a function of altitude in kilometers for the upward leg of UNH 65-5. Ionogram profiles before and after the flight with the corresponding scale

of electron density are shown for comparison (calculated by J. W. Wright of ESSA).

Figure 49. UNH 65-5 downward leg Langmuir probe current as a function of altitude. The ionogram profiles before and after flight are also plotted.

Figure 50. Langmuir probe current measured by UNH 65-4, plotted against altitude for the upward leg. Also plotted are the ionogram profiles.

Figure 51. The downward leg of UNH 65-4 Langmuir probe current versus altitude profile. Also plotted are the ionogram profiles.

Figure 52. The difference between the measured field of UNH 65-2 and the Leaton and Evans field in gammas as a function of altitude in kilometers. The arrows over the curves denote times of maximum positive effect of the precession and those under the curves the maximum negative effect.

Figure 53. The current density versus altitude profile derived from Figure 52 for flight UNH 65-2.

Figure 54. The difference between the UNH 65-3 measured field and the Leaton and Evans theoretical field in gammas, plotted against the altitude in kilometers.

Figure 55. UNH 65-3 current density in amp/km^2 (derived from the slope of Figure 54) as a function of the altitude in kilometers.

Figure 56. Langmuir probe current in microamperes (proportional to electron density) plotted against altitude for the upward leg of UNH 65-2. The ionogram profile calculated by J. W. Wright of ESSA is shown for comparison.

Figure 57. Langmuir probe current in microamperes as a function of the altitude for the downward leg of UNH 65-2. The comparison to the ionogram profile is shown.

Figure 58. The downward leg of the UNH 65-3 Langmuir probe current versus altitude profile. Comparison is shown to the ionogram profiles before and after flight.

Figure 59. UNH 65-3 Langmuir probe current for the upward leg as a function of the altitude. The ionogram profiles are plotted with the corresponding electron density scale.

Figure 60. A plot of σ_3, calculated from values of σ_1 and σ_2 given in the graphs of Maeda and Matsumoto (1962), versus altitude.

Figure 61. Profiles of constant conductivity σ_{yy} about the electrojet over Peru, plotted against altitude on the vertical scale and latitude on the horizontal scale, as calculated by Sugiura and Cain (1965). Note that the horizontal scale is compressed by a factor of 20 and that north is to the right of the graph.

Figure 62. The magnetic field calculated from a model electrojet versus altitude showing the effect of the variation of the width of the electrojet.

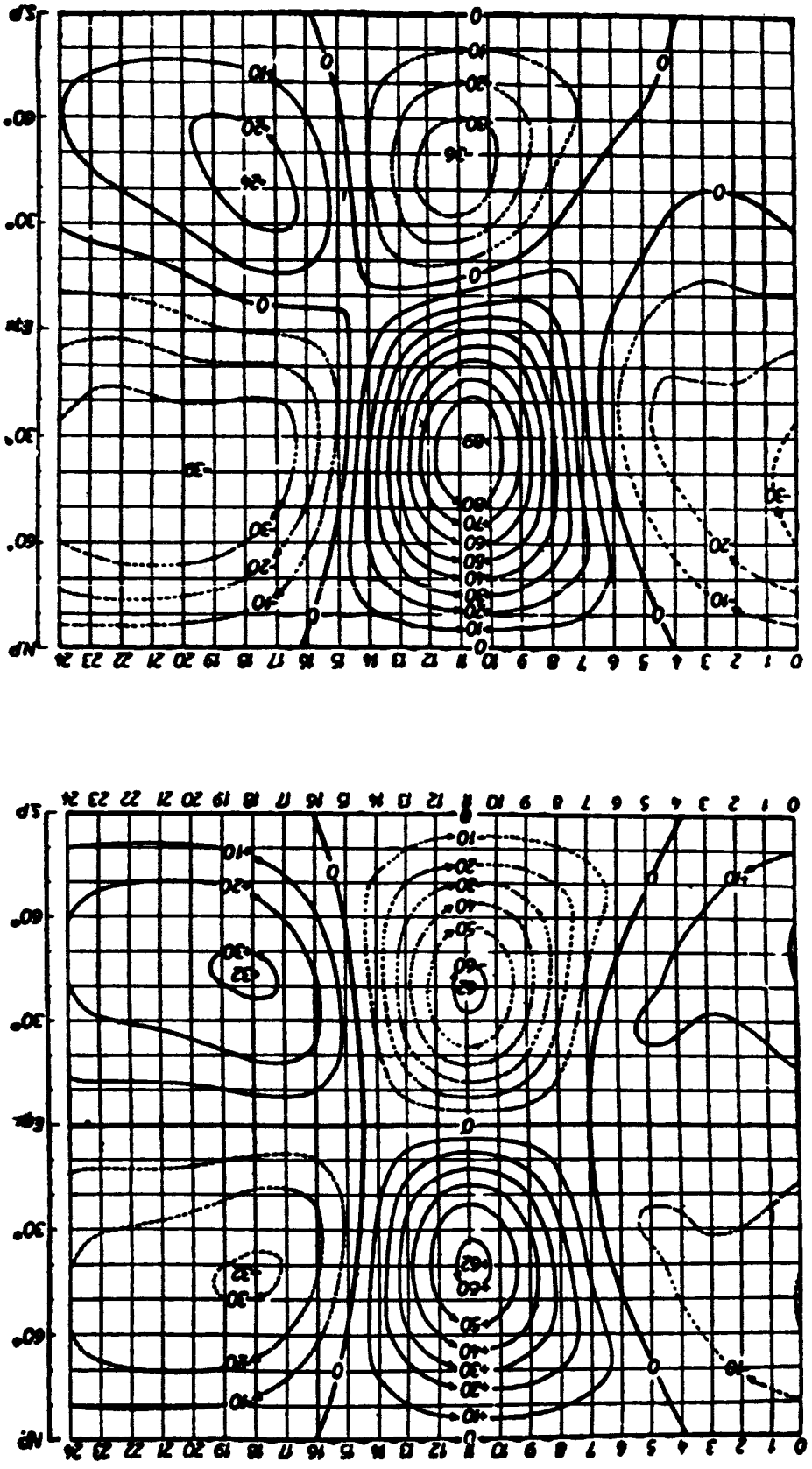

Figure 1

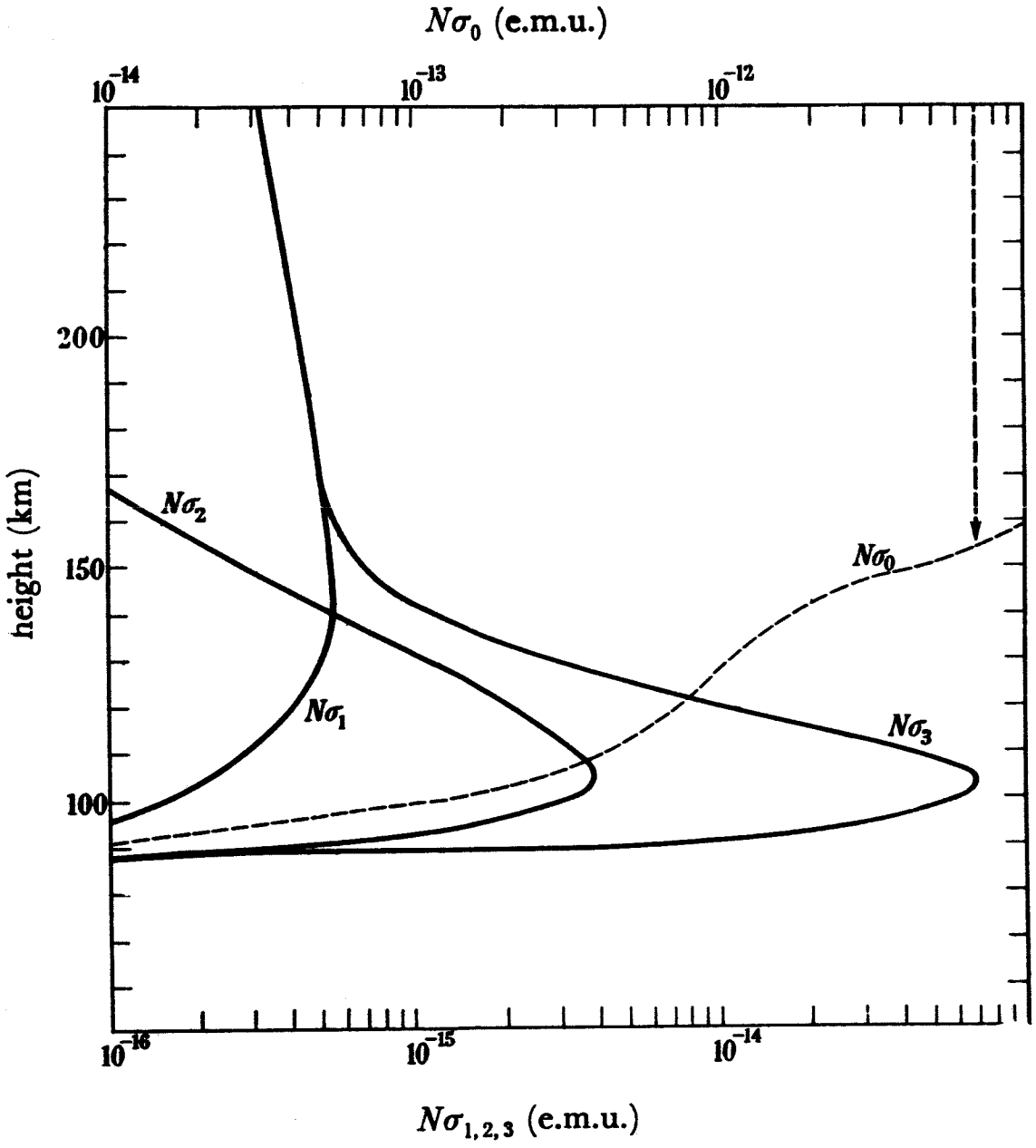
$N\sigma_0$ (e.m.u.)
10^{-14}
10^{-13}
10^{-12}
200
150
100
height (km)
$N\sigma_2$
$N\sigma_0$
$N\sigma_1$
$N\sigma_3$
10^{-16}
10^{-15}
10^{-14}
$N\sigma_{1,2,3}$ (e.m.u.)

Figure 2

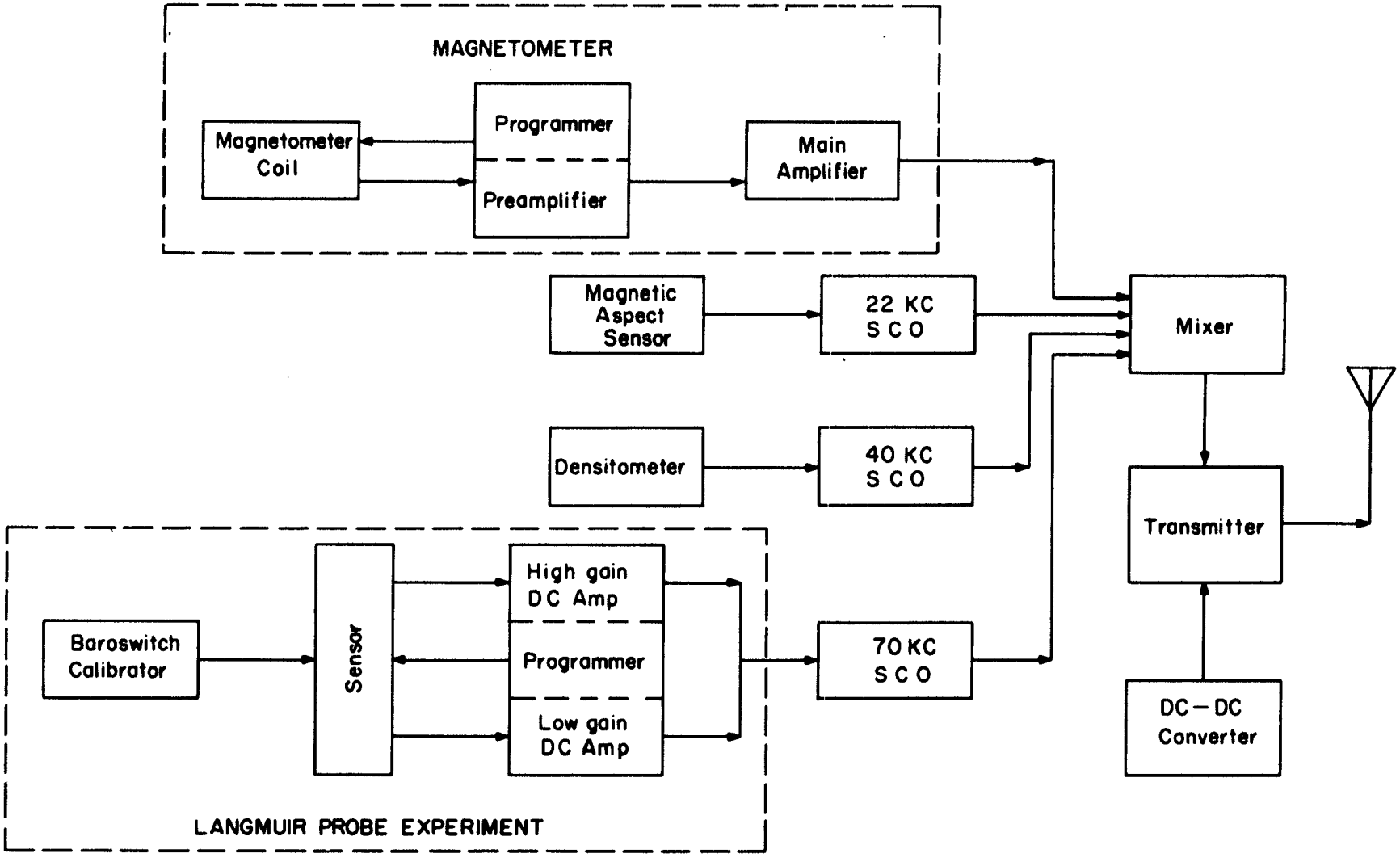

BLOCK DIAGRAM — UNH ROCKET MAGNETOMETER PAYLOAD

Figure 3

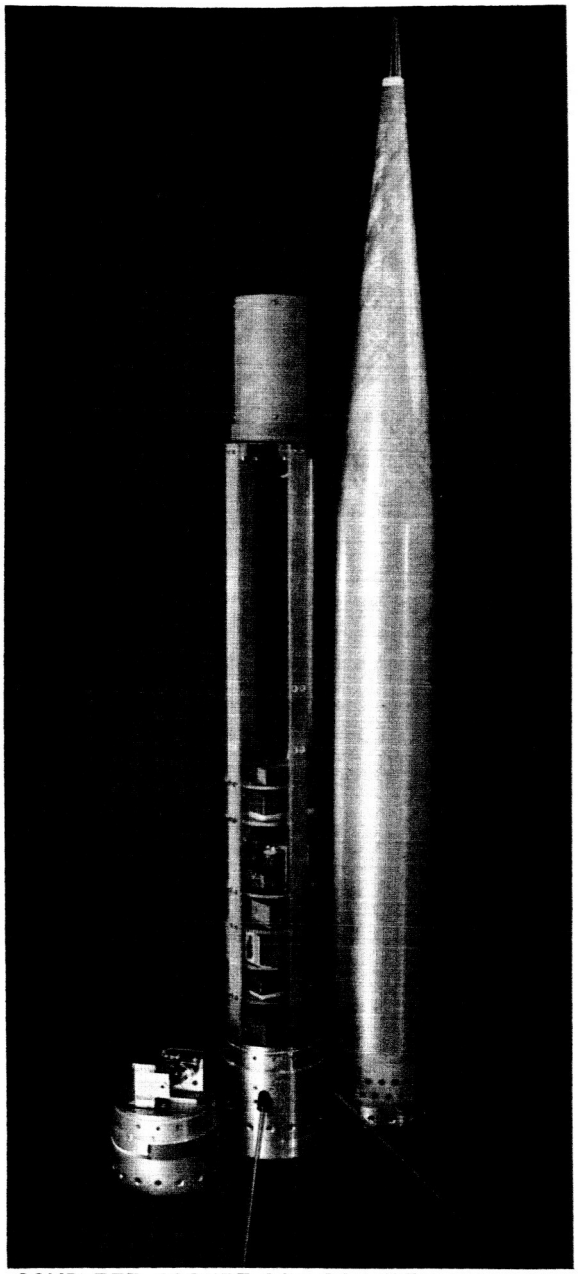

COMPLETE ROCKET PAYLOAD WITH NOSE CONE

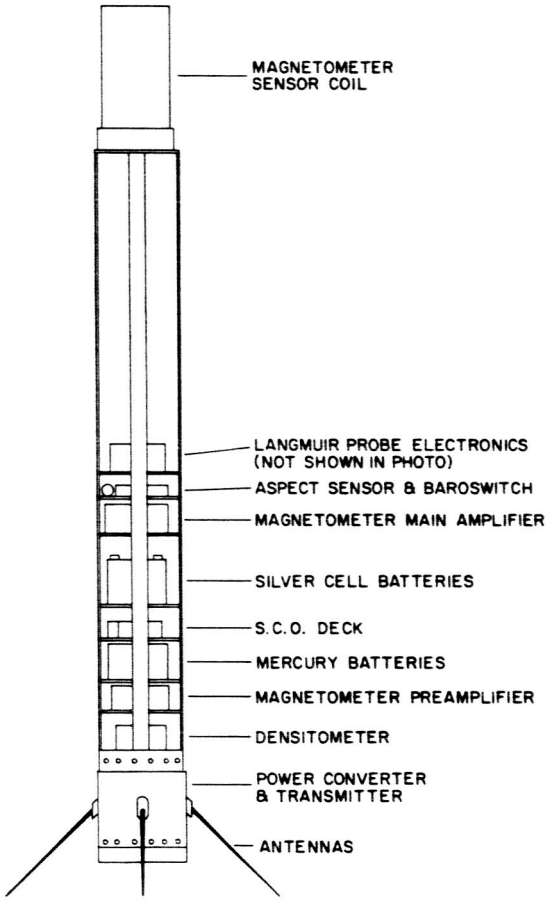

Figure 4

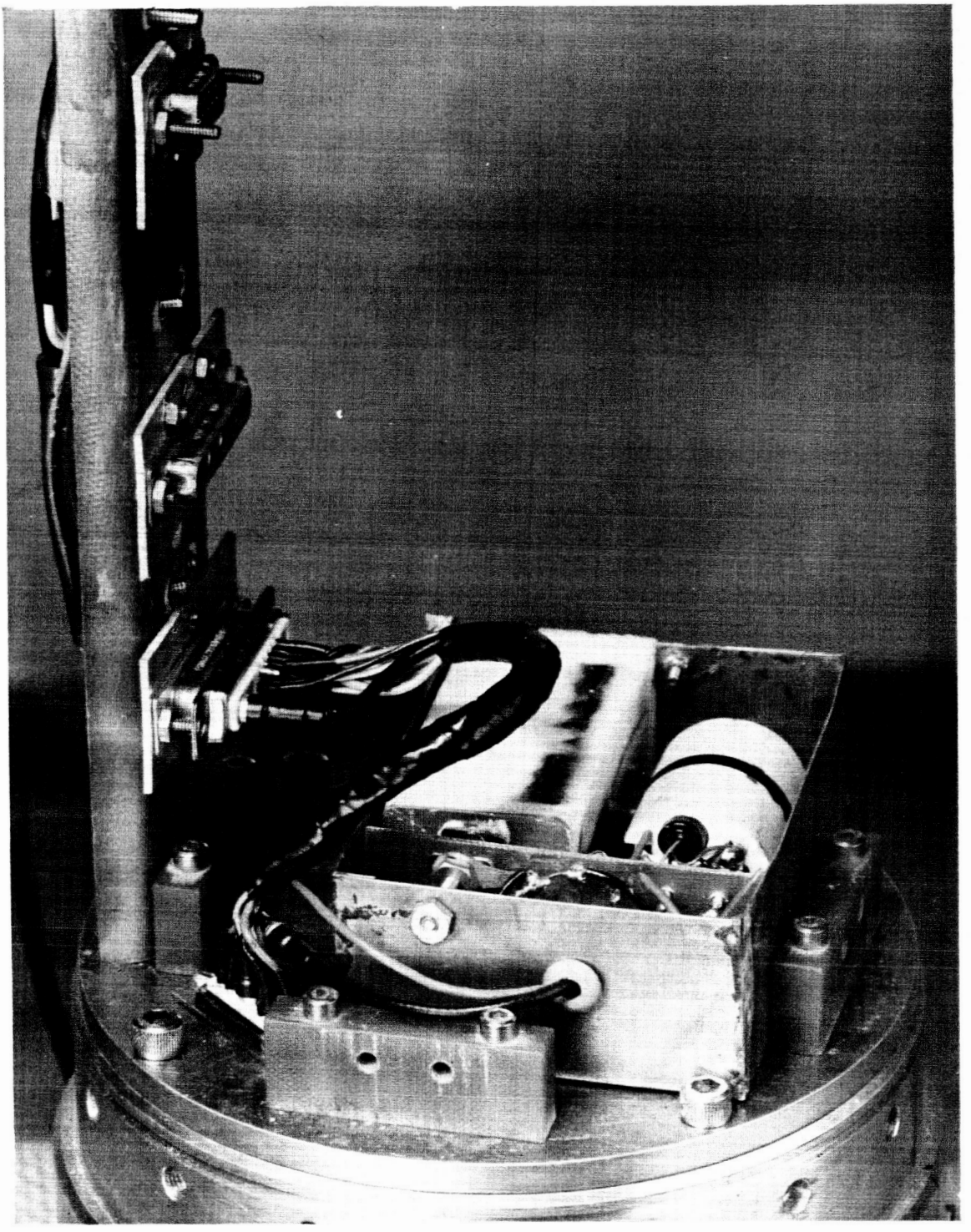

Figure 5

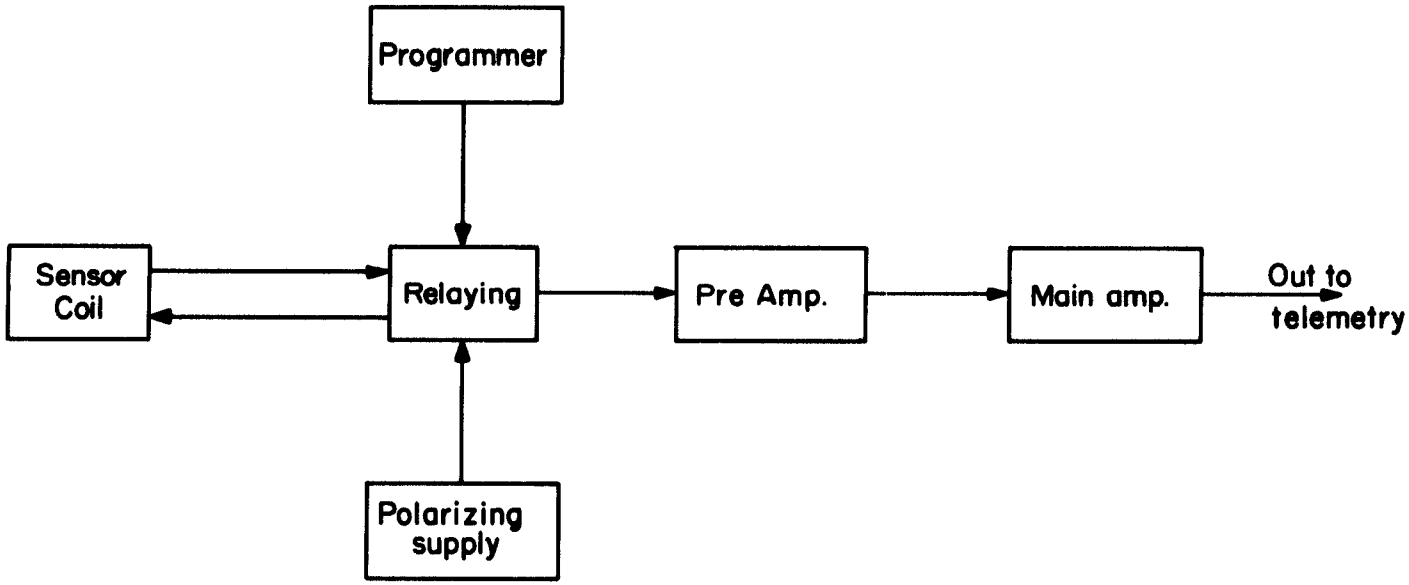

MAGNETOMETER BLOCK DIAGRAM

Figure 6

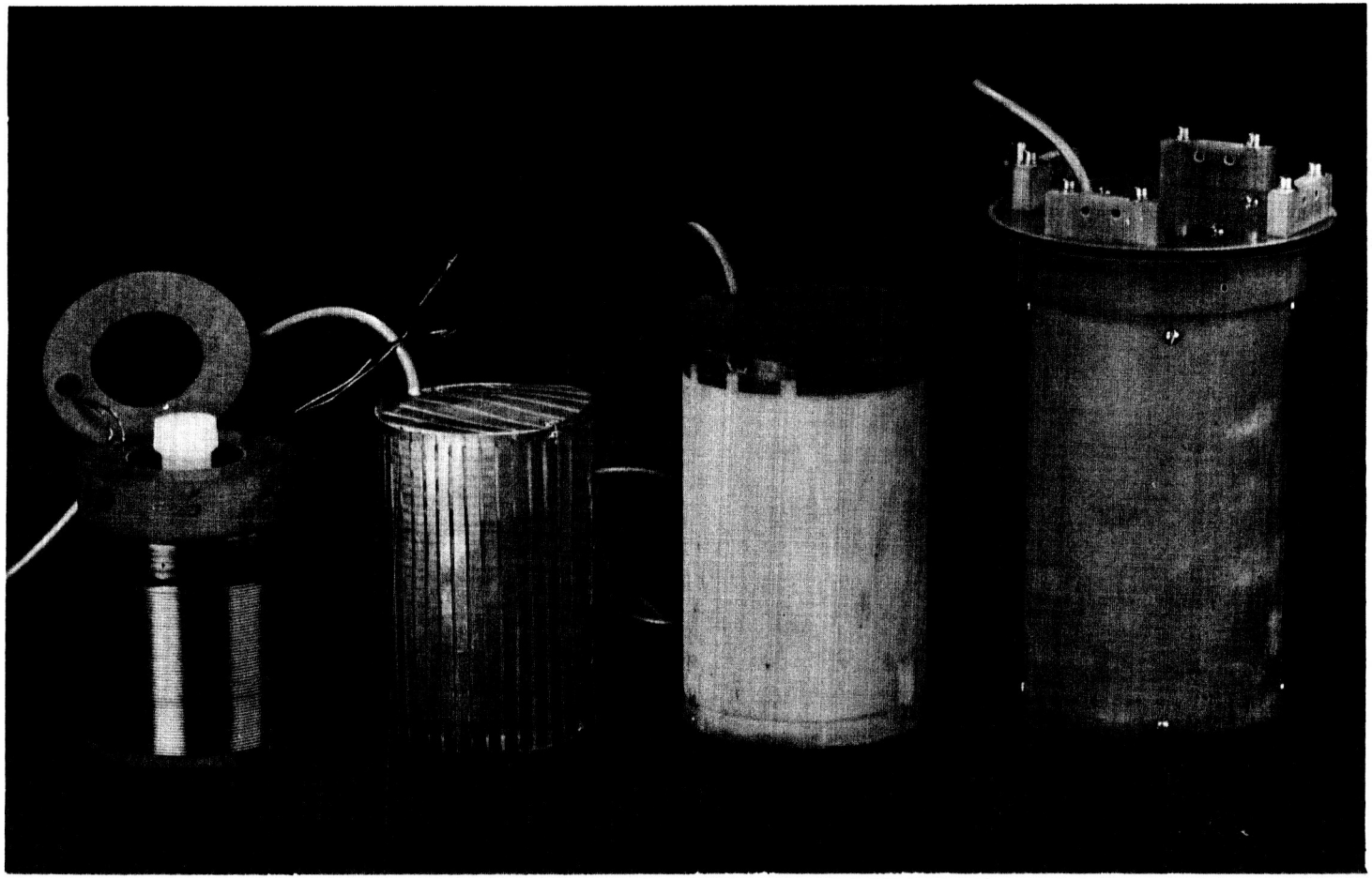

Figure 7

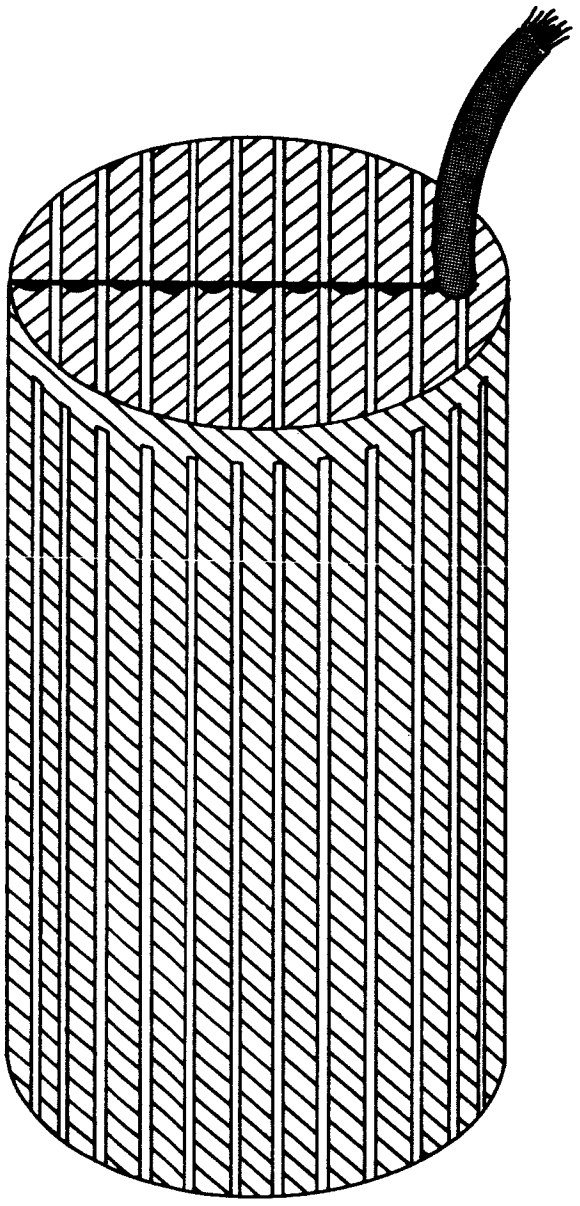

SENSOR WITH ELECTRO STATIC SHIELD

Figure 8

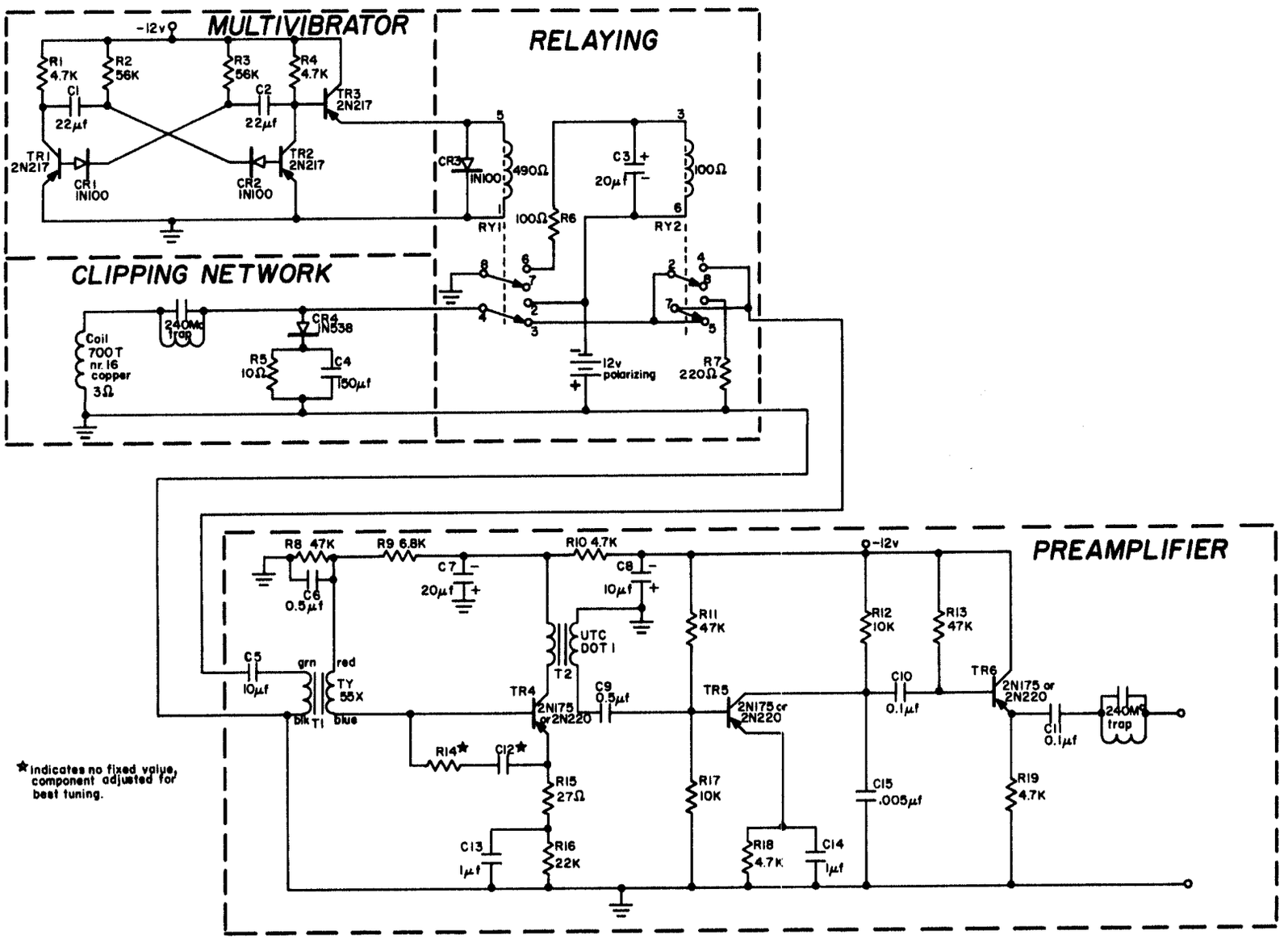
MULTIVIBRATOR
-12v
R1 4.7K
R2 56K
R3 56K
R4 4.7K
C1 22μf
C2 22μf
TR3 2N217
TR1 2N217
TR2 2N217
CR1 IN100
CR2 IN100
RELAYING
CR3 IN100
490Ω
100Ω
C3 20μf
100Ω
RY1
RY2
100Ω R6
CLIPPING NETWORK
Coil 700T nr.16 copper 3Ω
240Mc trap
CR4 IN538
R5 10Ω
C4 150μf
12v polarizing
R7 220Ω
PREAMPLIFIER
R8 47K
R9 6.8K
R10 4.7K
C6 0.5μf
C7 20μf
C8 10μf
-12v
R11 47K
R12 10K
R13 47K
C5 10μf
grn
red
TY 55X
blk
T1
blue
UTC DOT 1
T2
TR4 2N175 or 2N220
C9 0.5μf
TR5 2N175 or 2N220
C10 0.1μf
TR6 2N175 or 2N220
C11 0.1μf
240Mc trap
R14★
C12★
R15 27Ω
R16 22K
C13 1μf
R17 10K
R18 4.7K
C14 1μf
C15 .005μf
R19 4.7K
★Indicates no fixed value, component adjusted for best tuning.

Figure 9

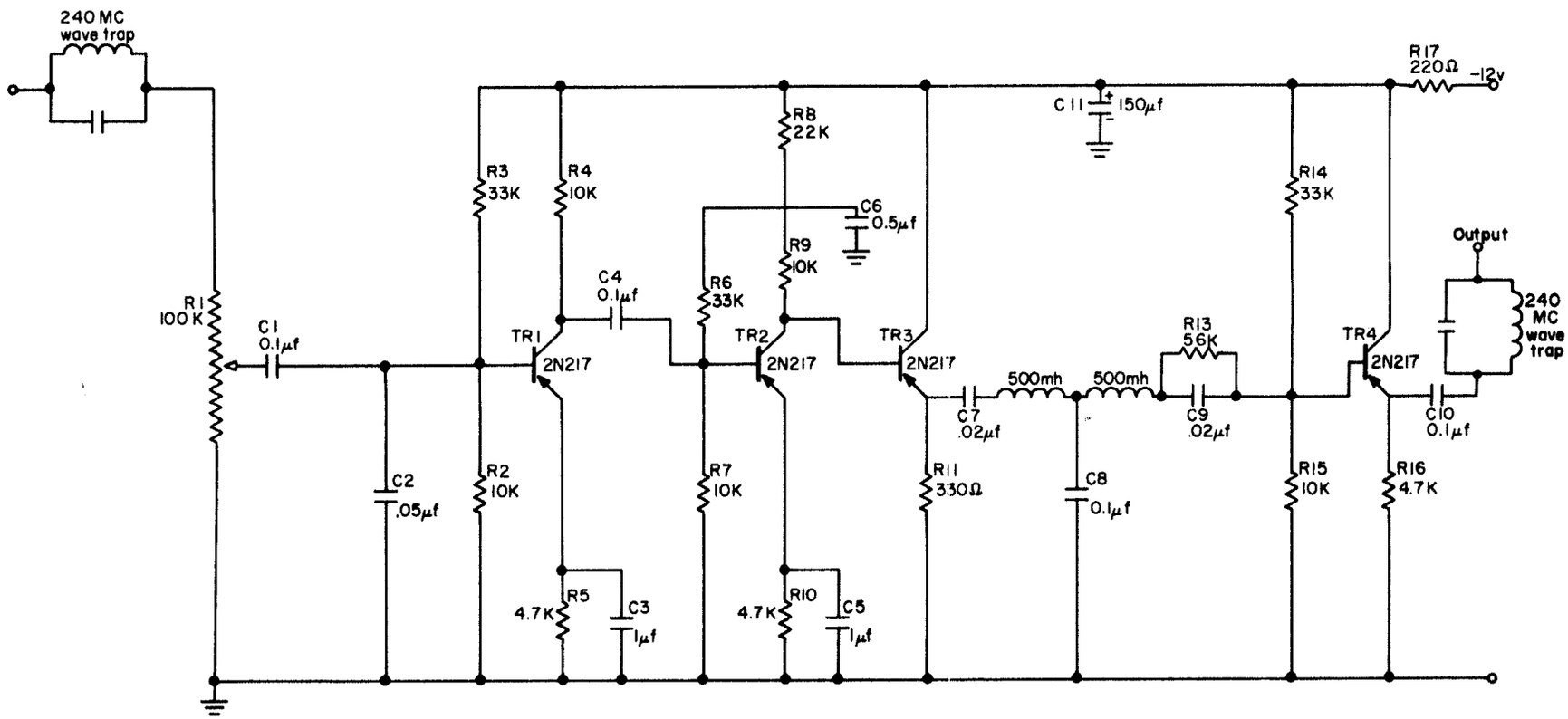

MODIFIED MAIN AMPLIFIER

Figure 10

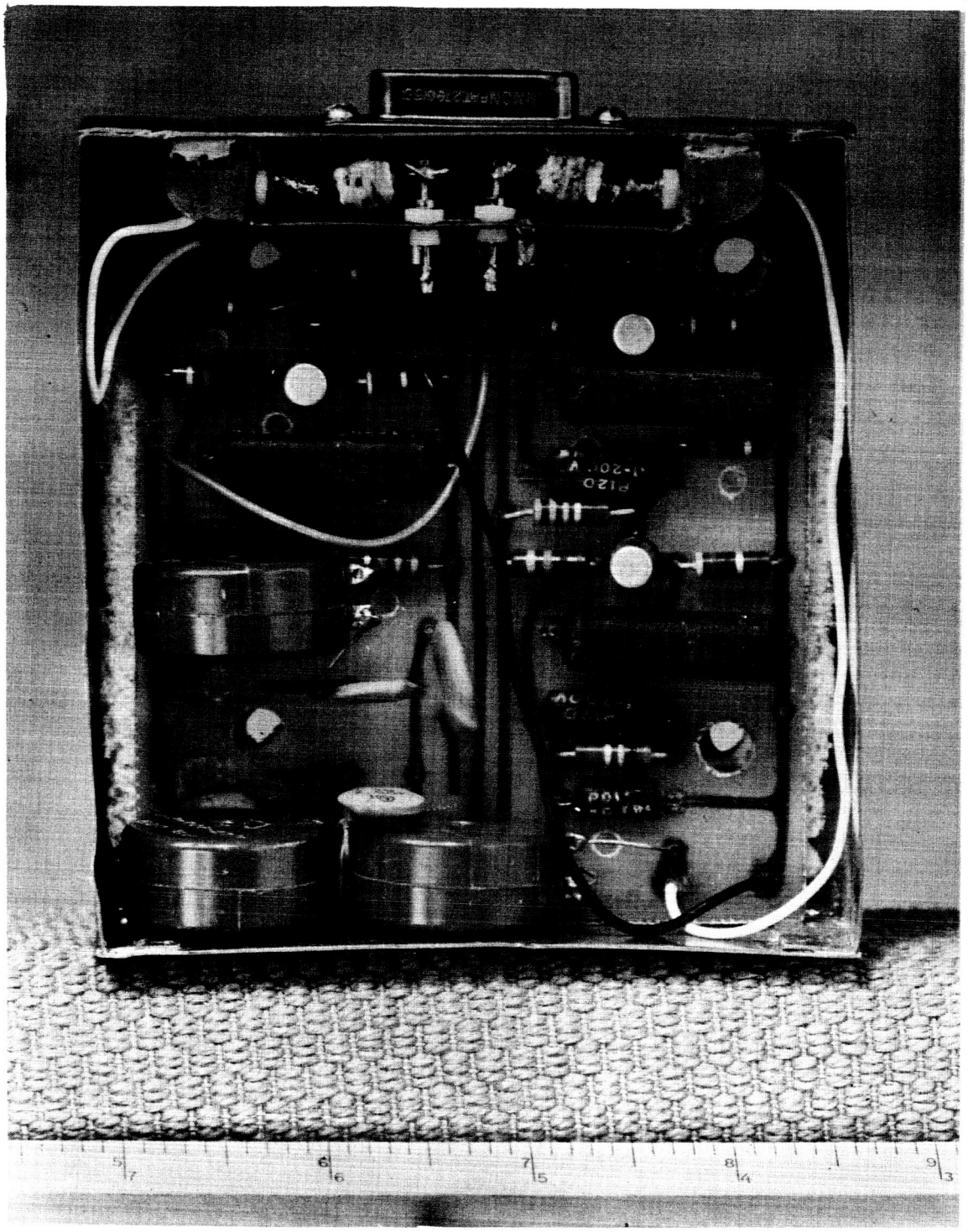

Figure 11

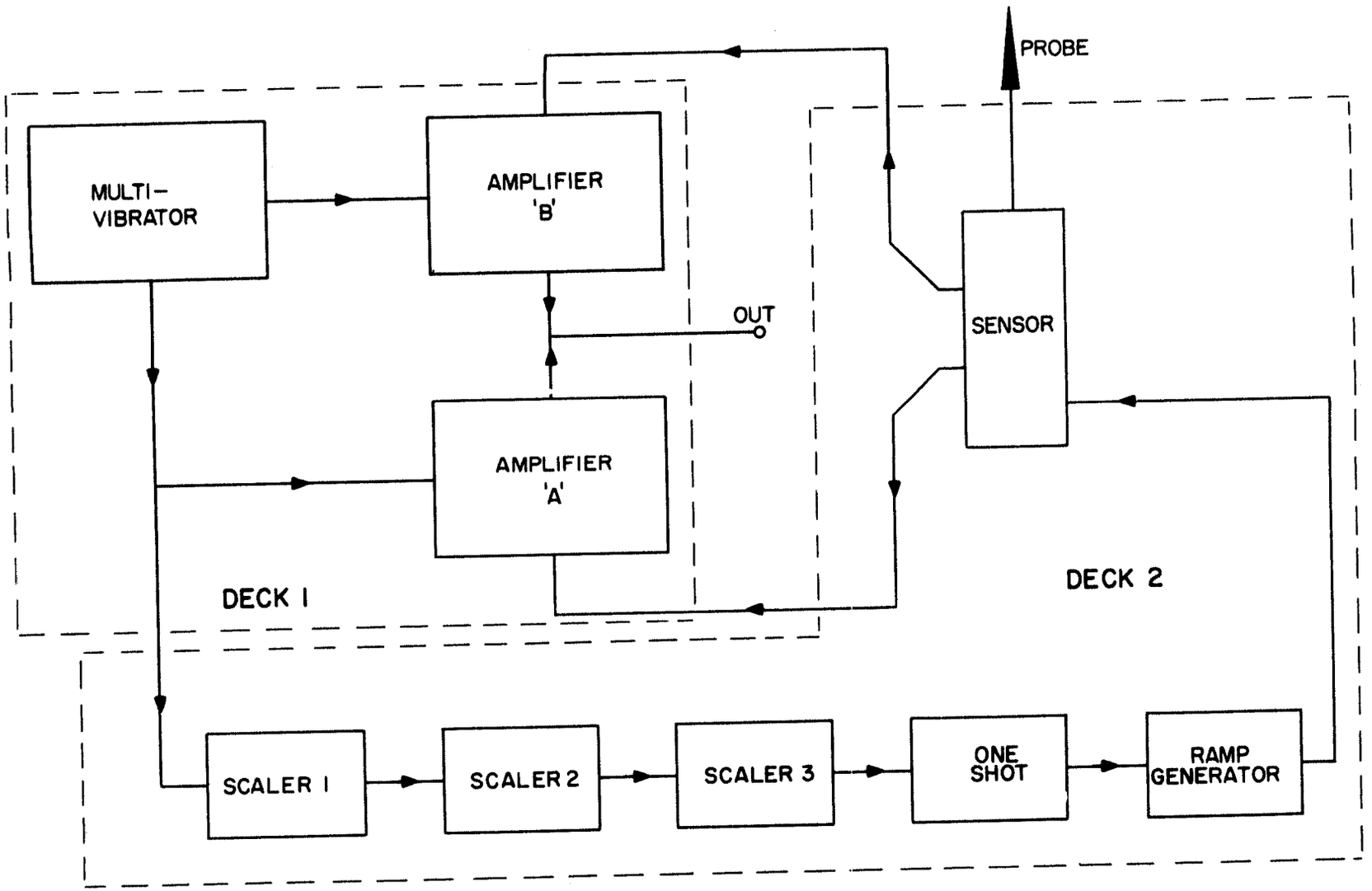

LANGMUIR PROBE BLOCK DIAGRAM

Figure 12

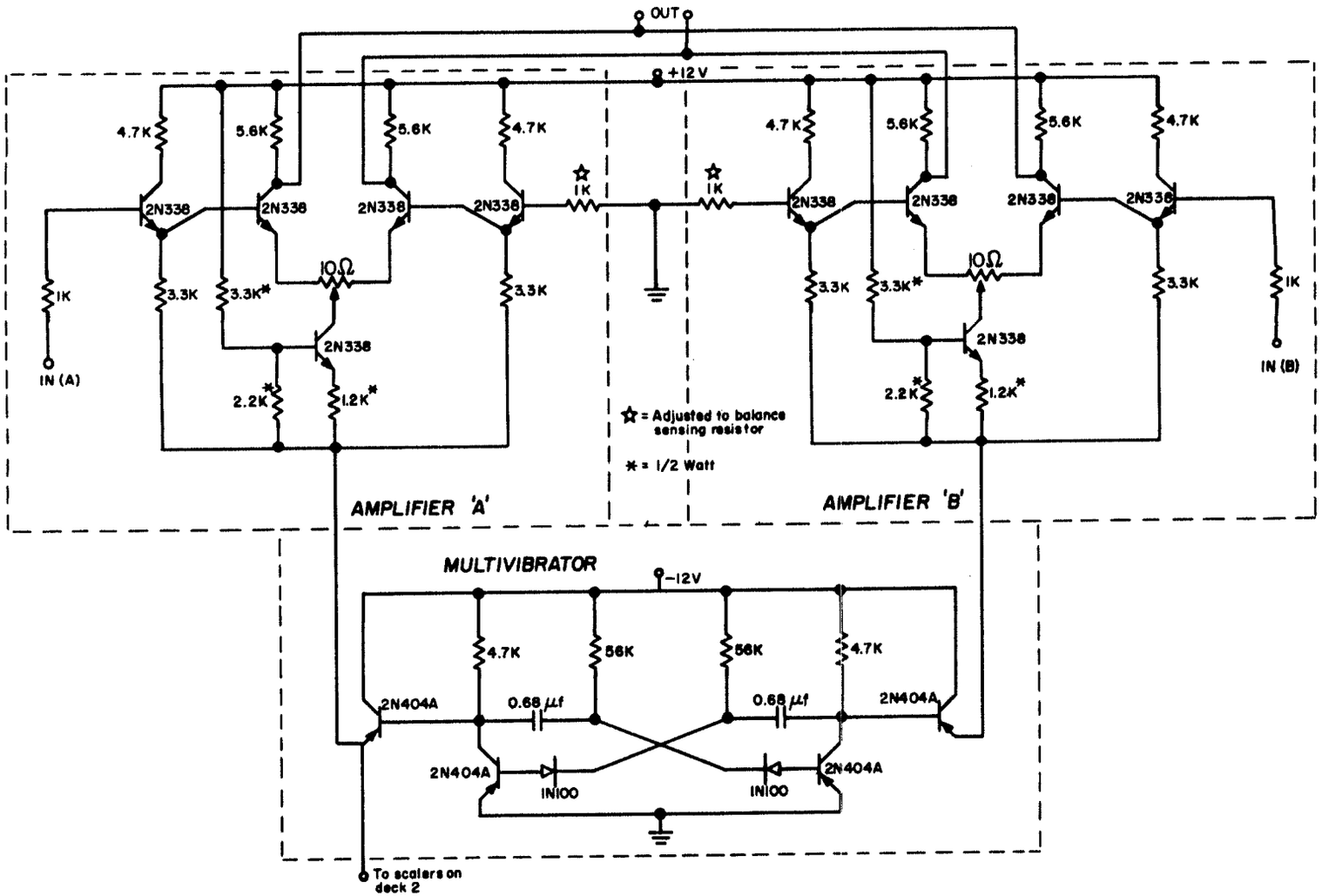

CIRCUIT DIAGRAM — DECK 1

Figure 13

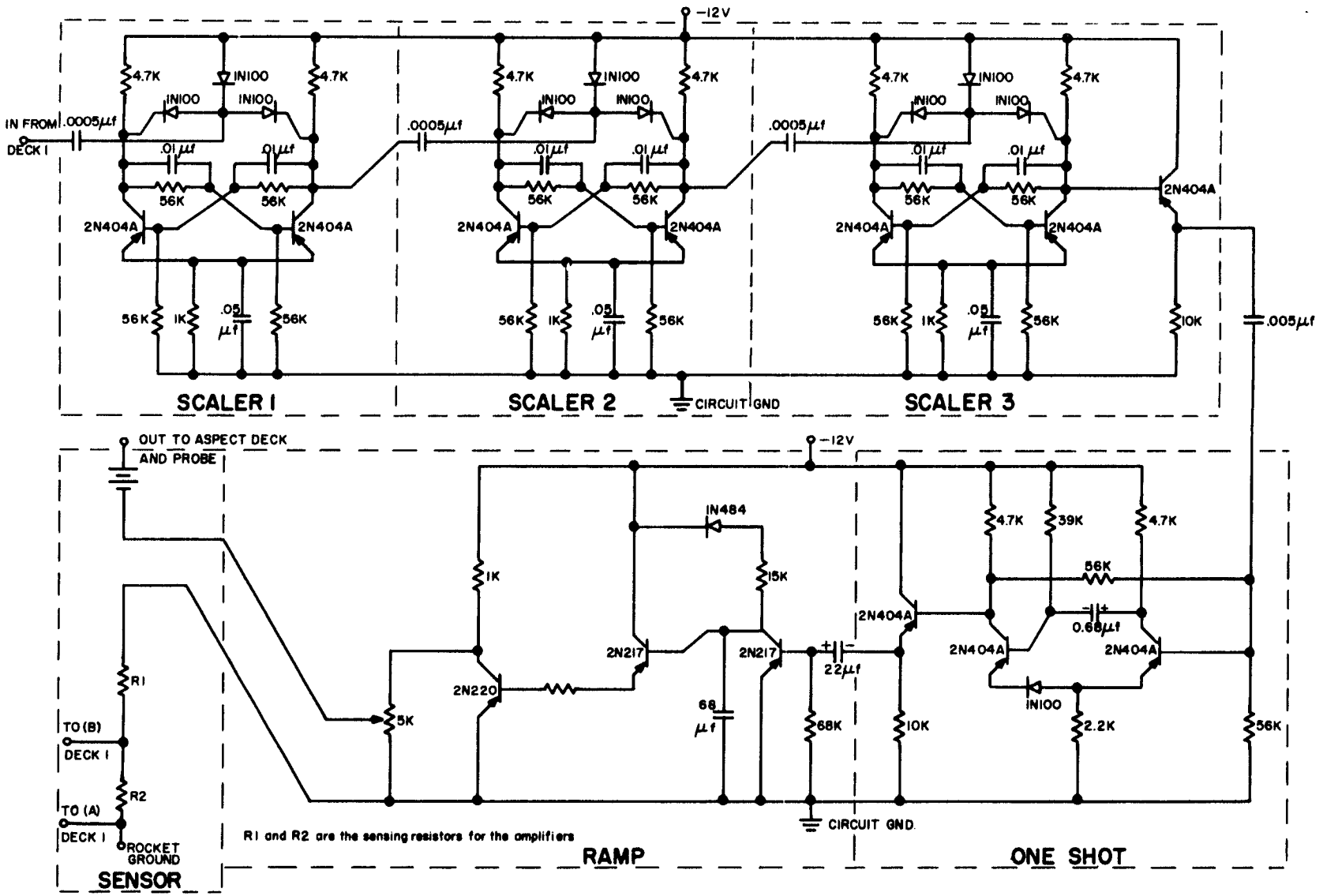

CIRCUIT DIAGRAM—DECK 2

Figure 14

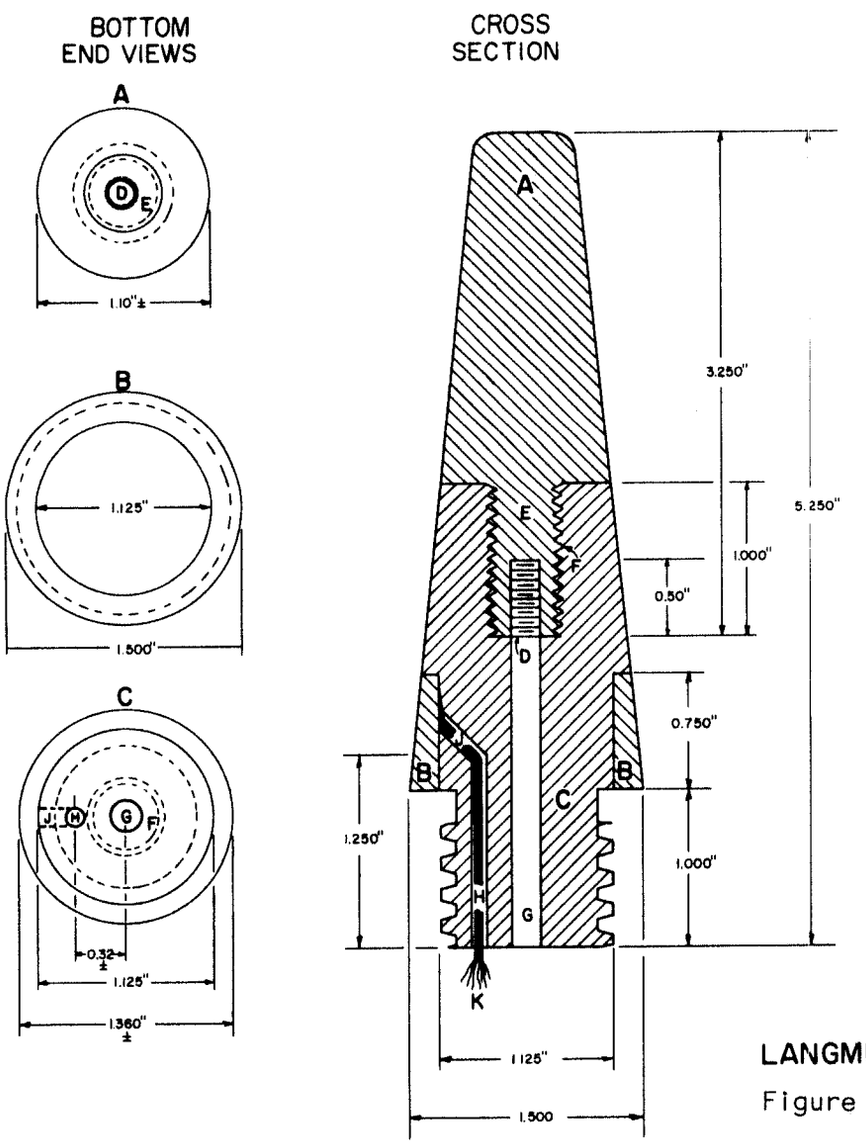

MATERIALS:

Nr. 347 stainless steel (ss) & teflon.

KEY:

A. SS nose, taper 2.50" per foot.
B. SS ferrule, taper 2.50" per foot.
C. Teflon base, taper 2.50" per foot.
D. Hole in SS nose, tapped 10-32, 0.50" deep.
E. SS nose threaded 1/2"-13, 1.00" long.
F. Hole in teflon base tapped 1/2"-13, 1.00" deep.
G. Hole in teflon base, nr. 11 drill.
H. Hole in teflon base, nr. 38 drill, 1.25" deep.
J. Hole in teflon base, nr. 38 drill at 45° to meet hole "H".
K. Nr. 16 stranded copper wire thru hole "H-J", stripped 1/2" at top, and squeezed between ferrule "B" and base "C" for electrical contact.

Bottom of base "C" threaded ACME Nr. 1.

LANGMUIR PROBE ASSEMBLY

Figure 15

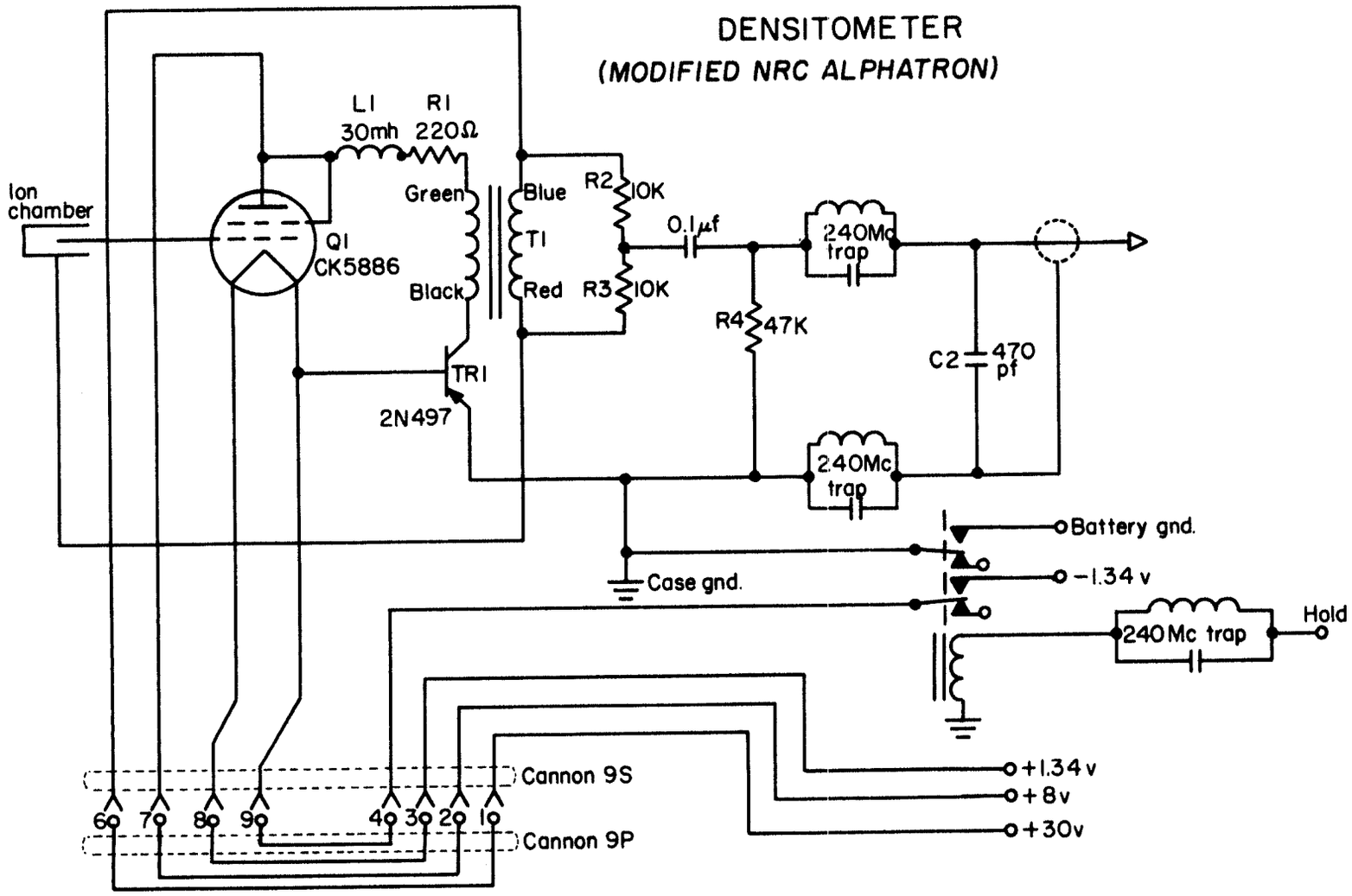
DENSITOMETER
(MODIFIED NRC ALPHATRON)
Ion chamber
L1 30mh
R1 220Ω
Q1 CK5886
Green
Black
Blue
T1
Red
R2 10K
R3 10K
0.1μf
240Mc trap
R4 47K
C2 470 pf
TR1
2N497
240Mc trap
Battery gnd.
-1.34 v
Case gnd.
240Mc trap
Hold
Cannon 9S
Cannon 9P
6 7 8 9 4 3 2 1
+1.34 v
+8v
+30v

Figure 16

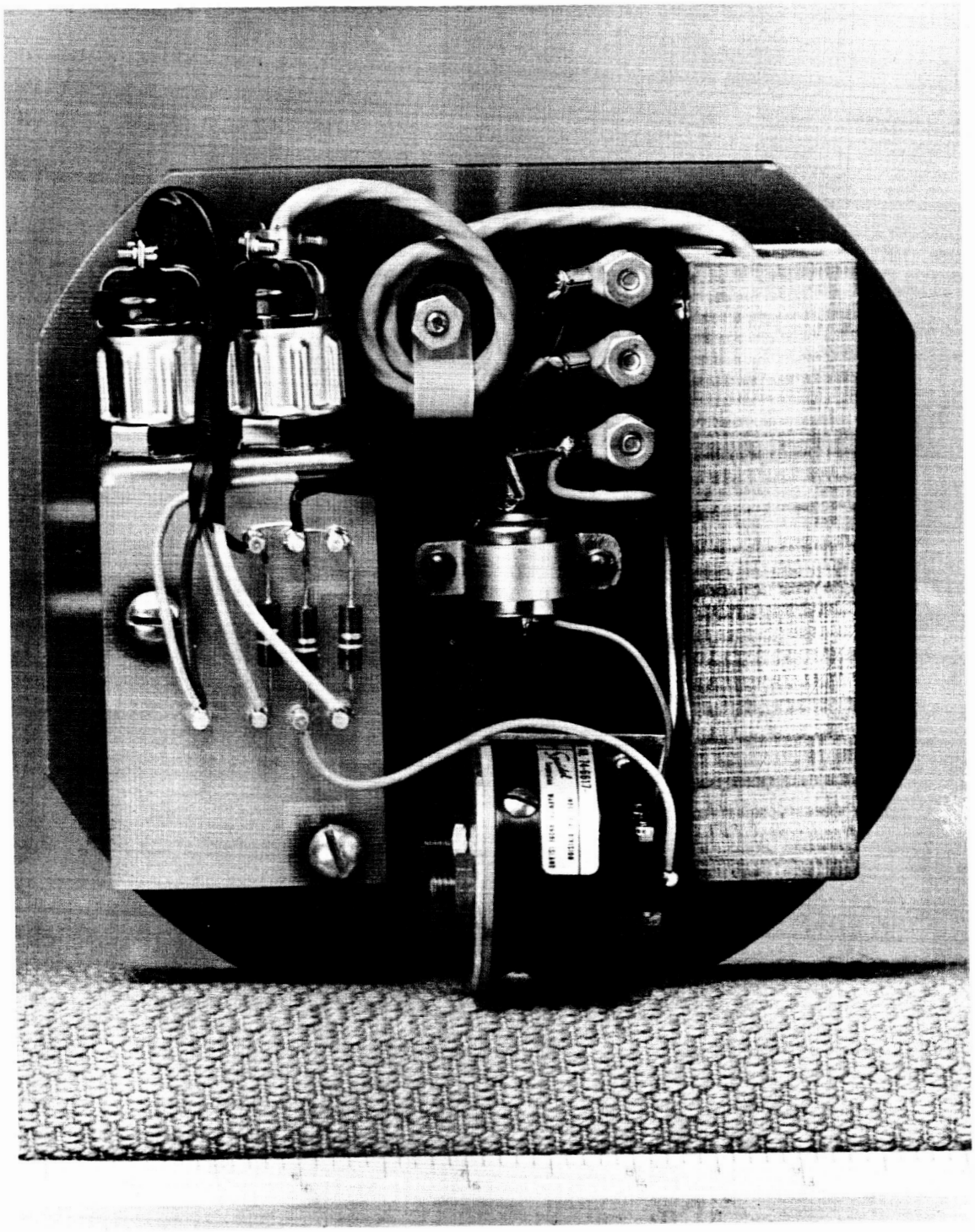

Figure 17

MIXER PLUG-IN SCHEMATIC

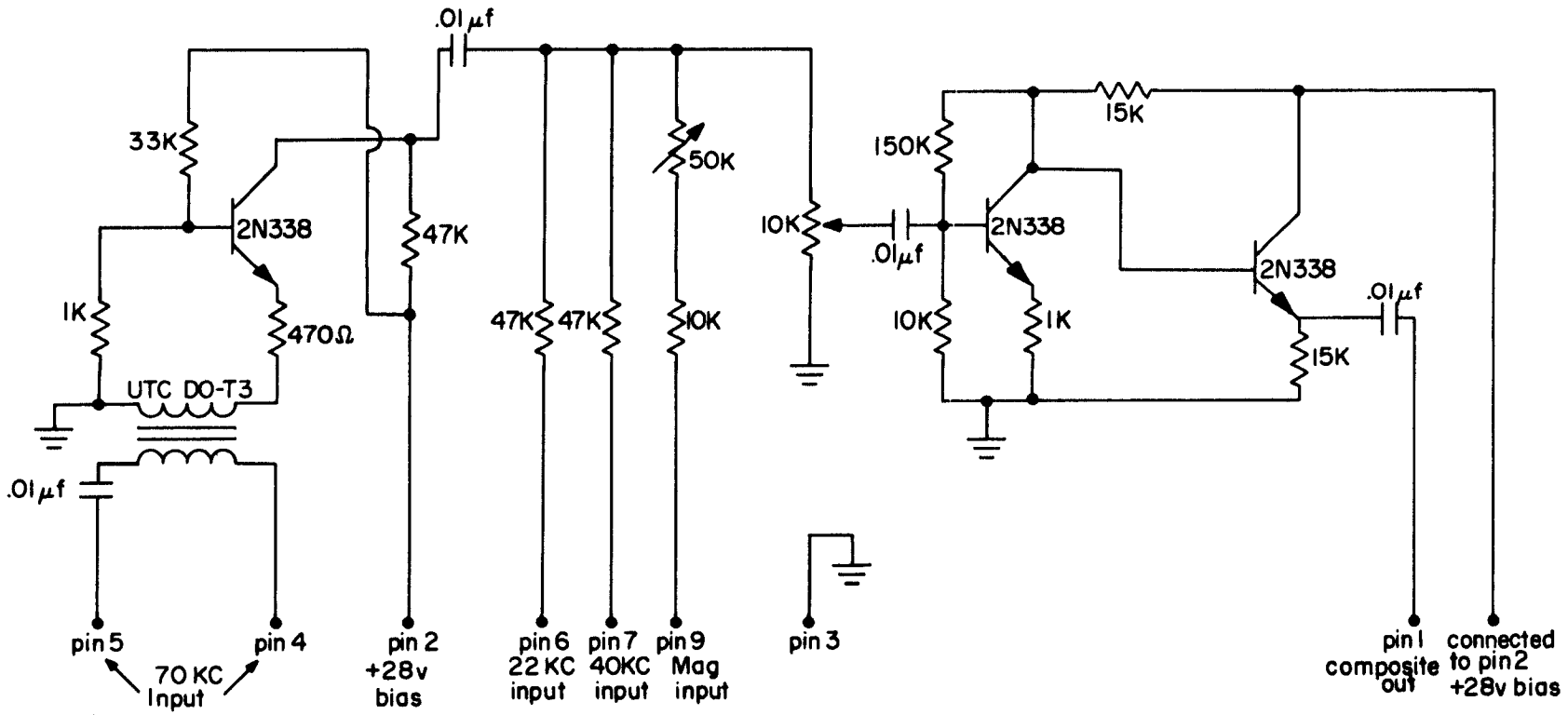

PLUG IS CANNON DEM 9 PNMB

Figure 18

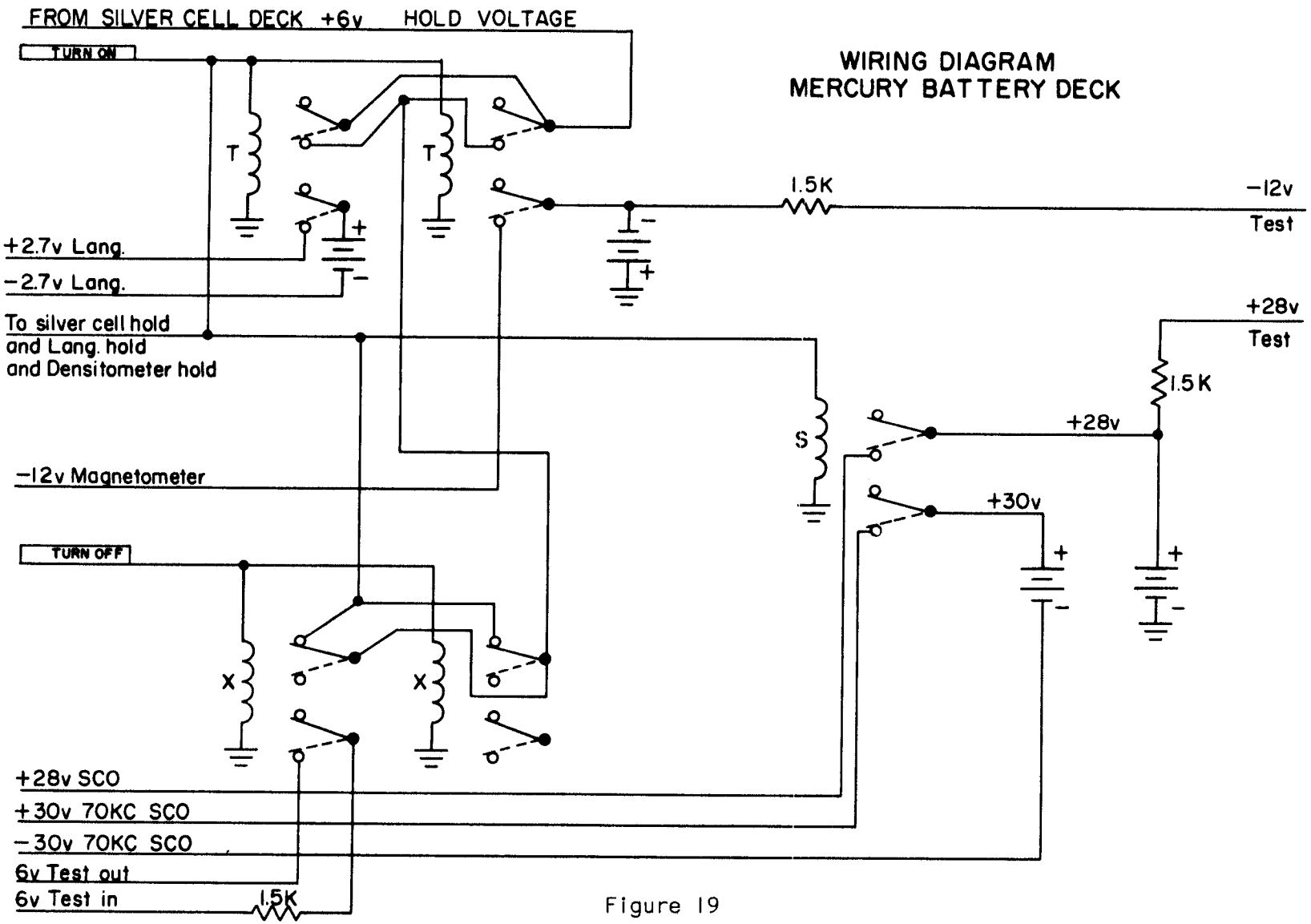

WIRING DIAGRAM
MERCURY BATTERY DECK

Figure 19

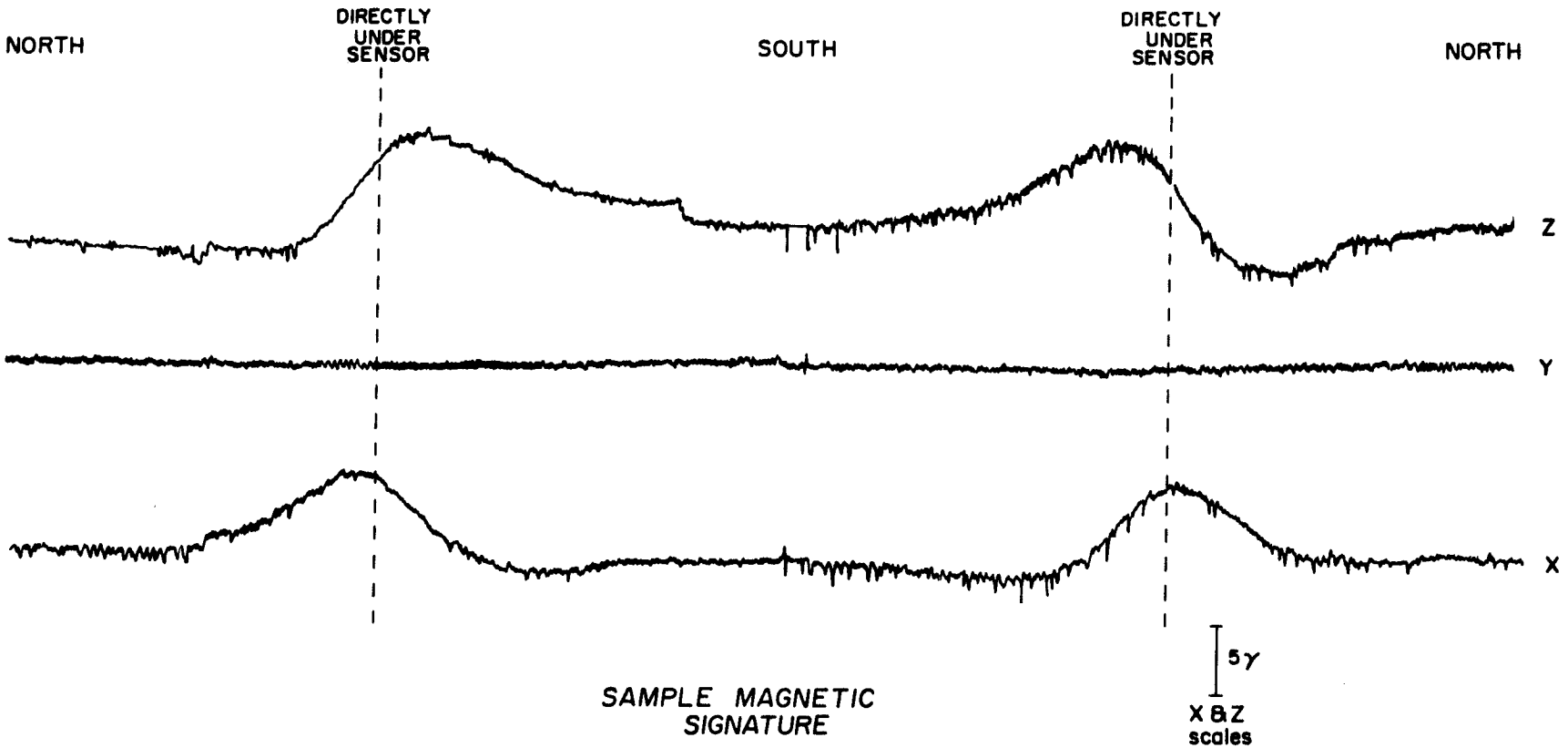

SAMPLE MAGNETIC SIGNATURE

Figure 20

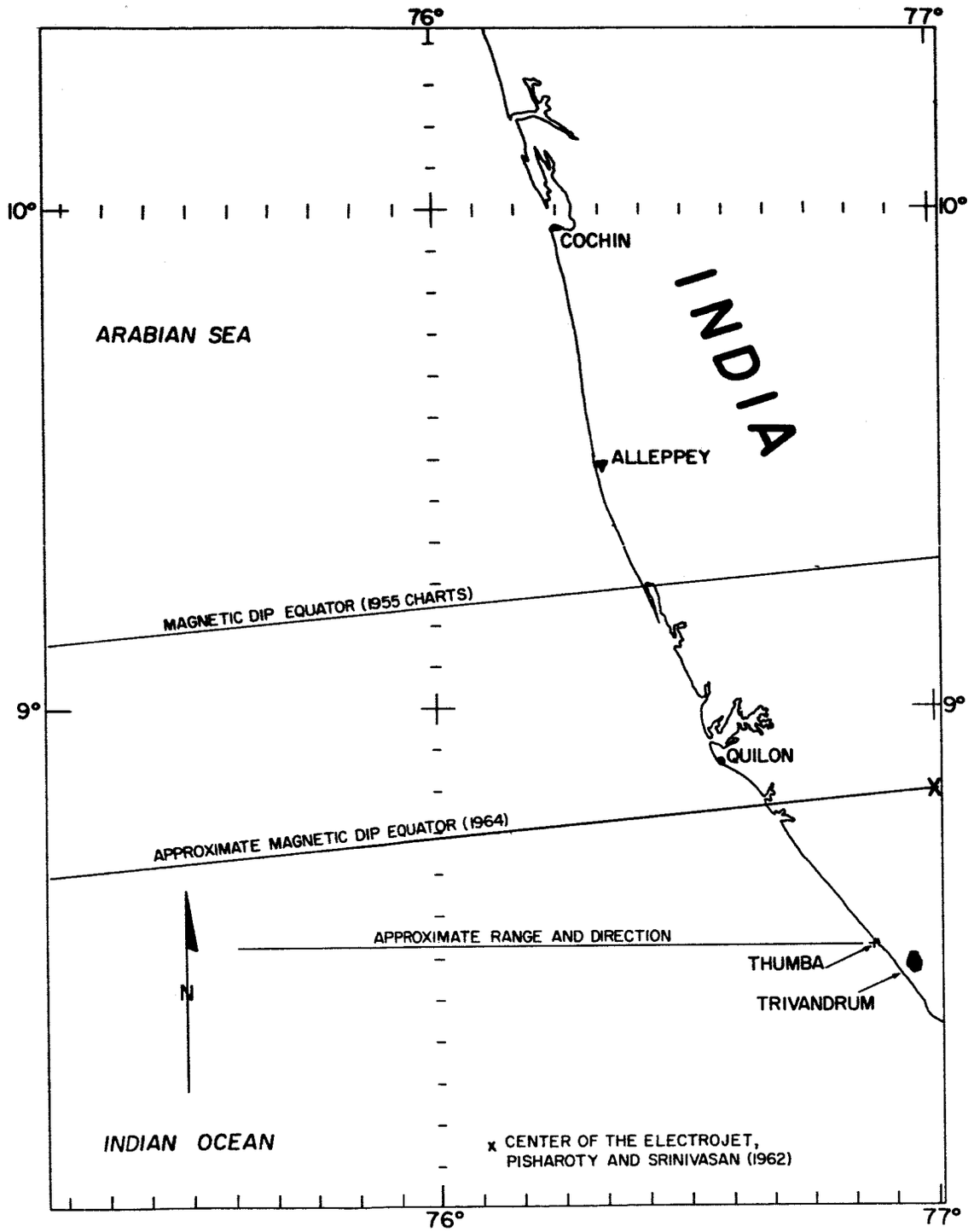
76°
77°
10°
10°
COCHIN
INDIA
ARABIAN SEA
ALLEPPEY
MAGNETIC DIP EQUATOR (1955 CHARTS)
9°
9°
QUILON
APPROXIMATE MAGNETIC DIP EQUATOR (1964)
APPROXIMATE RANGE AND DIRECTION
THUMBA
TRIVANDRUM
N
INDIAN OCEAN
x CENTER OF THE ELECTROJET,
PISHAROTY AND SRINIVASAN (1962)
76°
77°

Figure 21

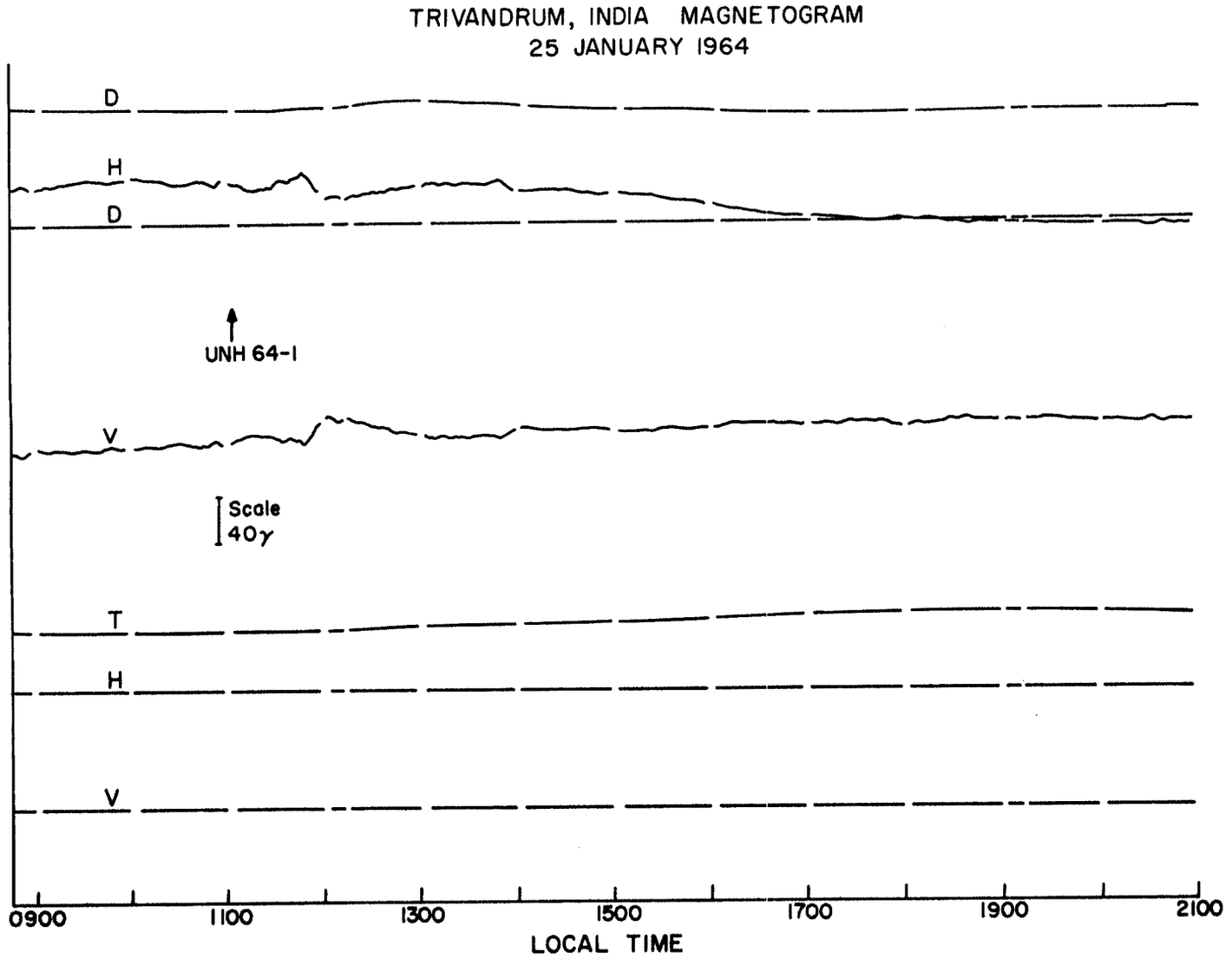
TRIVANDRUM, INDIA MAGNETOGRAM
25 JANUARY 1964
D
H
D
UNH 64-1
V
Scale
40γ
T
H
V
0900
1100
1300
1500
1700
1900
2100
LOCAL TIME

Figure 22

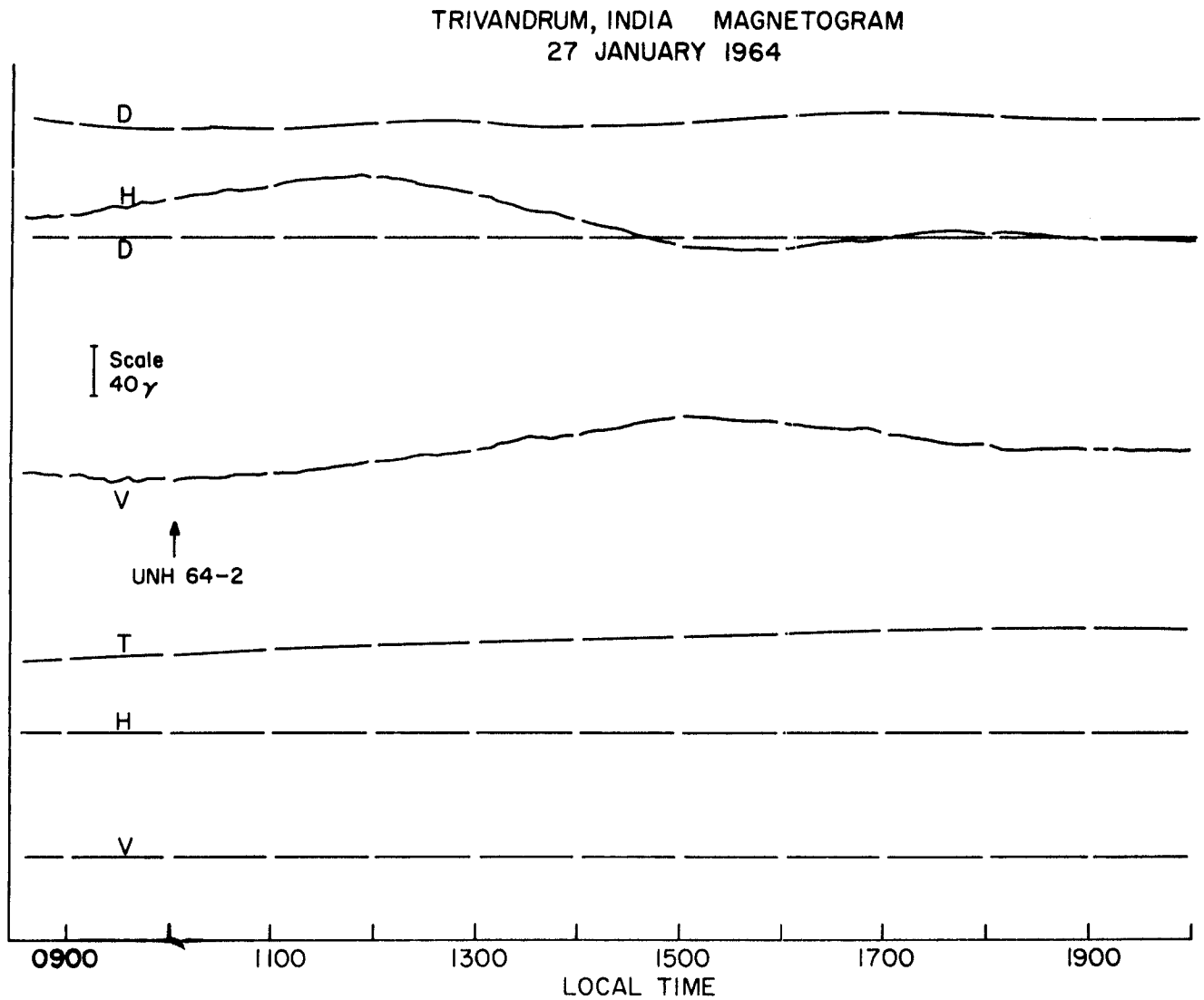
TRIVANDRUM, INDIA MAGNETOGRAM
27 JANUARY 1964
D
H
D
Scale
40γ
V
UNH 64-2
T
H
V
0900
1100
1300
1500
1700
1900
LOCAL TIME

Figure 23

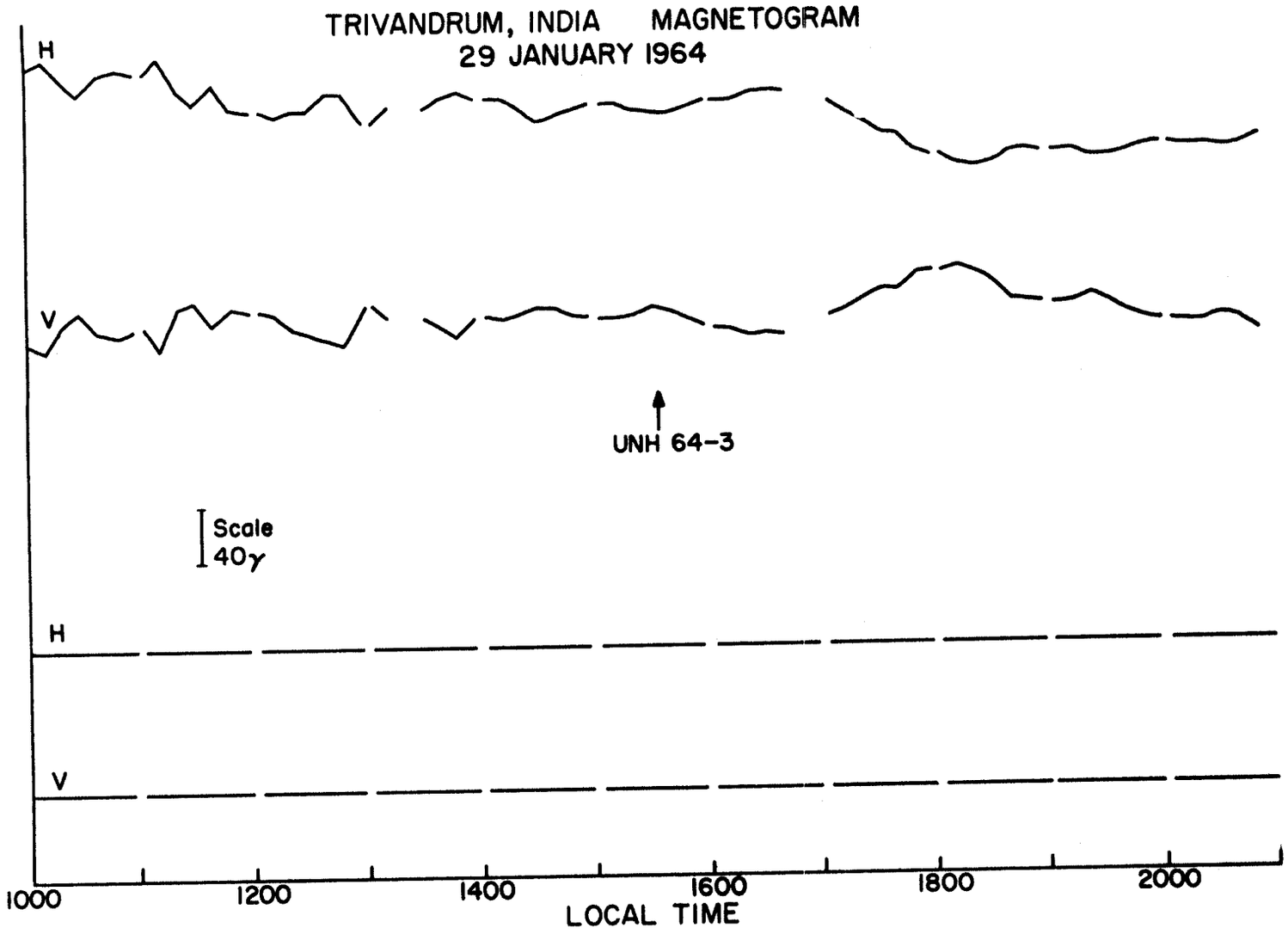
TRIVANDRUM, INDIA MAGNETOGRAM
29 JANUARY 1964
H
V
UNH 64-3
Scale
40γ
H
V
1000
1200
1400
1600
1800
2000
LOCAL TIME

Figure 24

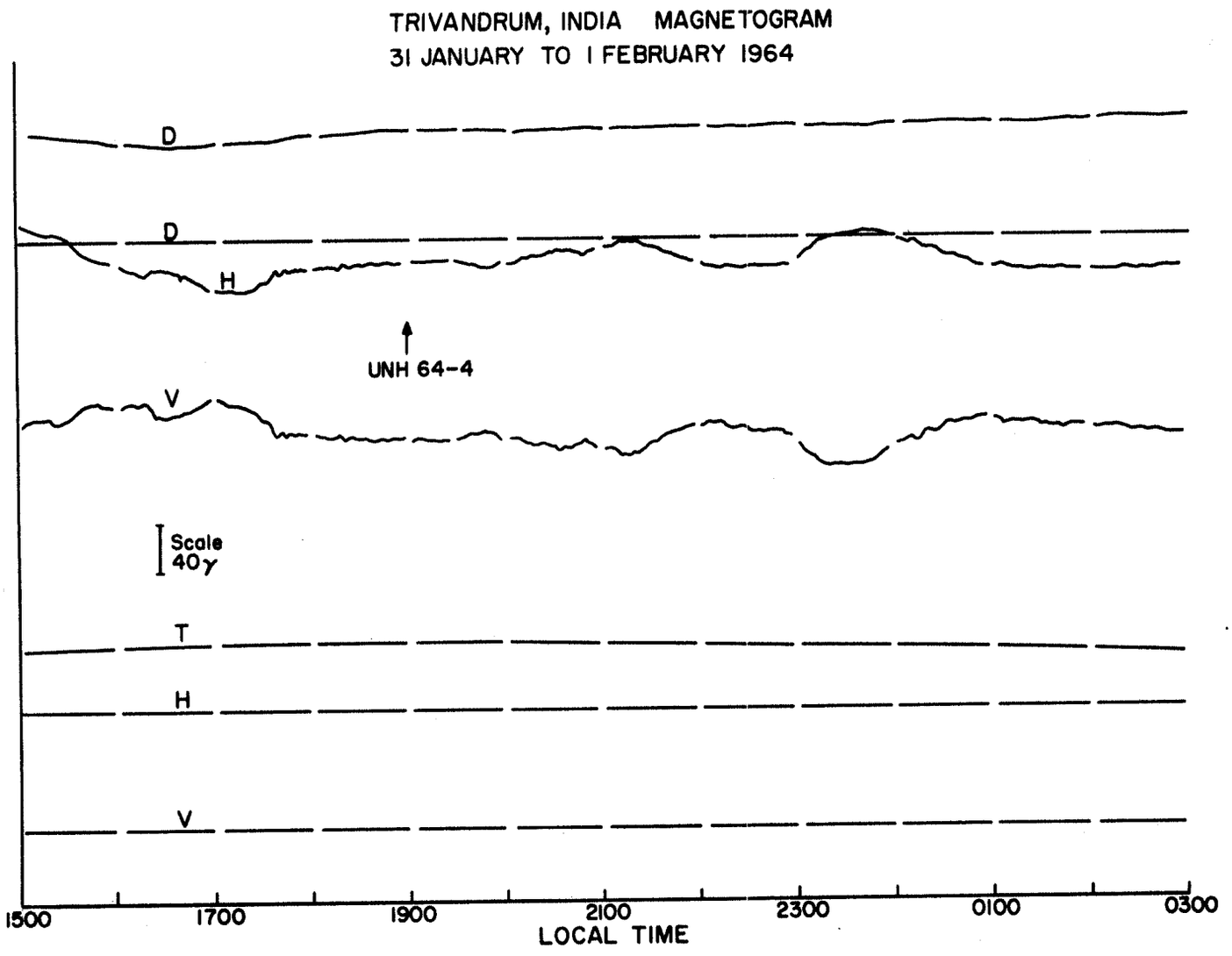
TRIVANDRUM, INDIA MAGNETOGRAM
31 JANUARY TO 1 FEBRUARY 1964
D
D
H
UNH 64-4
V
Scale
40γ
T
H
V
1500
1700
1900
2100
2300
0100
0300
LOCAL TIME

Figure 25

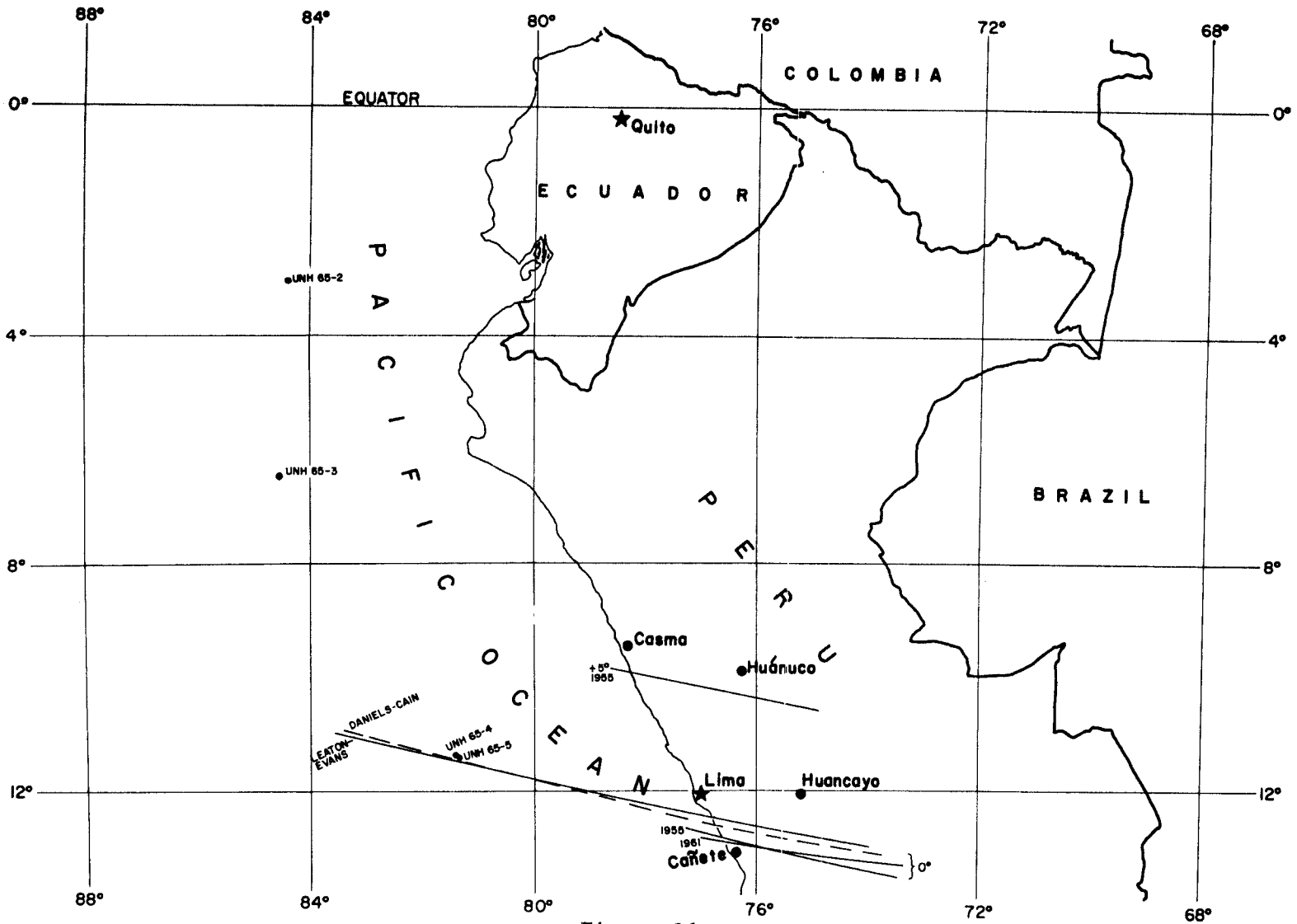
88°
84°
80°
76°
72°
68°
0°
4°
8°
12°
EQUATOR
COLOMBIA
Quito
ECUADOR
PACIFIC OCEAN
PERU
BRAZIL
UNH 65-2
UNH 65-3
UNH 65-4
UNH 65-5
DANIELS-CAIN
EATON-EVANS
Casma
Huánuco
+5°
1965
Lima
Huancayo
1955
1961
Cañete
0°

Figure 26

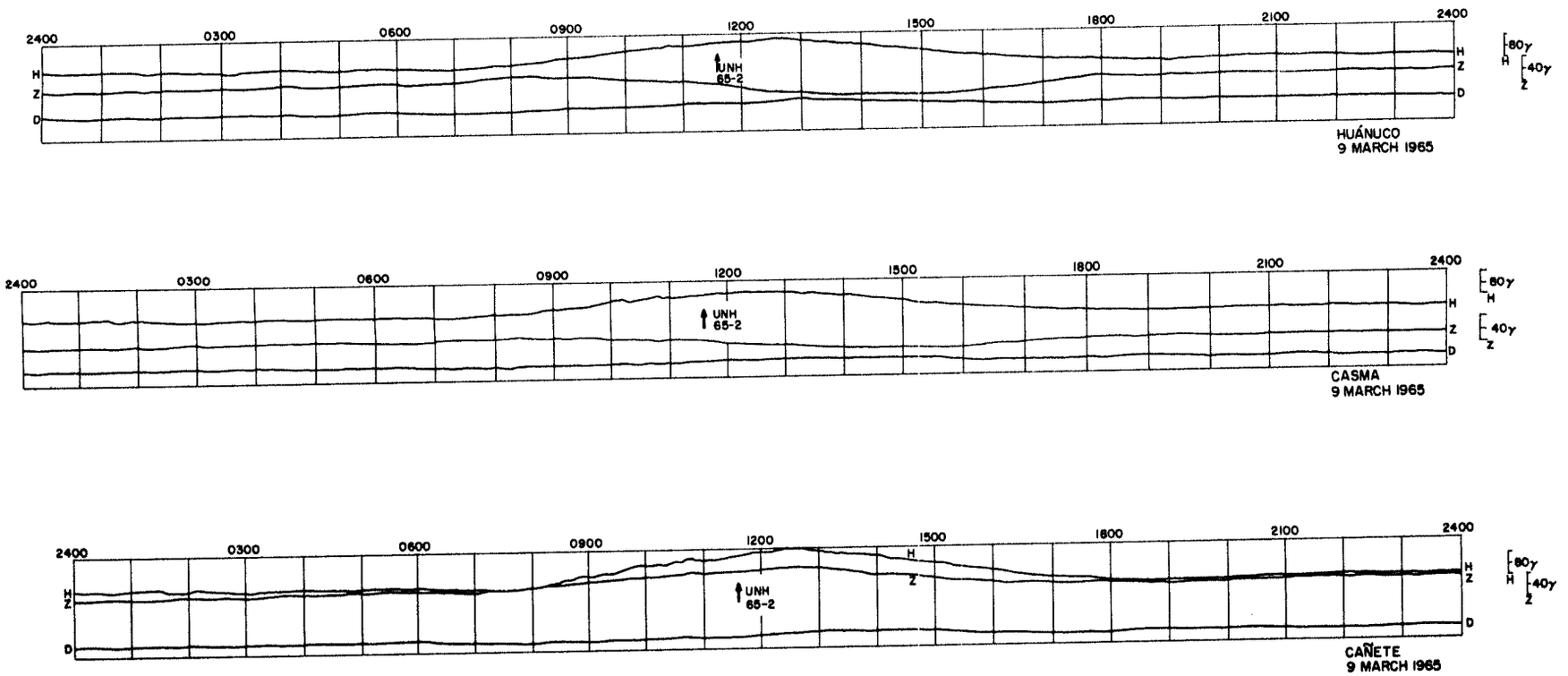
2400
0300
0600
0900
1200
1500
1800
2100
2400
H
Z
D
UNH
65-2
80γ
H
40γ
Z
HUÁNUCO
9 MARCH 1965
CASMA
9 MARCH 1965
CAÑETE
9 MARCH 1965

Figure 27

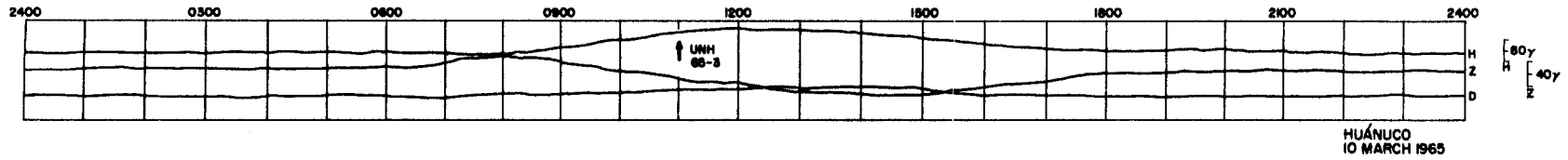
2400
0300
0600
0900
1200
1500
1800
2100
2400
UNH
65-3
H
Z
D
60γ
H
40γ
Z
HUÁNUCO
10 MARCH 1965

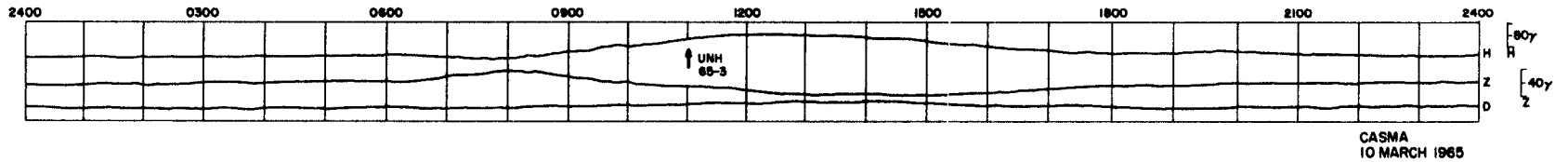
2400
0300
0600
0900
1200
1500
1800
2100
2400
UNH
65-3
H
Z
D
60γ
H
40γ
Z
CASMA
10 MARCH 1965

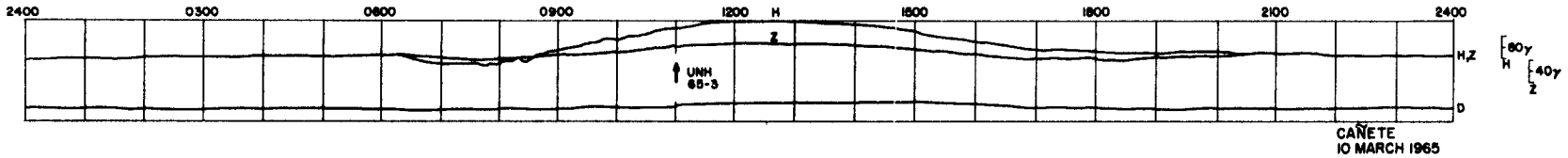
2400
0300
0600
0900
1200
H
Z
1500
1800
2100
2400
UNH
65-3
H,Z
D
60γ
H
40γ
Z
CAÑETE
10 MARCH 1965

Figure 28

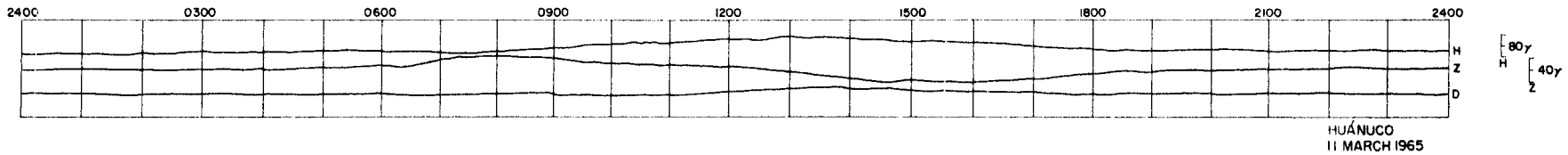

HUÁNUCO
11 MARCH 1965

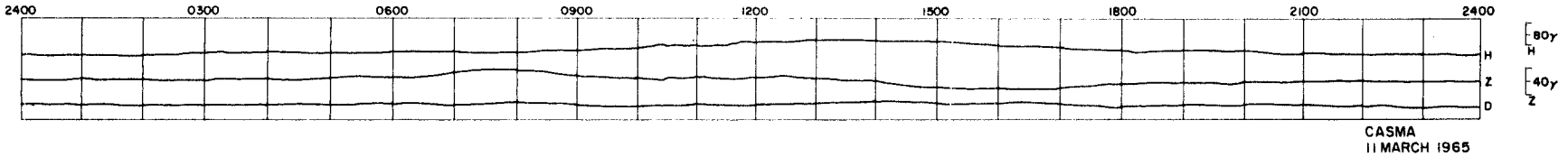

CASMA
11 MARCH 1965

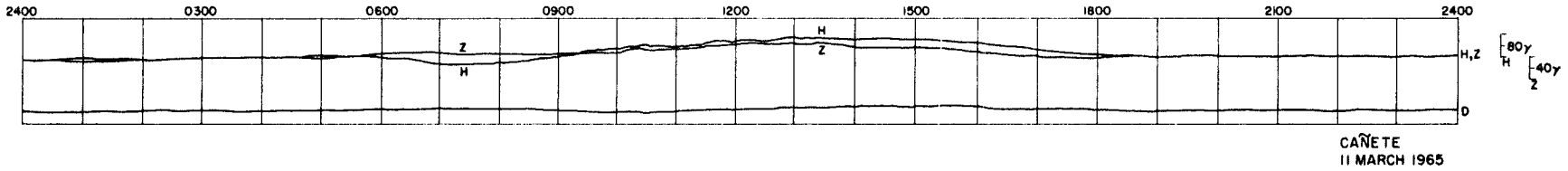

CAÑETE
11 MARCH 1965

Figure 29

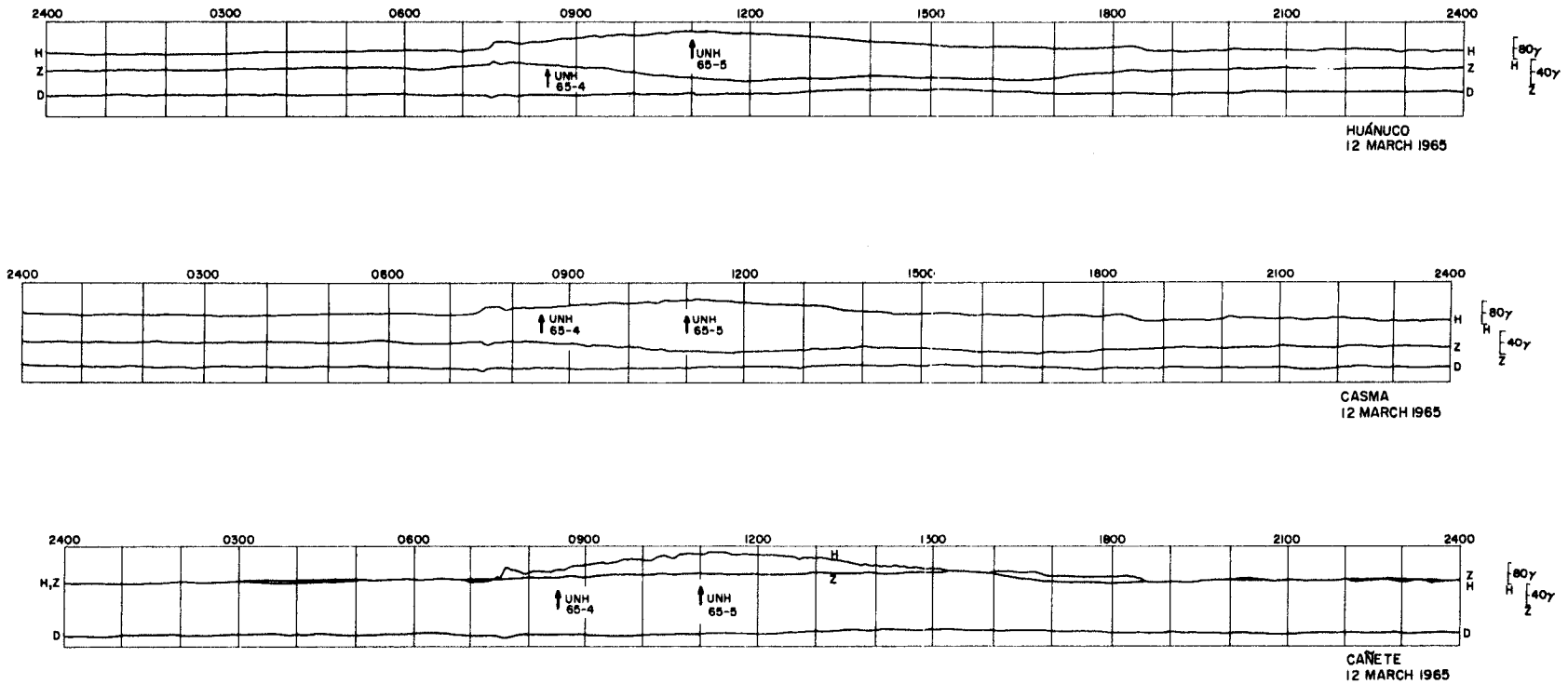
2400
0300
0600
0900
1200
1500
1800
2100
2400
H
Z
D
UNH 65-4
UNH 65-5
80γ
40γ
HUÁNUCO
12 MARCH 1965
CASMA
12 MARCH 1965
H,Z
CAÑETE
12 MARCH 1965

Figure 30

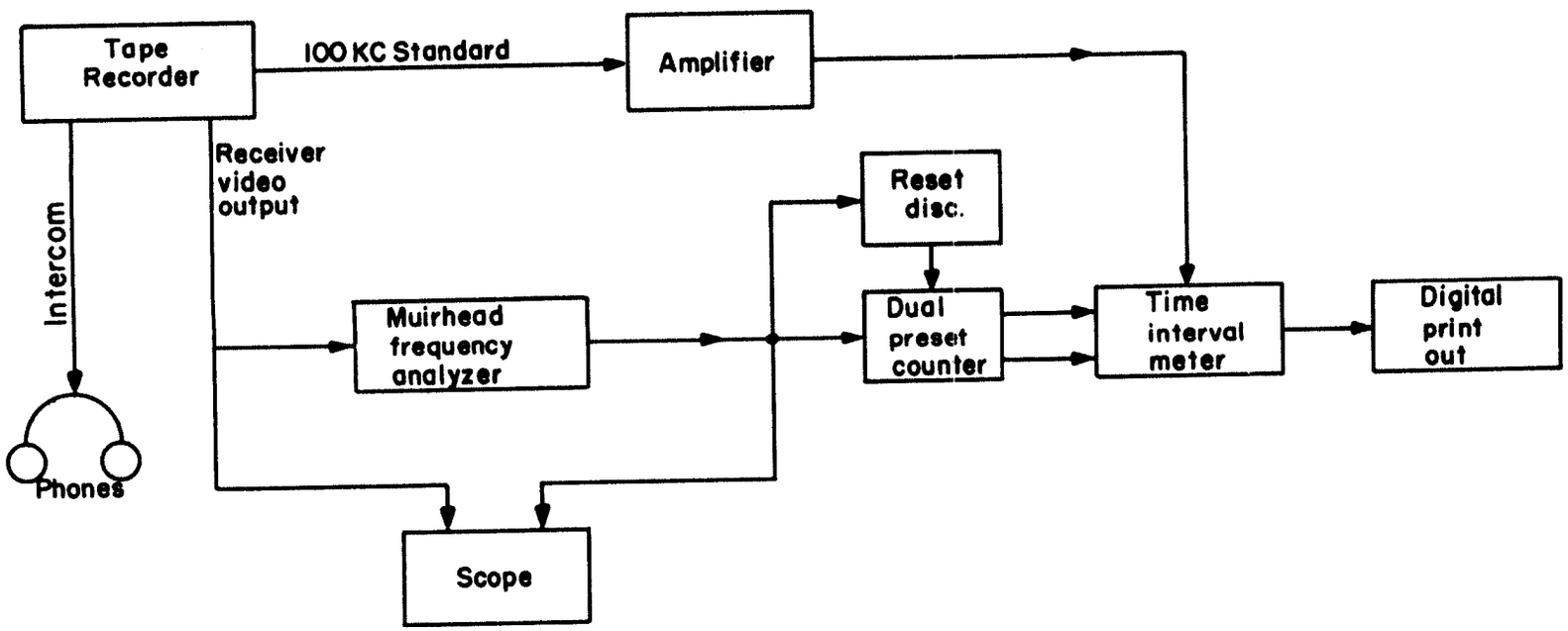

DATA READ OUT SET UP — MAGNETOMETER

Figure 31

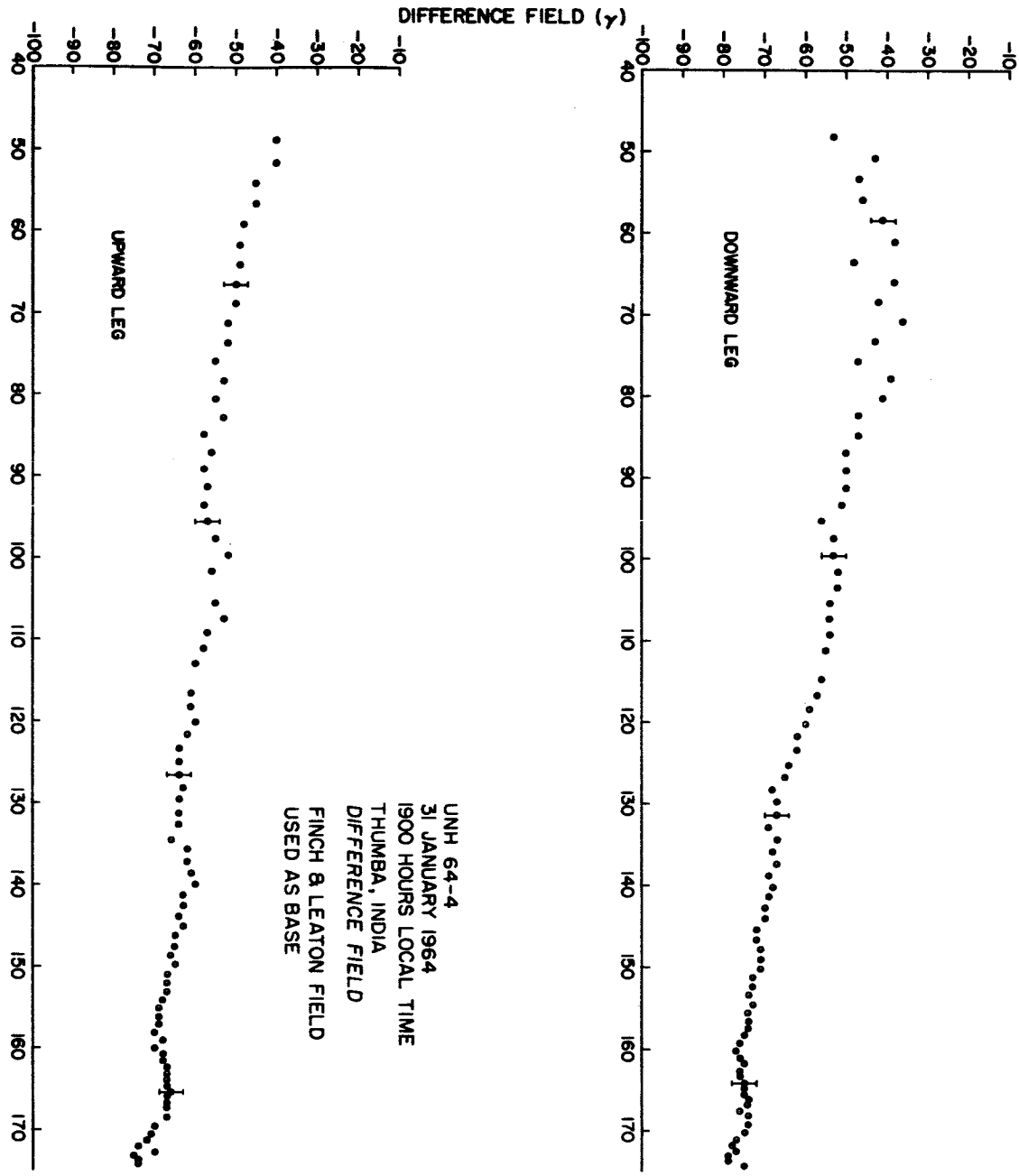
DIFFERENCE FIELD (γ)
-10
-20
-30
-40
-50
-60
-70
-80
-90
-100
40
50
60
70
80
90
100
110
120
130
140
150
160
170
UPWARD LEG
DOWNWARD LEG
UNH 64-4
31 JANUARY 1964
1900 HOURS LOCAL TIME
THUMBA, INDIA
DIFFERENCE FIELD
FINCH & LEATON FIELD
USED AS BASE

Figure 32

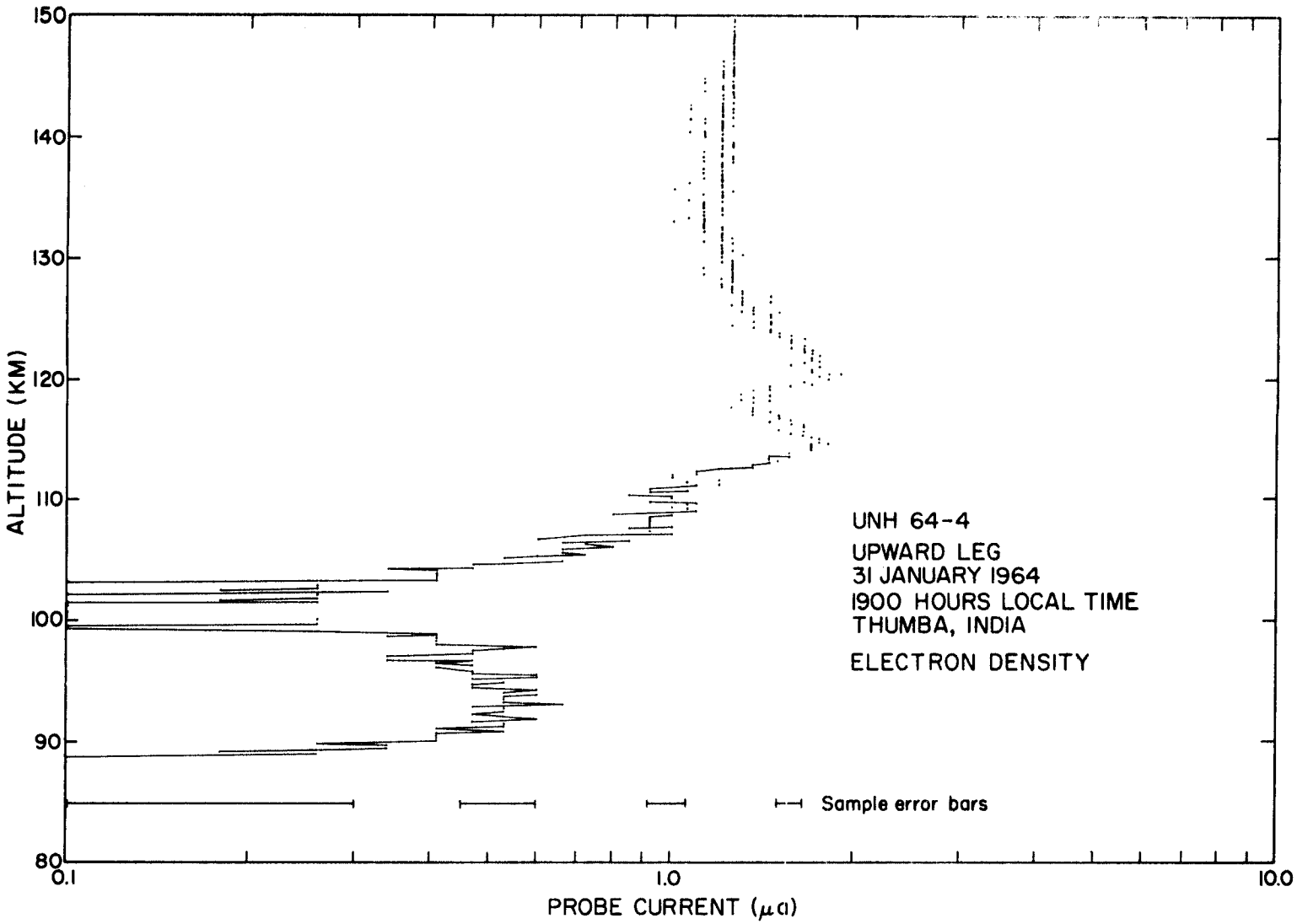
150
140
130
120
110
100
90
80
ALTITUDE (KM)
0.1
1.0
10.0
PROBE CURRENT (μa)
UNH 64-4
UPWARD LEG
31 JANUARY 1964
1900 HOURS LOCAL TIME
THUMBA, INDIA
ELECTRON DENSITY
Sample error bars

Figure 33

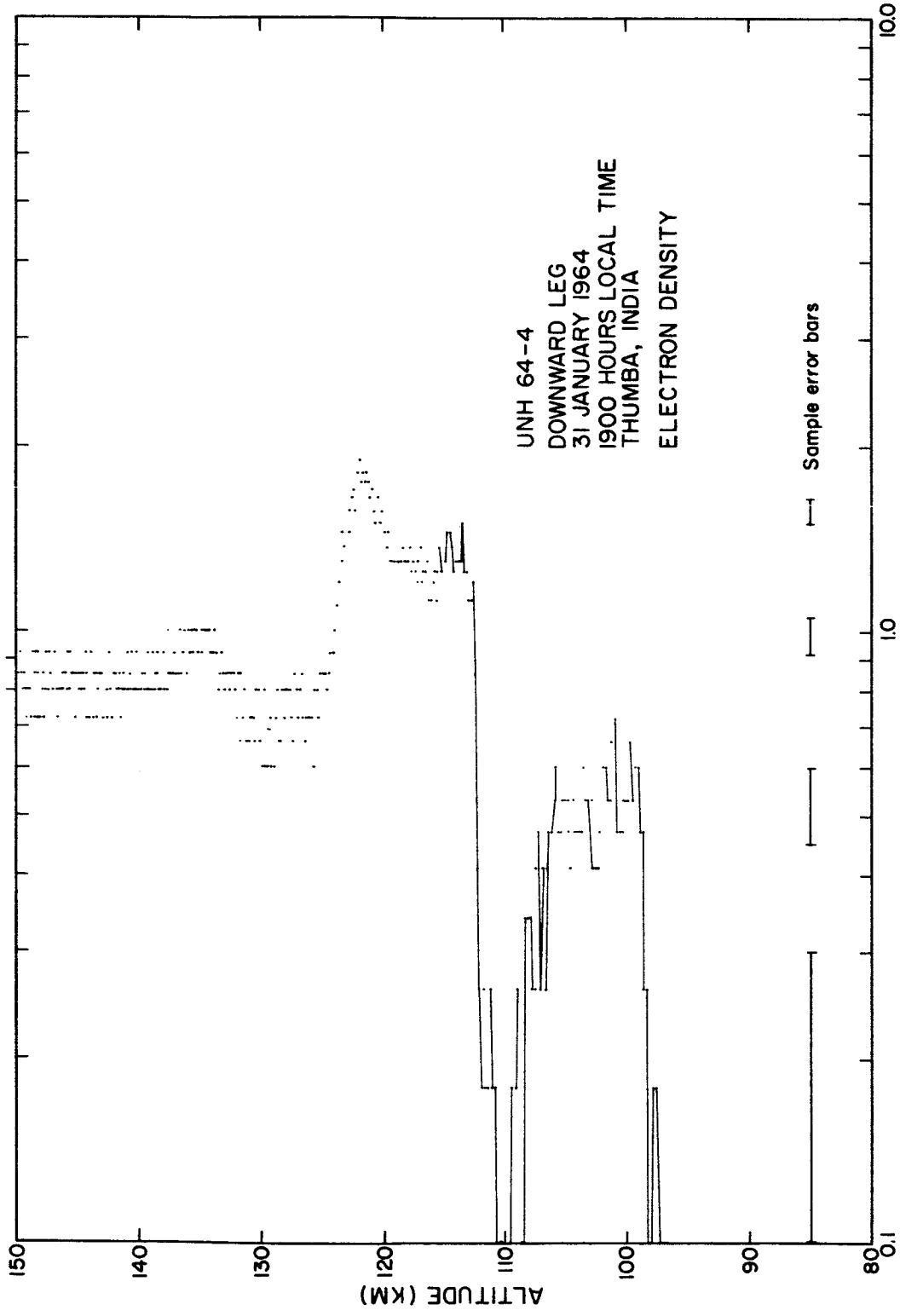
UNH 64-4
DOWNWARD LEG
31 JANUARY 1964
1900 HOURS LOCAL TIME
THUMBA, INDIA
ELECTRON DENSITY
Sample error bars
ALTITUDE (KM)
PROBE CURRENT (μa)
150
140
130
120
110
100
90
80
10.0
1.0
0.1

Figure 34

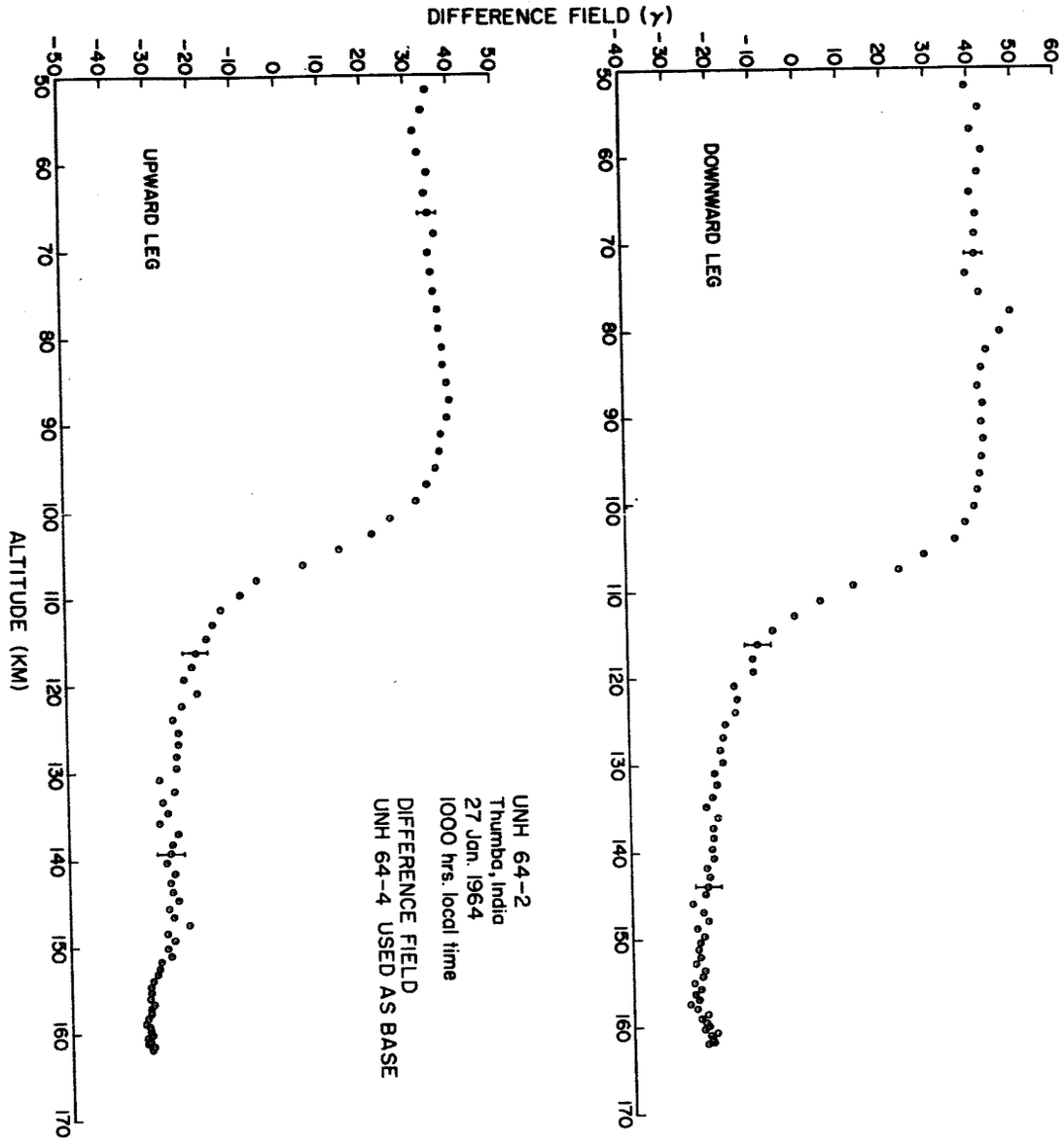
DIFFERENCE FIELD (γ)
DOWNWARD LEG
UPWARD LEG
ALTITUDE (KM)
UNH 64-2
Thumba, India
27 Jan. 1964
1000 hrs. local time
DIFFERENCE FIELD
UNH 64-4 USED AS BASE

Figure 35

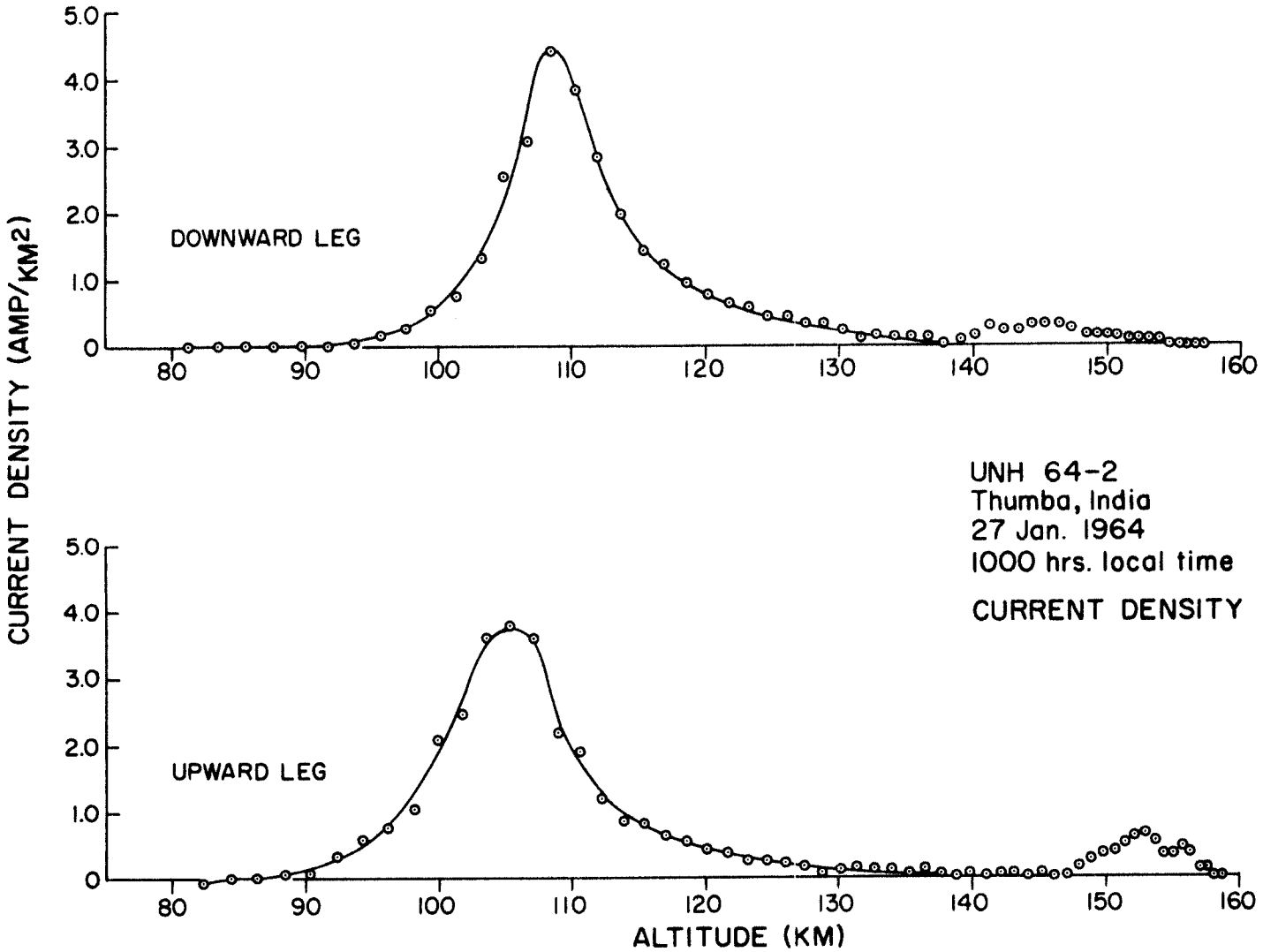
CURRENT DENSITY (AMP/KM²)
5.0
4.0
3.0
2.0
1.0
0
DOWNWARD LEG
80
90
100
110
120
130
140
150
160
UNH 64-2
Thumba, India
27 Jan. 1964
1000 hrs. local time
CURRENT DENSITY
UPWARD LEG
ALTITUDE (KM)

Figure 36

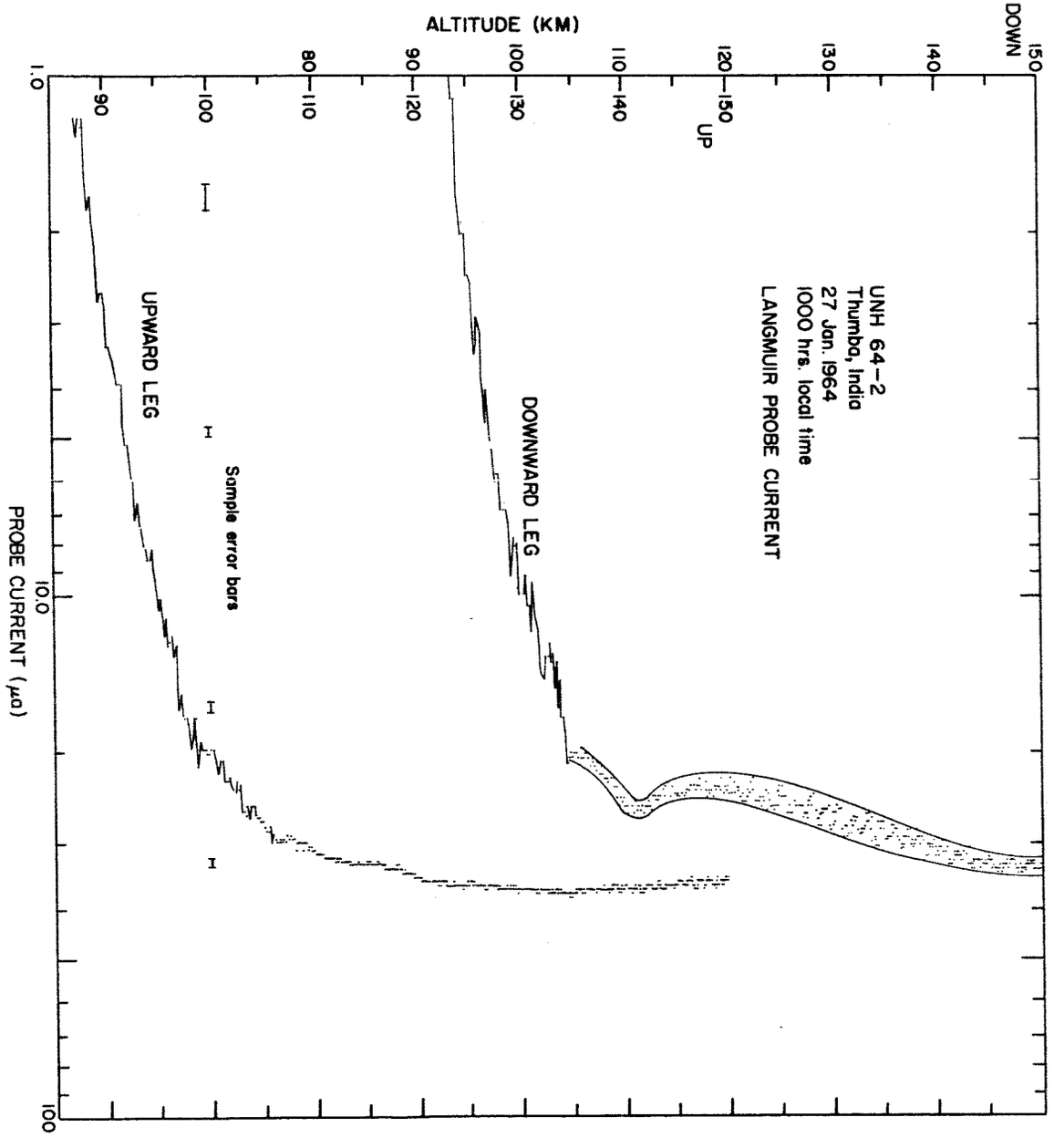
ALTITUDE (KM)
DOWN
UP
UNH 64-2
Thumba, India
27 Jan. 1964
1000 hrs. local time
LANGMUIR PROBE CURRENT
UPWARD LEG
DOWNWARD LEG
Sample error bars
PROBE CURRENT (μa)

Figure 37

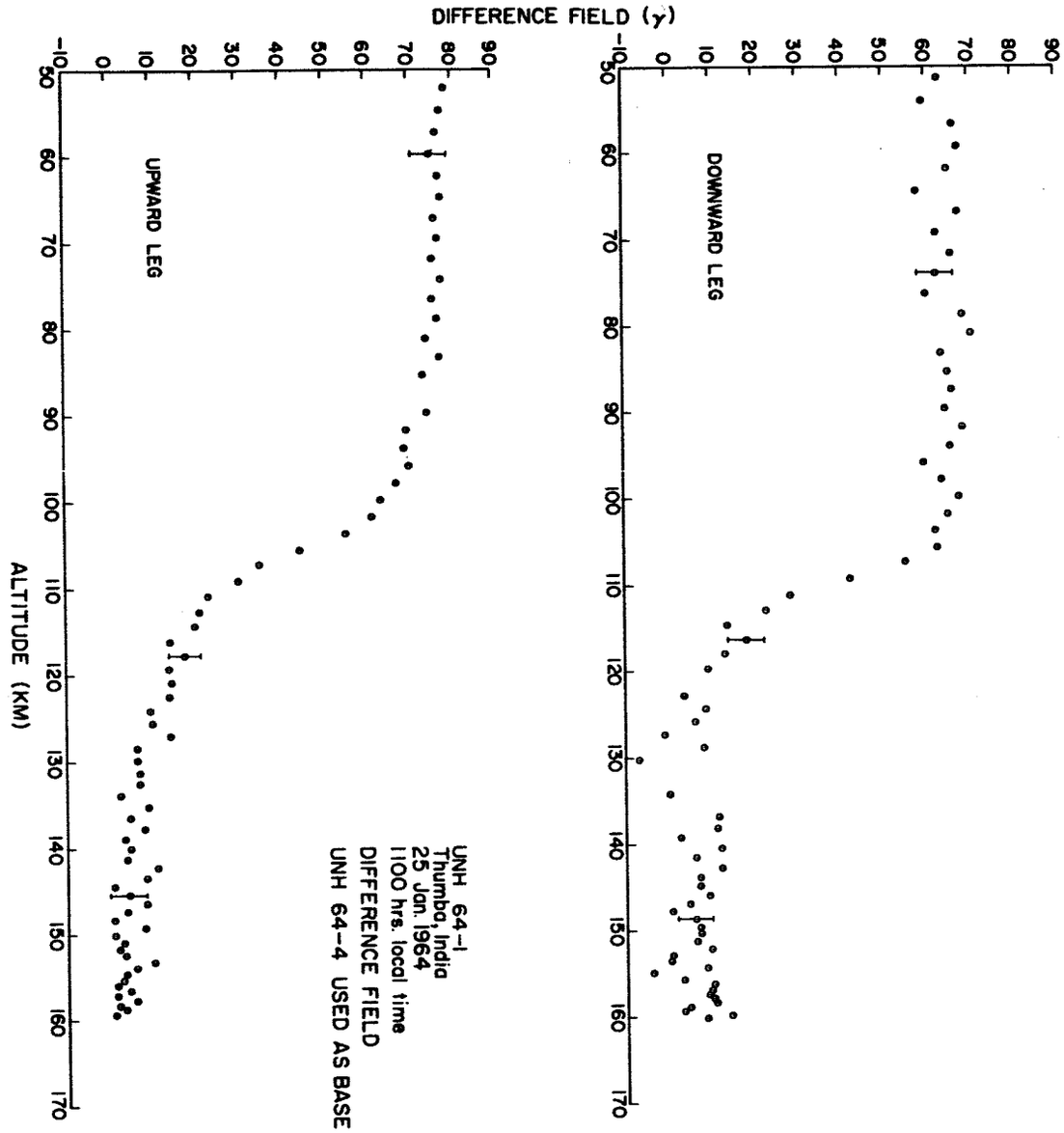
DIFFERENCE FIELD (γ)
DOWNWARD LEG
UPWARD LEG
ALTITUDE (KM)
UNH 64-1
Thumba, India
25 Jan. 1964
1100 hrs. local time
DIFFERENCE FIELD
UNH 64-4 USED AS BASE

Figure 38

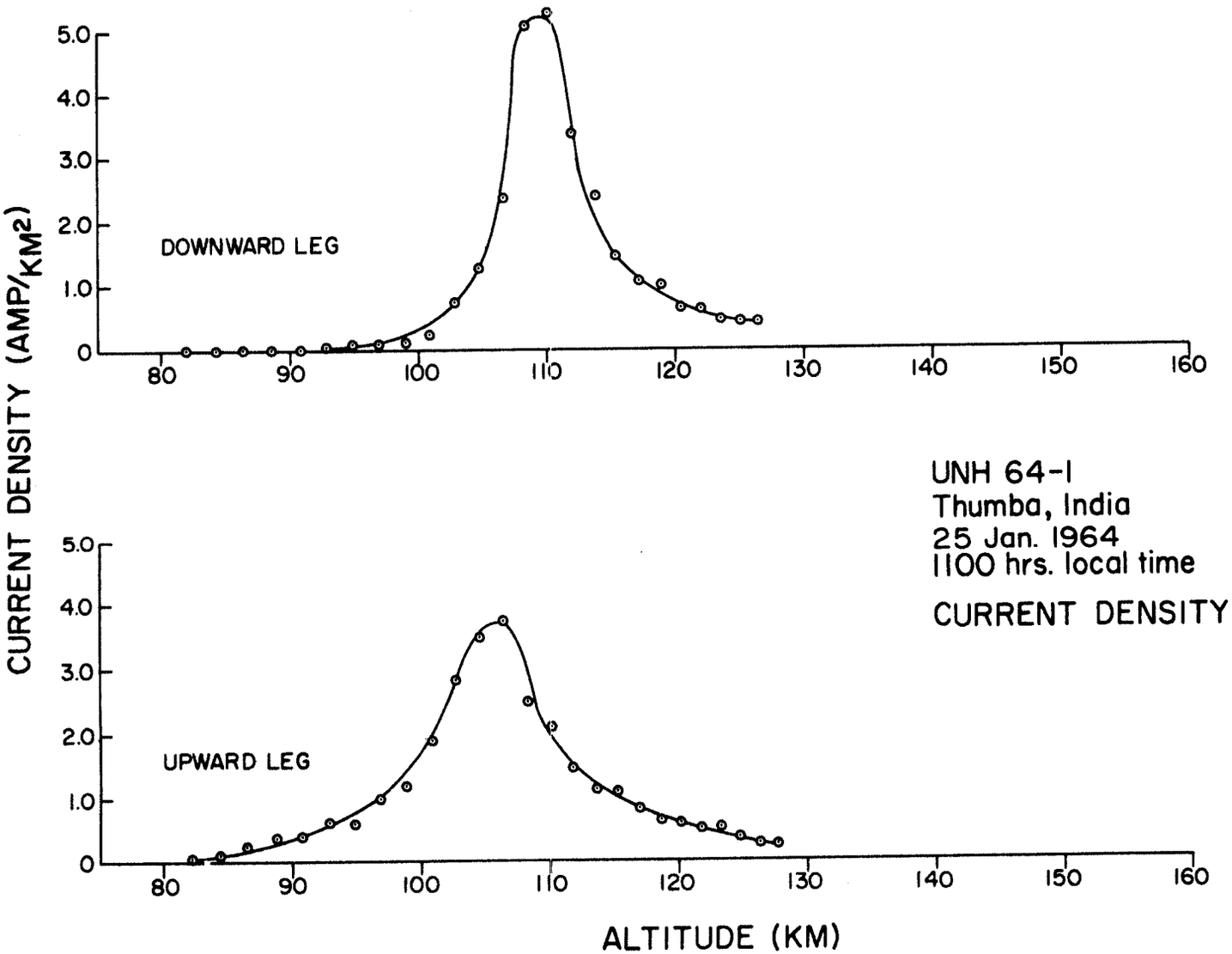

UNH 64-I
Thumba, India
25 Jan. 1964
1100 hrs. local time

CURRENT DENSITY

Figure 39

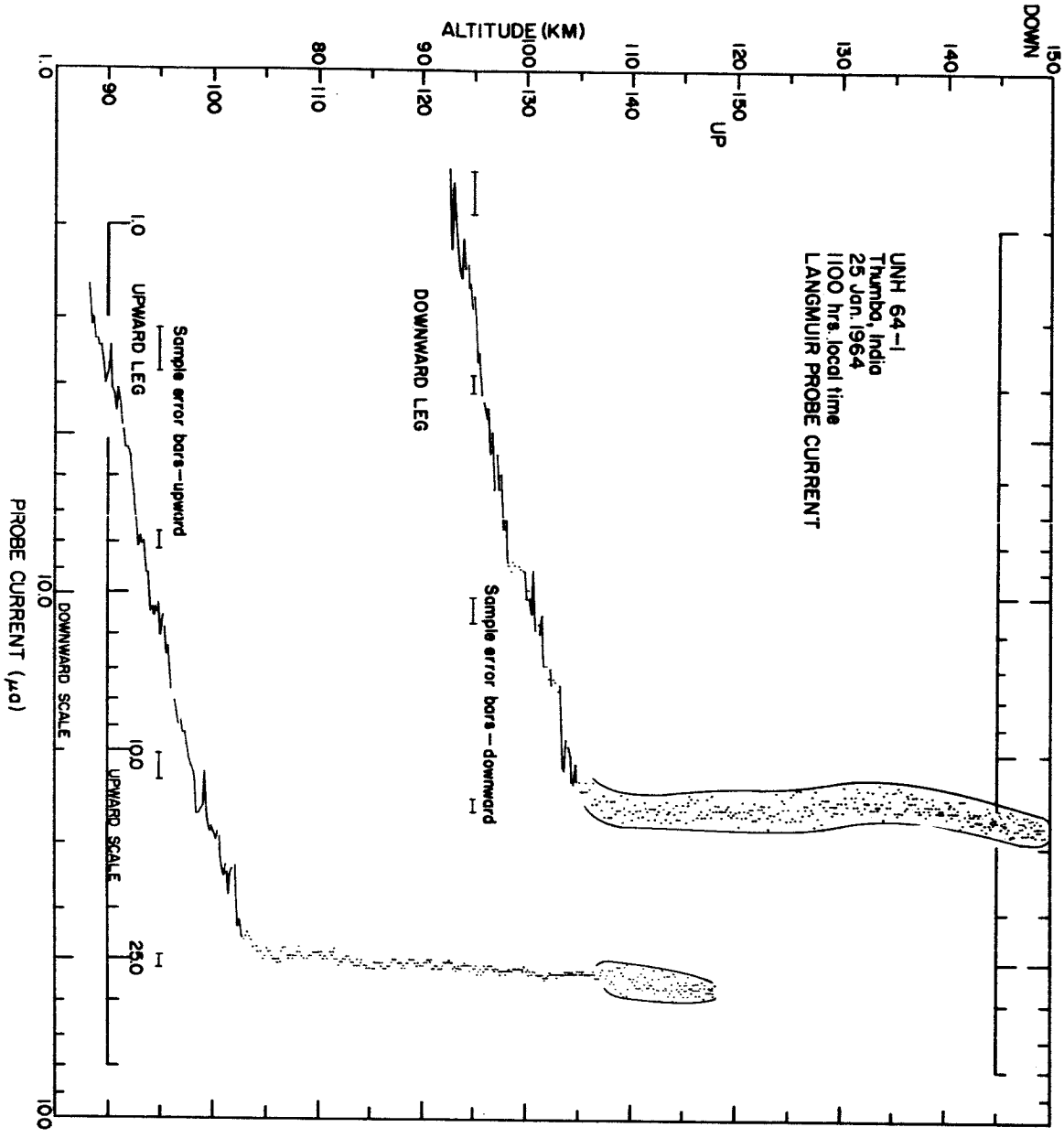
ALTITUDE (KM)
DOWN
UP
UNH 64-1
Thumba, India
25 Jan. 1964
1100 hrs. local time
LANGMUIR PROBE CURRENT
DOWNWARD LEG
Sample error bars – downward
UPWARD LEG
Sample error bars – upward
DOWNWARD SCALE
UPWARD SCALE
PROBE CURRENT (μa)

Figure 40

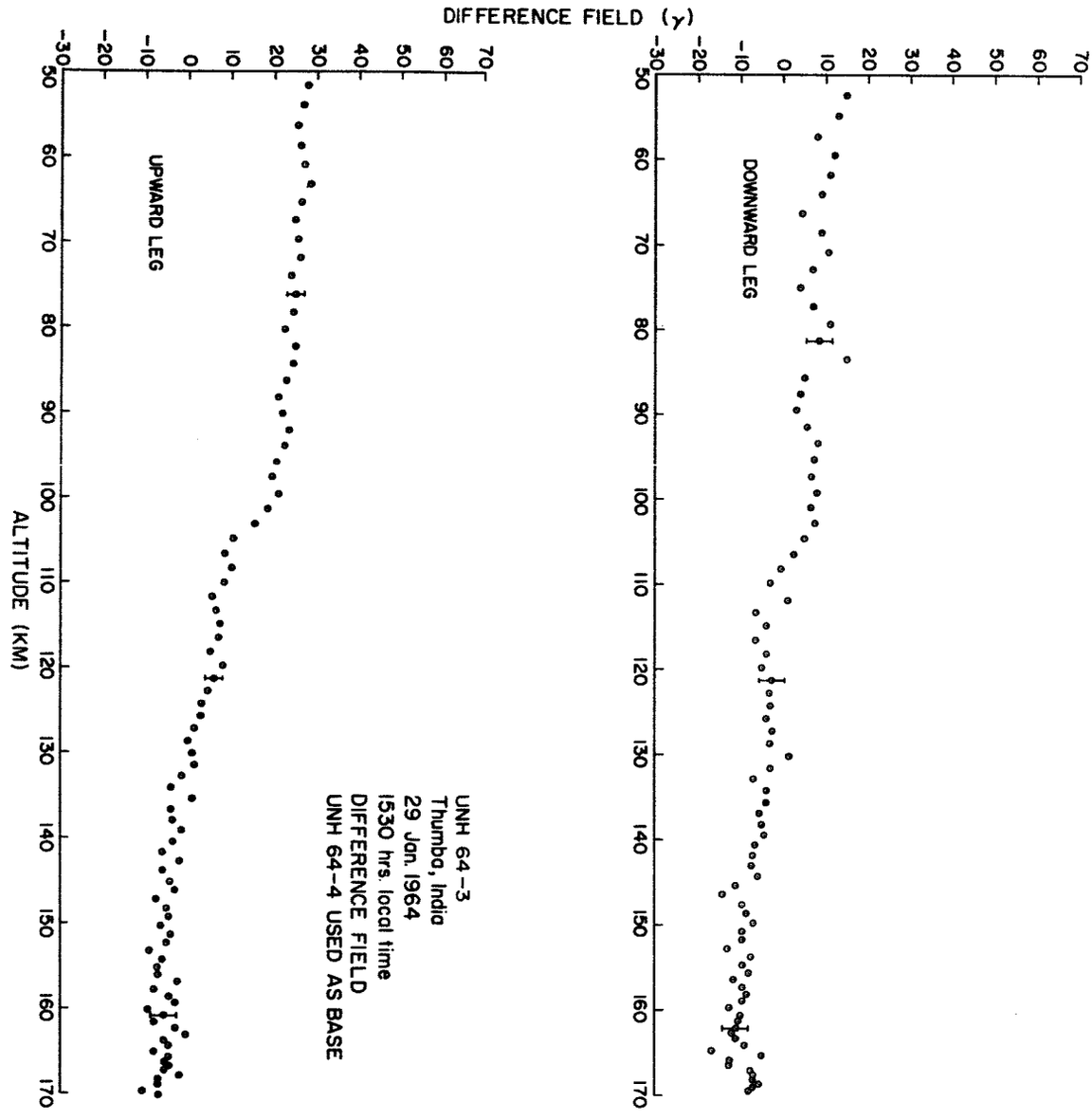
DIFFERENCE FIELD (γ)
ALTITUDE (KM)
UPWARD LEG
DOWNWARD LEG
UNH 64-3
Thumba, India
29 Jan. 1964
1530 hrs. local time
DIFFERENCE FIELD
UNH 64-4 USED AS BASE

Figure 41

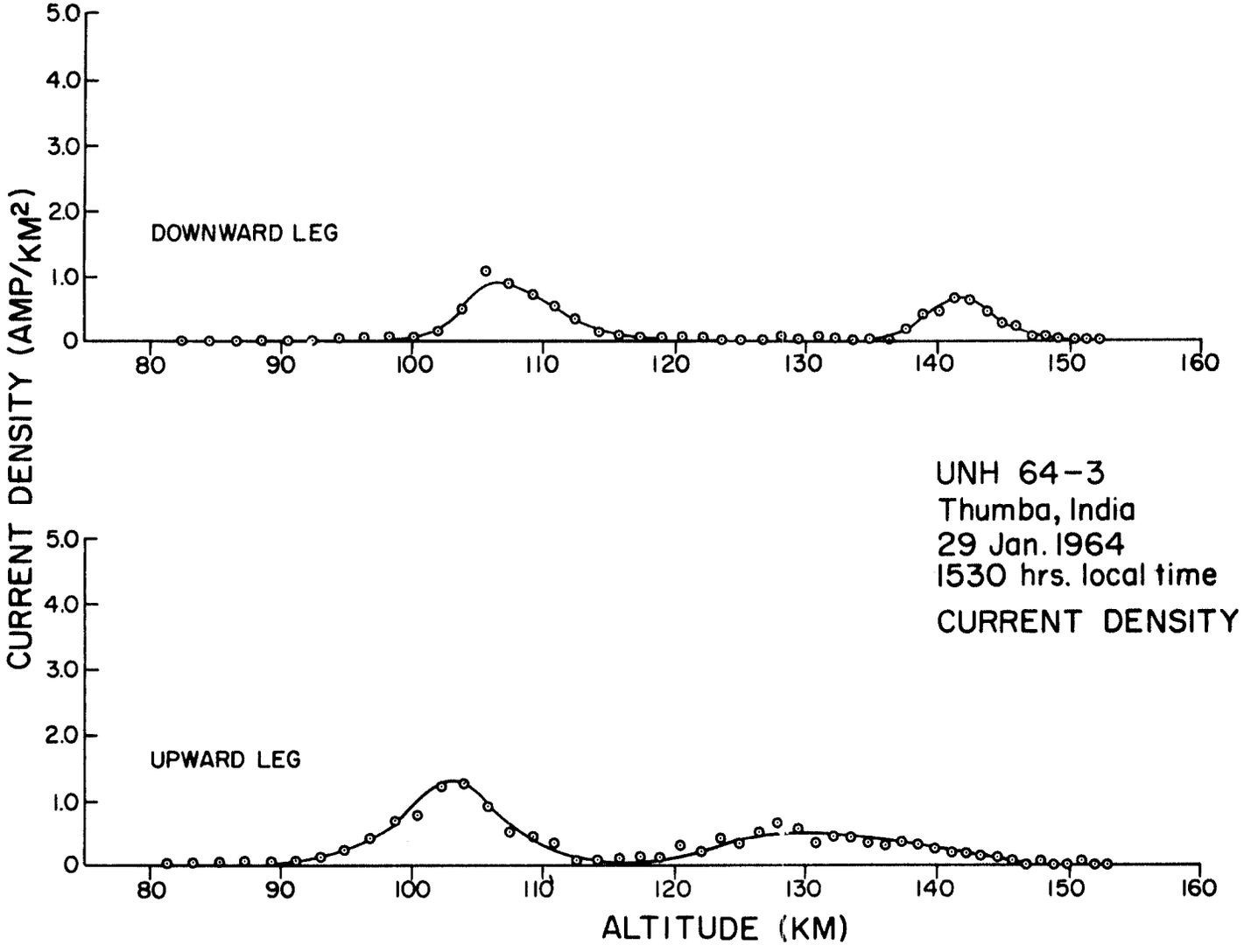
5.0
4.0
3.0
2.0
1.0
0
DOWNWARD LEG
80
90
100
110
120
130
140
150
160
CURRENT DENSITY (AMP/KM²)
UNH 64-3
Thumba, India
29 Jan. 1964
1530 hrs. local time
CURRENT DENSITY
UPWARD LEG
ALTITUDE (KM)

Figure 42

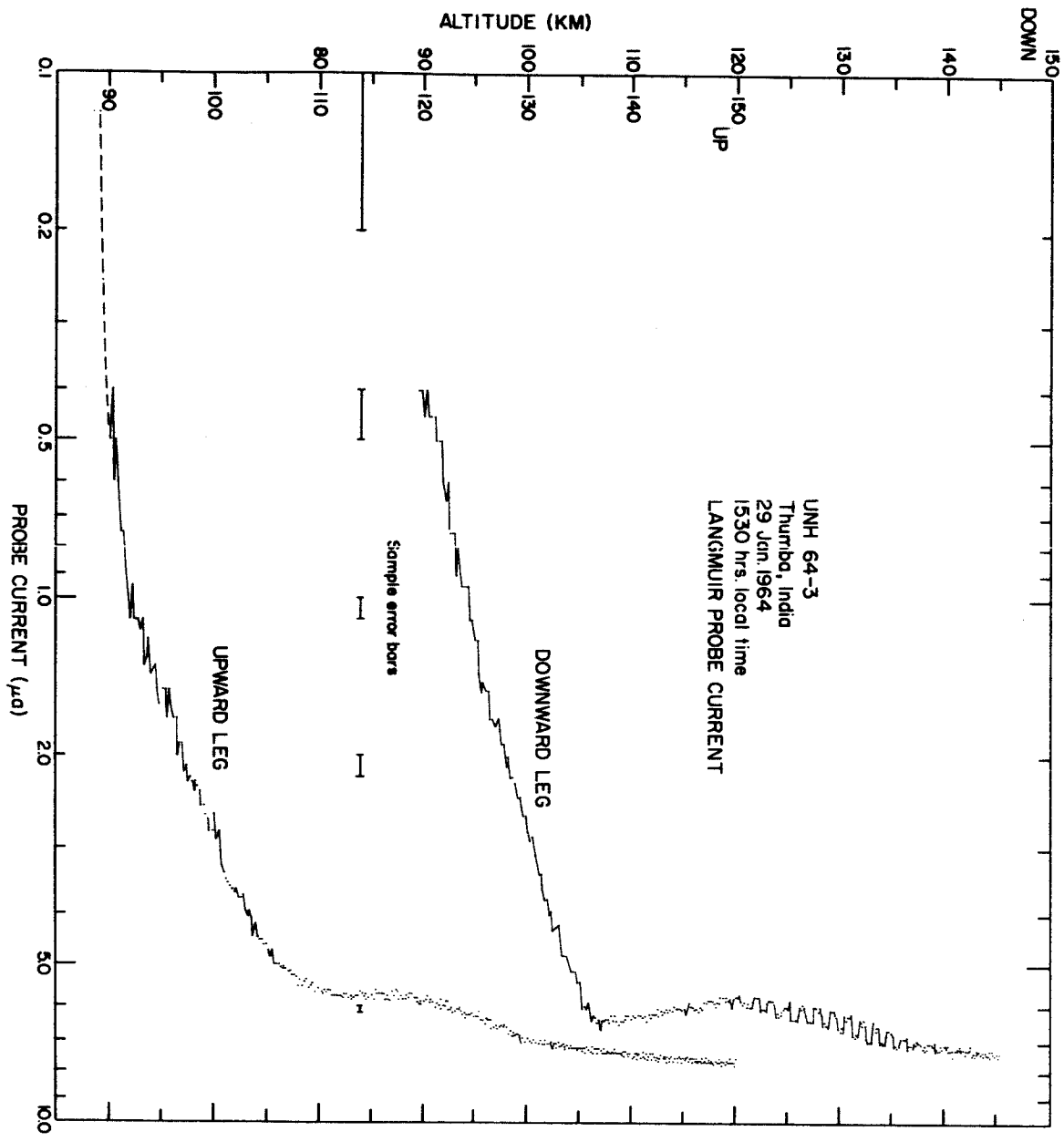
ALTITUDE (KM)
DOWN
UP
UNH 64-3
Thumba, India
29 Jan. 1964
1530 hrs. local time
LANGMUIR PROBE CURRENT
DOWNWARD LEG
UPWARD LEG
Sample error bars
PROBE CURRENT (μa)

Figure 43

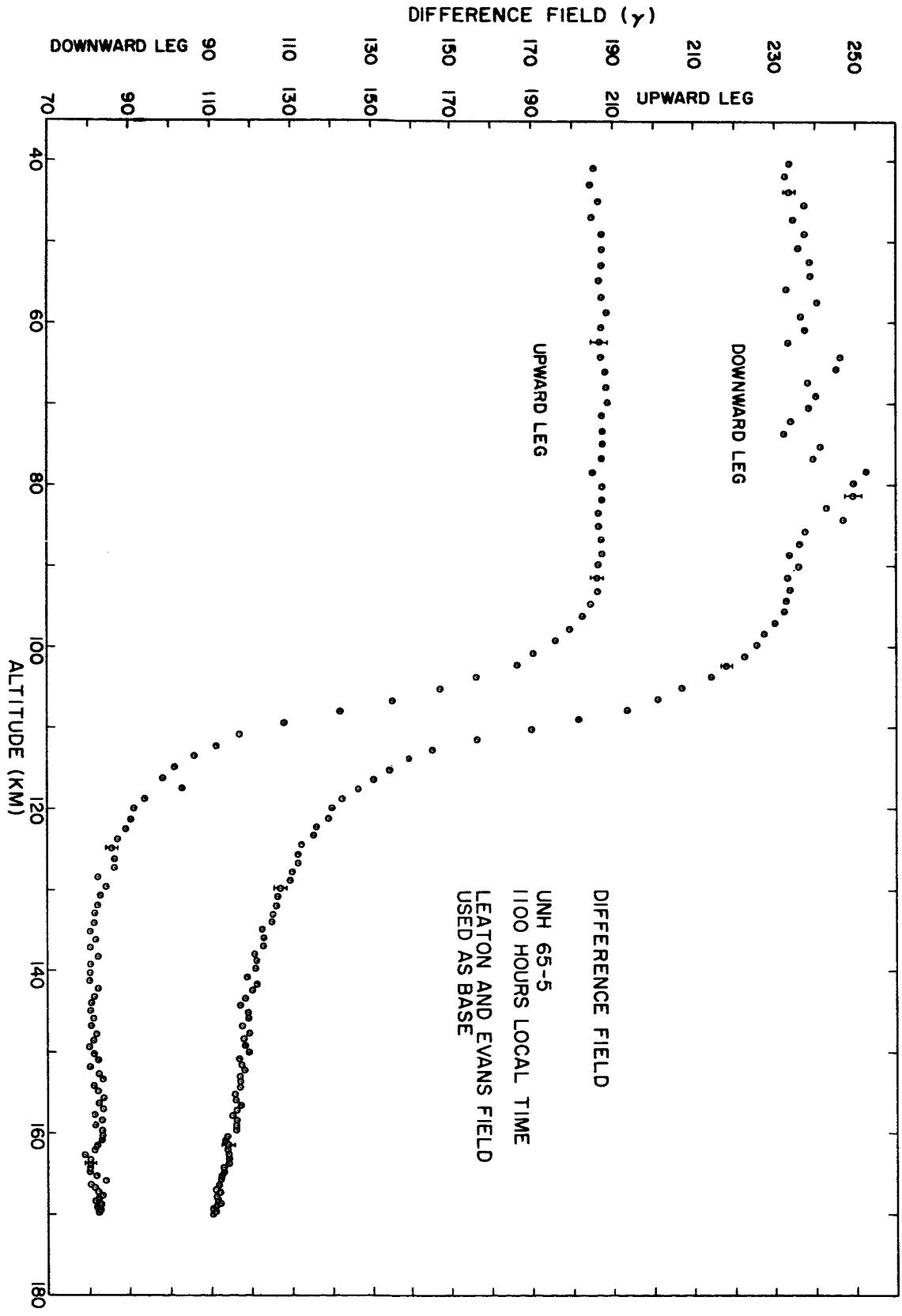
DIFFERENCE FIELD (γ)
DOWNWARD LEG
UPWARD LEG
ALTITUDE (KM)
UPWARD LEG
DOWNWARD LEG
DIFFERENCE FIELD
UNH 65-5
1100 HOURS LOCAL TIME
LEATON AND EVANS FIELD
USED AS BASE

Figure 44

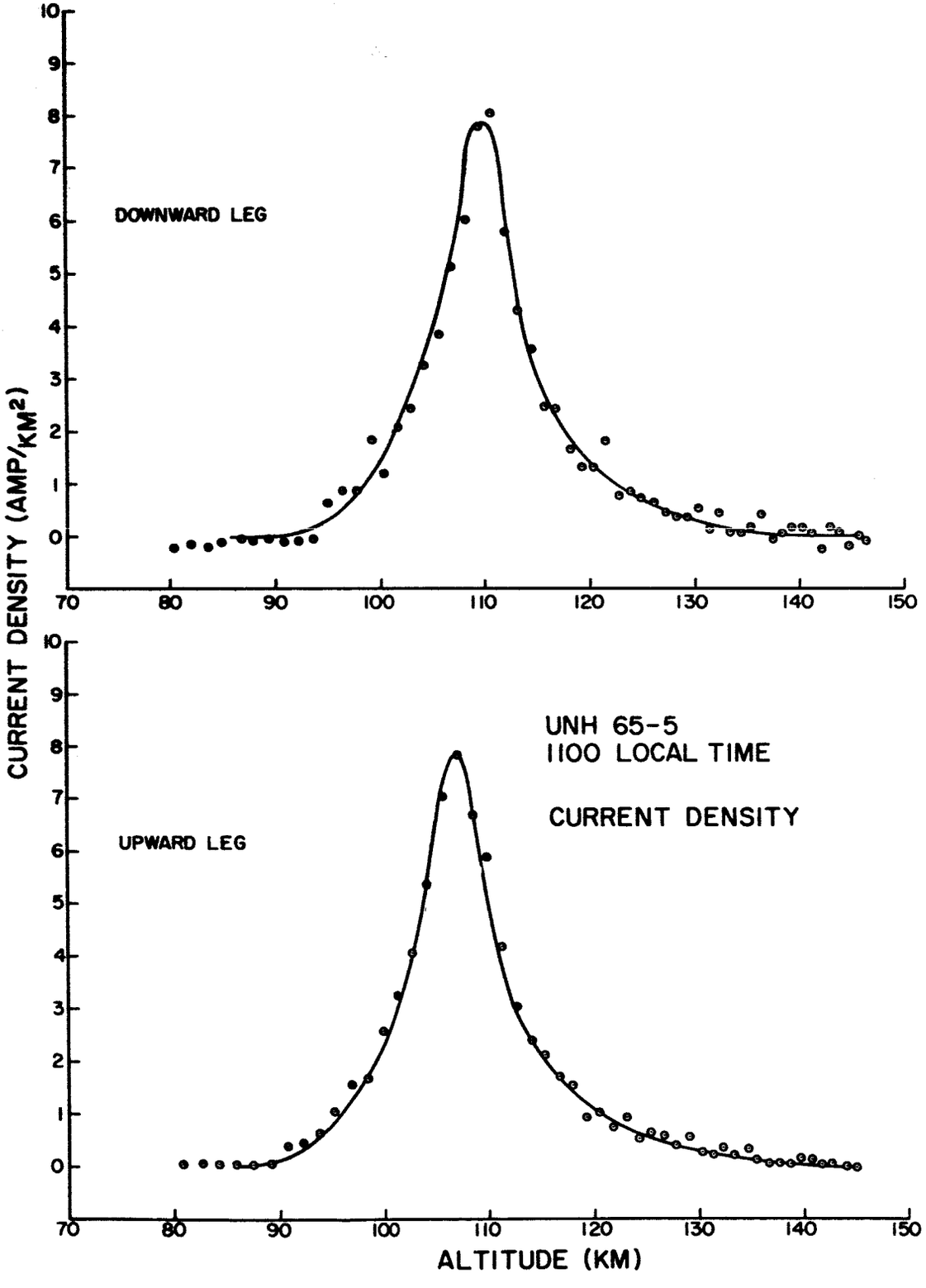
DOWNWARD LEG
UPWARD LEG
UNH 65-5
1100 LOCAL TIME
CURRENT DENSITY
CURRENT DENSITY (AMP/KM²)
ALTITUDE (KM)
0
1
2
3
4
5
6
7
8
9
10
70
80
90
100
110
120
130
140
150

Figure 45

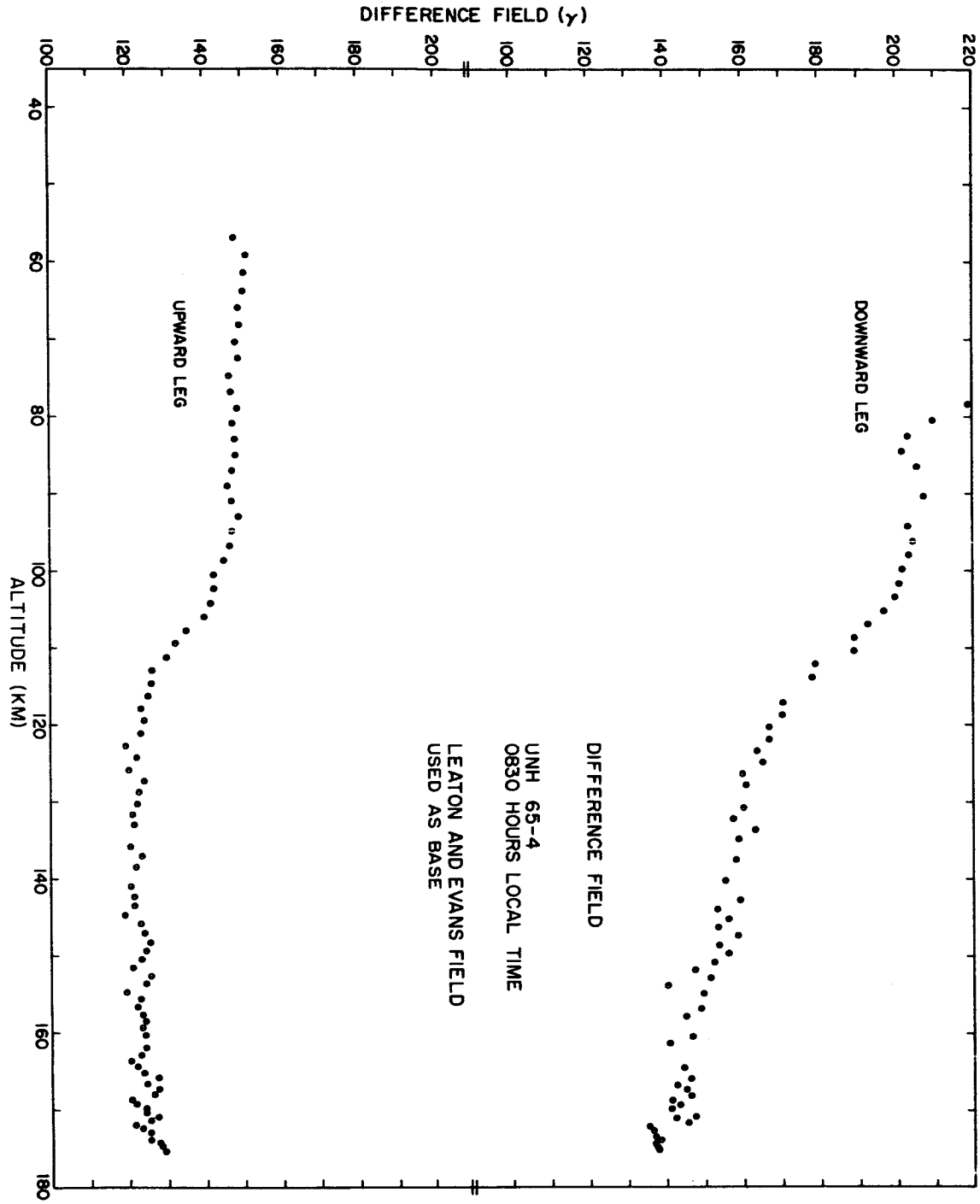
DIFFERENCE FIELD (γ)
100
120
140
160
180
200
220
40
60
80
100
120
140
160
180
ALTITUDE (KM)
DOWNWARD LEG
UPWARD LEG
DIFFERENCE FIELD
UNH 65-4
0830 HOURS LOCAL TIME
LEATON AND EVANS FIELD
USED AS BASE

Figure 46

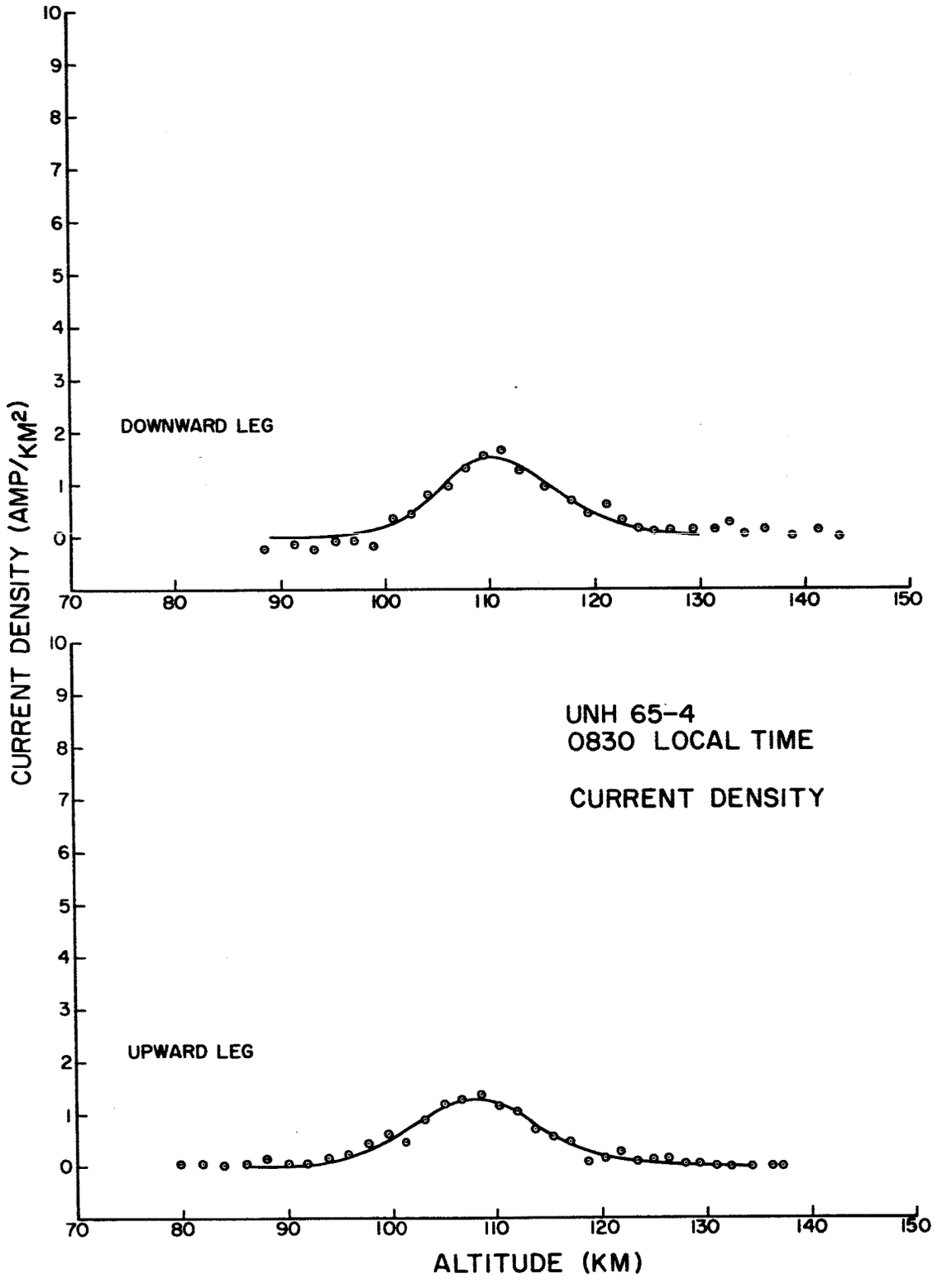
CURRENT DENSITY (AMP/KM²)
DOWNWARD LEG
UPWARD LEG
UNH 65-4
0830 LOCAL TIME
CURRENT DENSITY
ALTITUDE (KM)
0
1
2
3
4
5
6
7
8
9
10
70
80
90
100
110
120
130
140
150

Figure 47

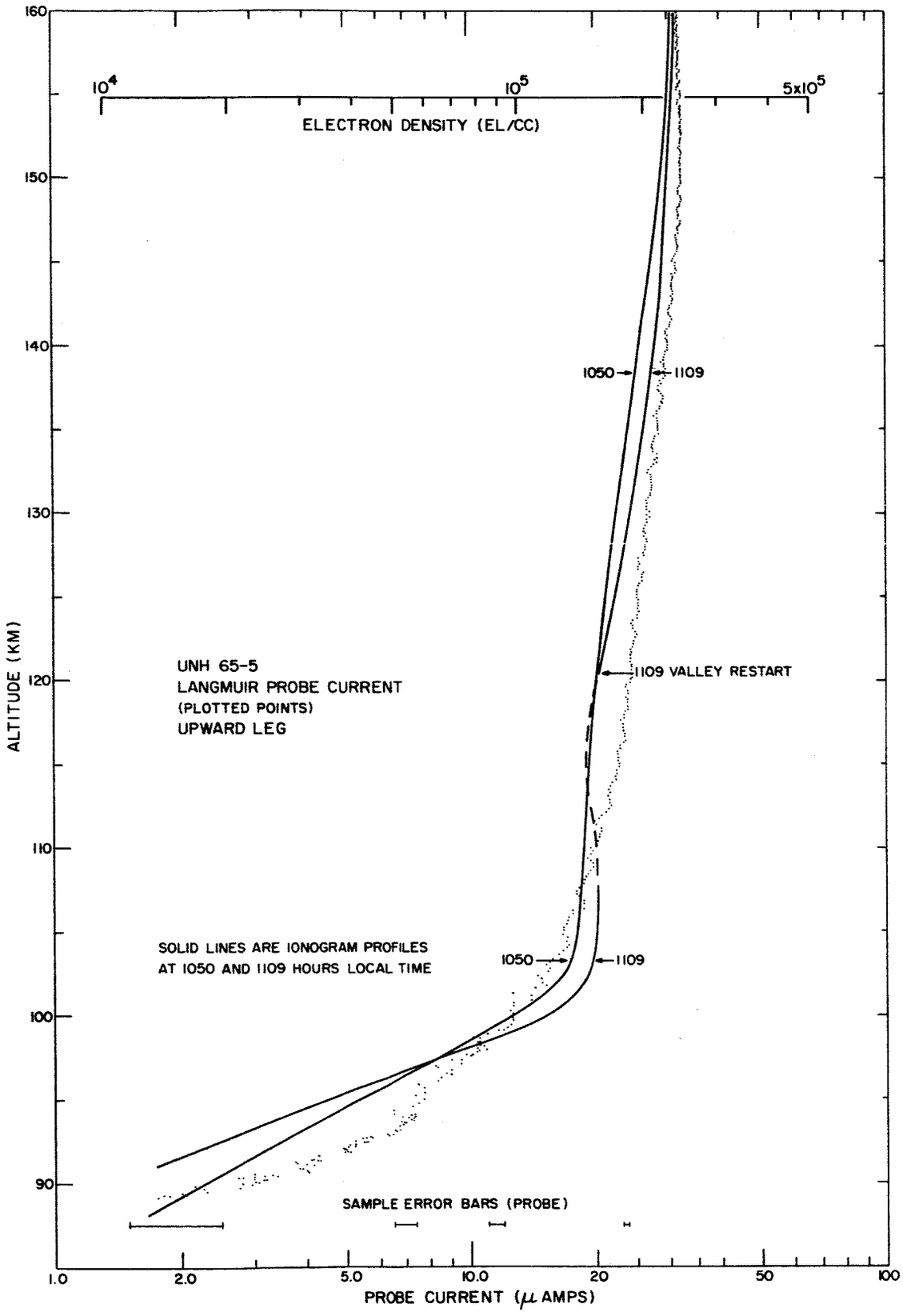
ELECTRON DENSITY (EL/CC)
10^4
10^5
$5x10^5$
ALTITUDE (KM)
160
150
140
130
120
110
100
90
1050
1109
1109 VALLEY RESTART
UNH 65-5
LANGMUIR PROBE CURRENT
(PLOTTED POINTS)
UPWARD LEG
SOLID LINES ARE IONOGRAM PROFILES
AT 1050 AND 1109 HOURS LOCAL TIME
1050
1109
SAMPLE ERROR BARS (PROBE)
1.0
2.0
5.0
10.0
20
50
100
PROBE CURRENT (μ AMPS)

Figure 48

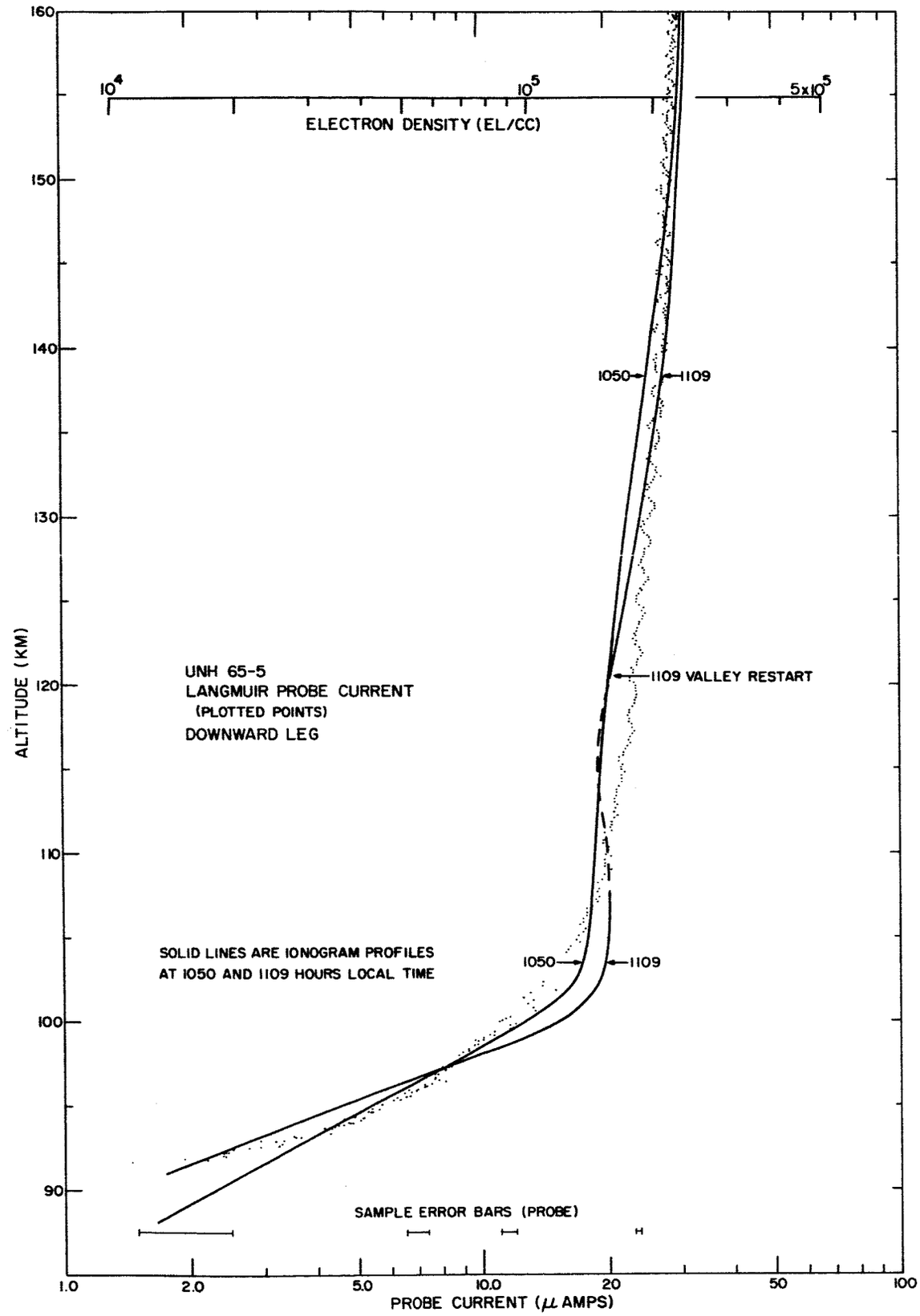
160
150
140
130
120
110
100
90
ALTITUDE (KM)
10^4
10^5
$5x10^5$
ELECTRON DENSITY (EL/CC)
1050
1109
UNH 65-5
LANGMUIR PROBE CURRENT
(PLOTTED POINTS)
DOWNWARD LEG
1109 VALLEY RESTART
SOLID LINES ARE IONOGRAM PROFILES
AT 1050 AND 1109 HOURS LOCAL TIME
1050
1109
SAMPLE ERROR BARS (PROBE)
1.0
2.0
5.0
10.0
20
50
100
PROBE CURRENT (μ AMPS)

Figure 49

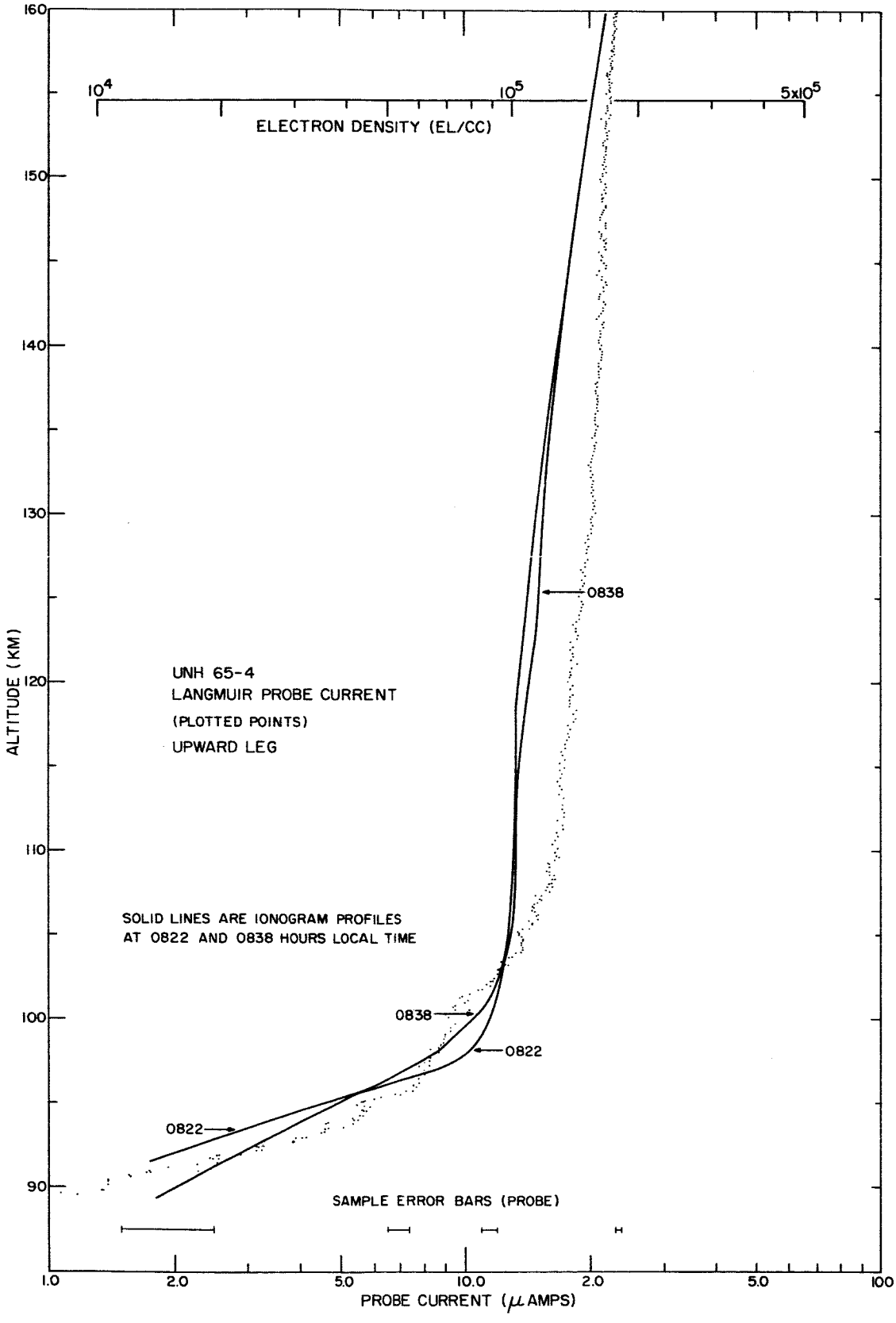
160
150
140
130
120
110
100
90
ALTITUDE (KM)
10^4
10^5
$5x10^5$
ELECTRON DENSITY (EL/CC)
0838
UNH 65-4
LANGMUIR PROBE CURRENT
(PLOTTED POINTS)
UPWARD LEG
SOLID LINES ARE IONOGRAM PROFILES
AT 0822 AND 0838 HOURS LOCAL TIME
0838
0822
0822
SAMPLE ERROR BARS (PROBE)
1.0
2.0
5.0
10.0
2.0
5.0
100
PROBE CURRENT (μAMPS)

Figure 50

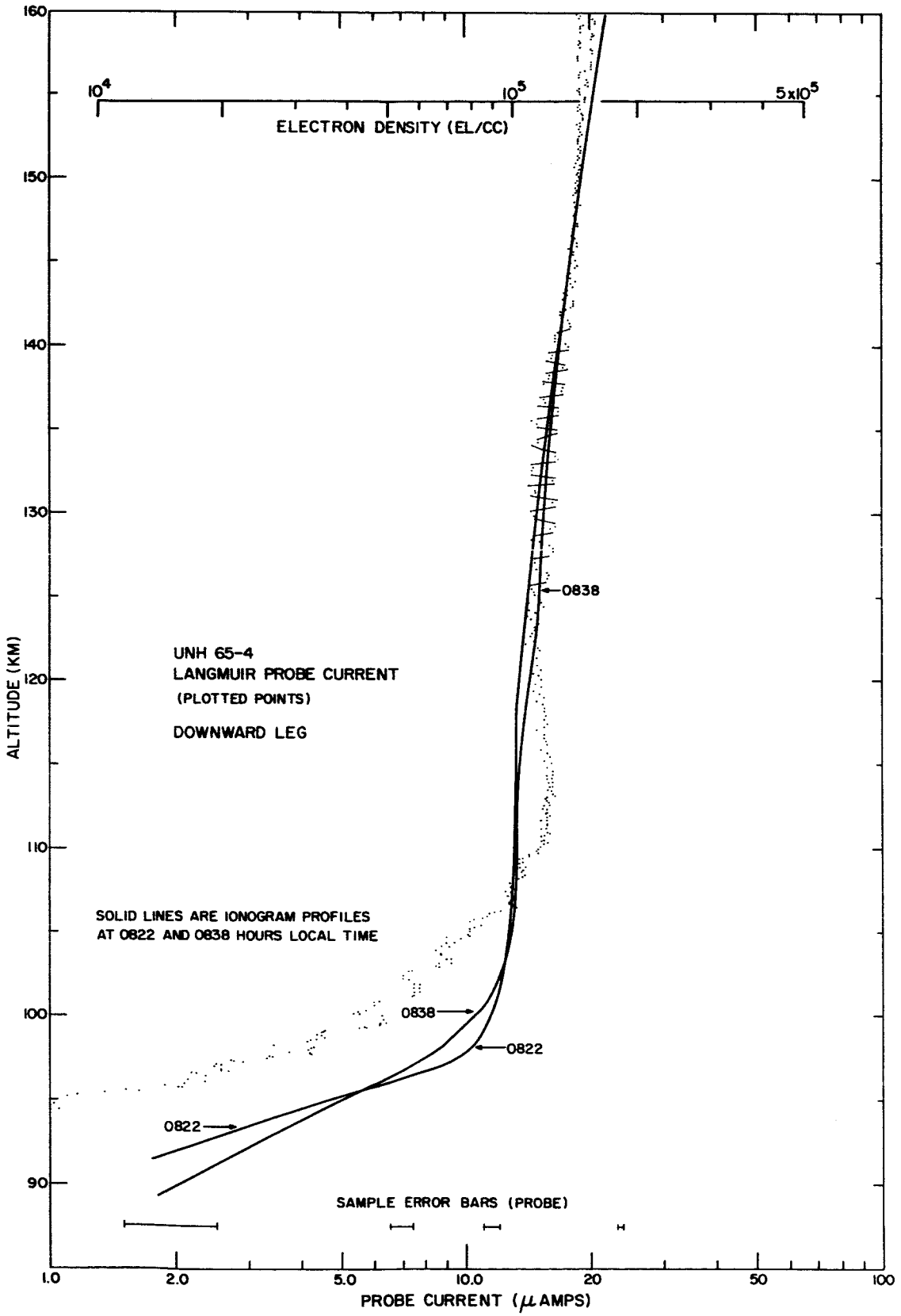
160
150
140
130
120
110
100
90
ALTITUDE (KM)
10^4
10^5
$5x10^5$
ELECTRON DENSITY (EL/CC)
UNH 65-4
LANGMUIR PROBE CURRENT
(PLOTTED POINTS)
DOWNWARD LEG
0838
SOLID LINES ARE IONOGRAM PROFILES
AT 0822 AND 0838 HOURS LOCAL TIME
0838
0822
0822
SAMPLE ERROR BARS (PROBE)
1.0
2.0
5.0
10.0
20
50
100
PROBE CURRENT (μAMPS)

Figure 51

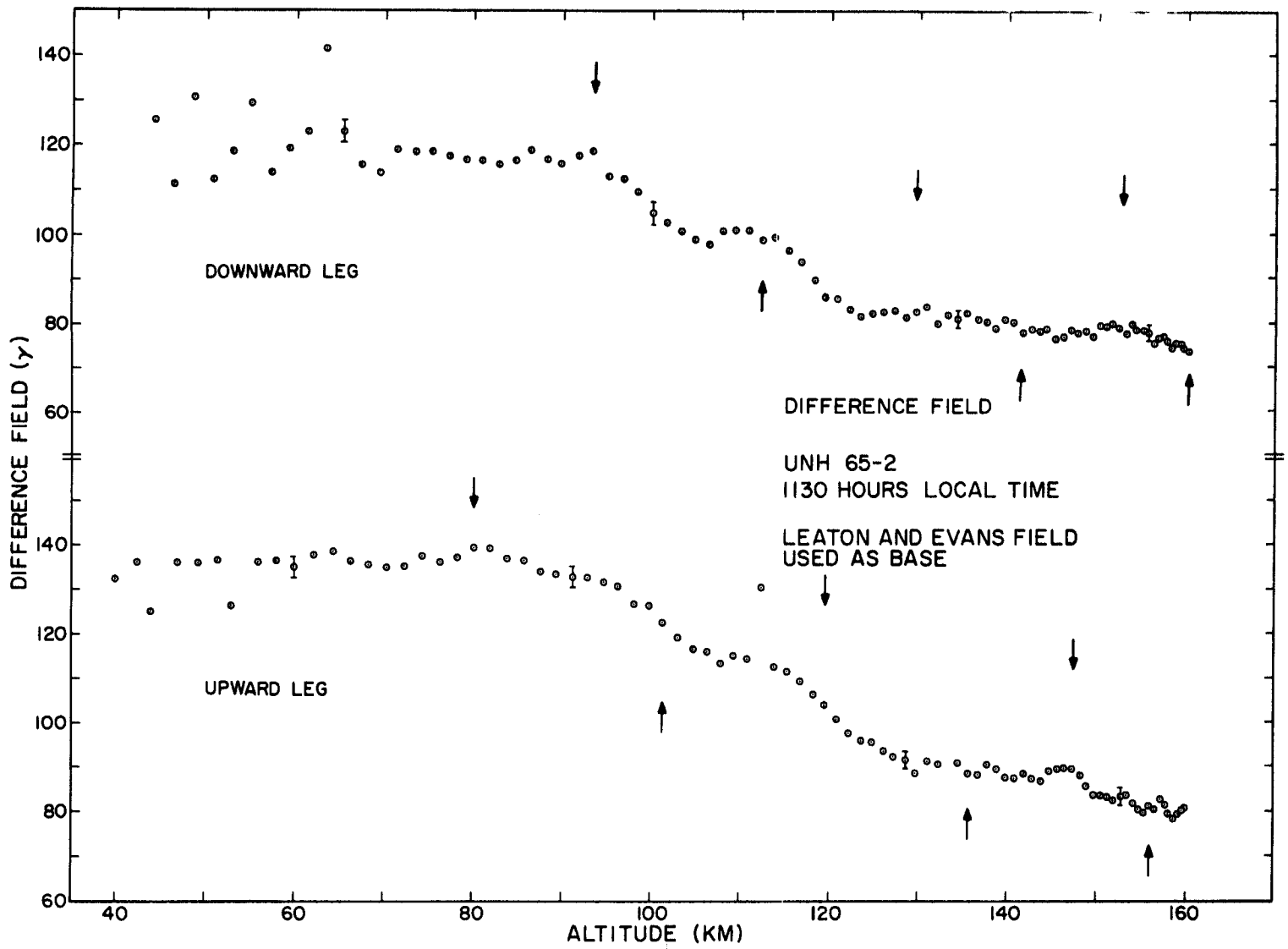
DIFFERENCE FIELD (γ)
ALTITUDE (KM)
DOWNWARD LEG
UPWARD LEG
DIFFERENCE FIELD
UNH 65-2
1130 HOURS LOCAL TIME
LEATON AND EVANS FIELD
USED AS BASE
140
120
100
80
60
40
160

Figure 52

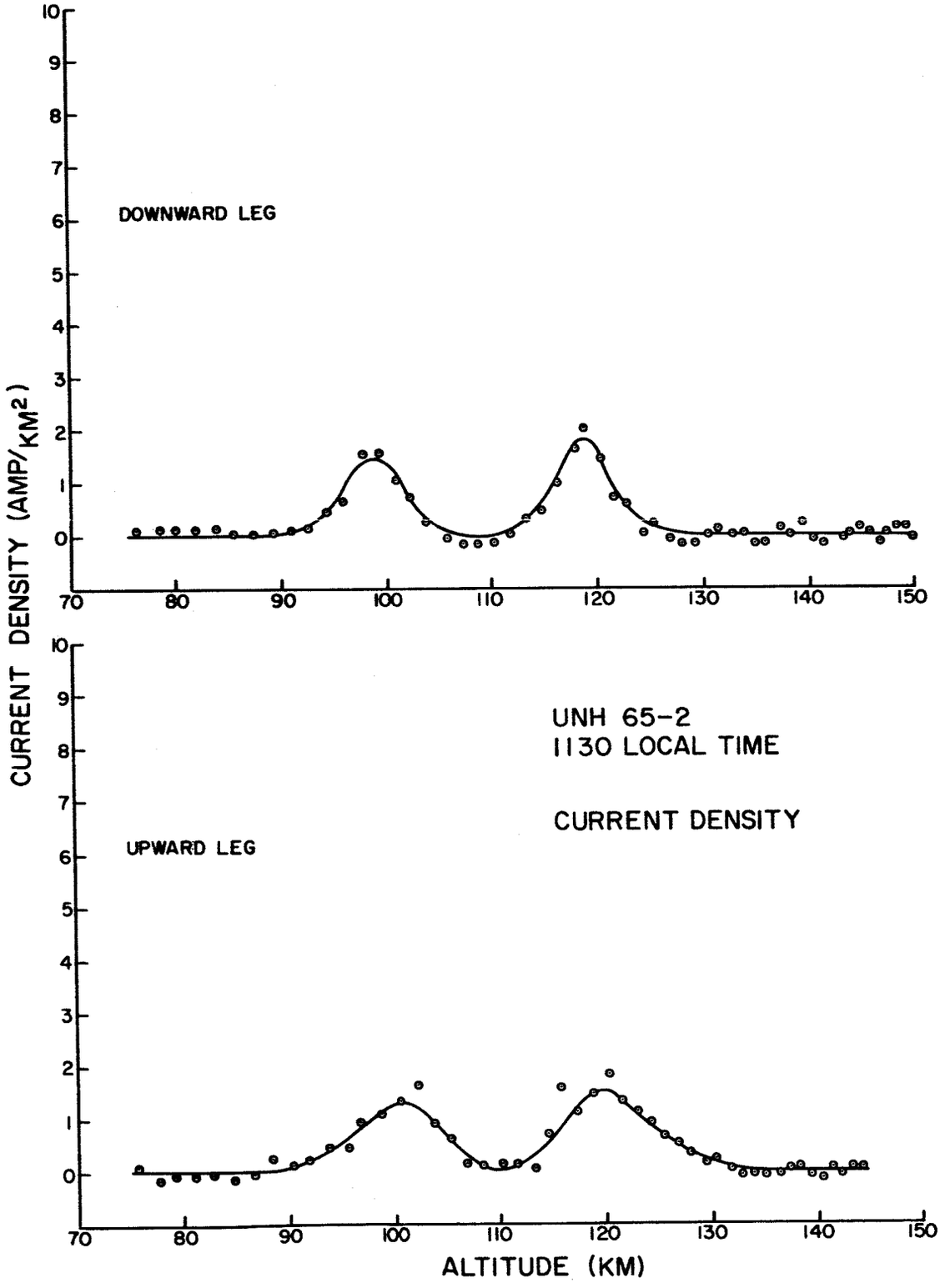
DOWNWARD LEG
UPWARD LEG
UNH 65-2
1130 LOCAL TIME
CURRENT DENSITY
CURRENT DENSITY (AMP/KM²)
ALTITUDE (KM)
0
1
2
3
4
5
6
7
8
9
10
70
80
90
100
110
120
130
140
150

Figure 53

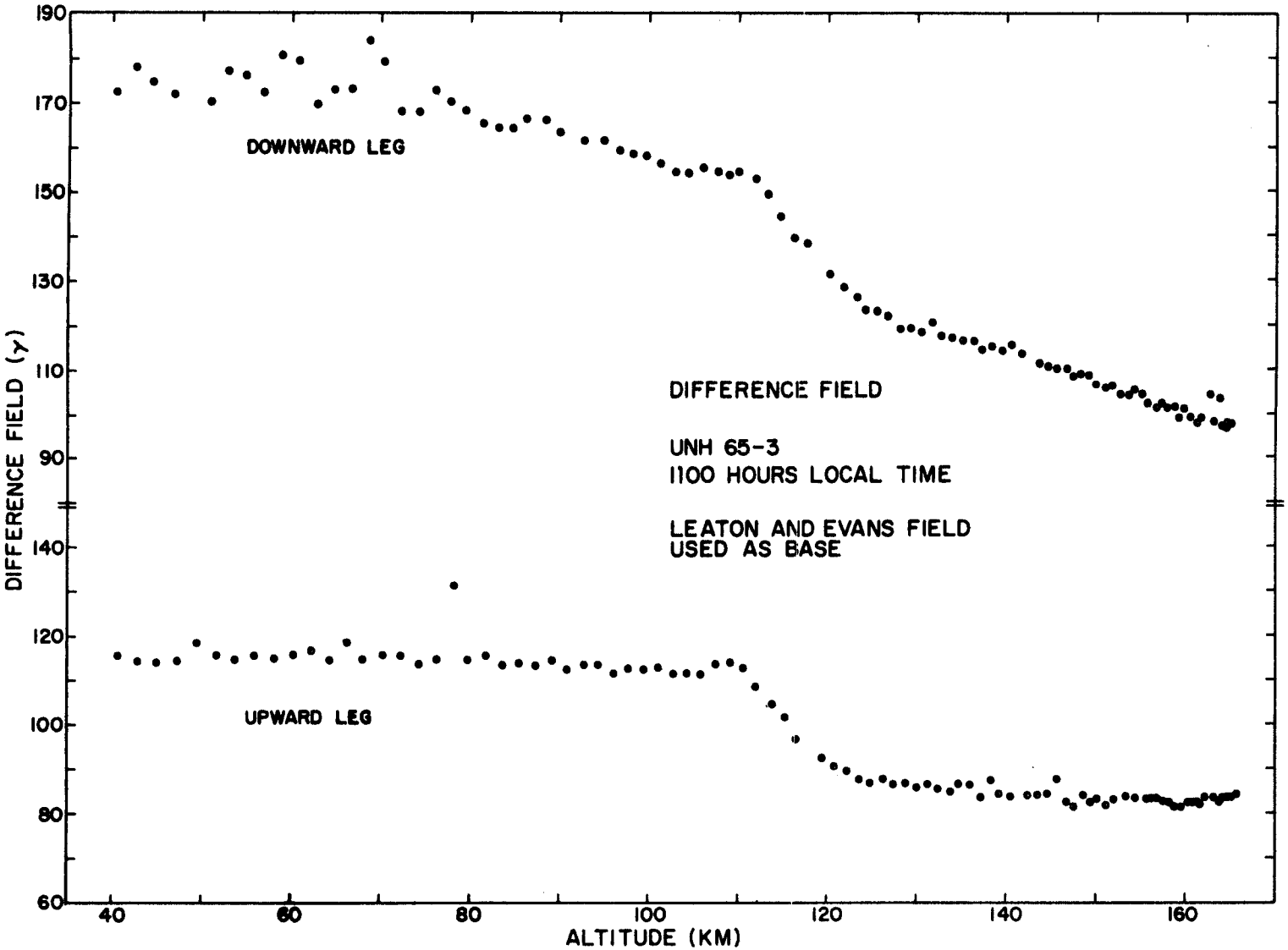
DOWNWARD LEG
UPWARD LEG
DIFFERENCE FIELD
UNH 65-3
1100 HOURS LOCAL TIME
LEATON AND EVANS FIELD
USED AS BASE
DIFFERENCE FIELD (γ)
ALTITUDE (KM)
190
170
150
130
110
90
140
120
100
80
60
40
60
80
100
120
140
160

Figure 54

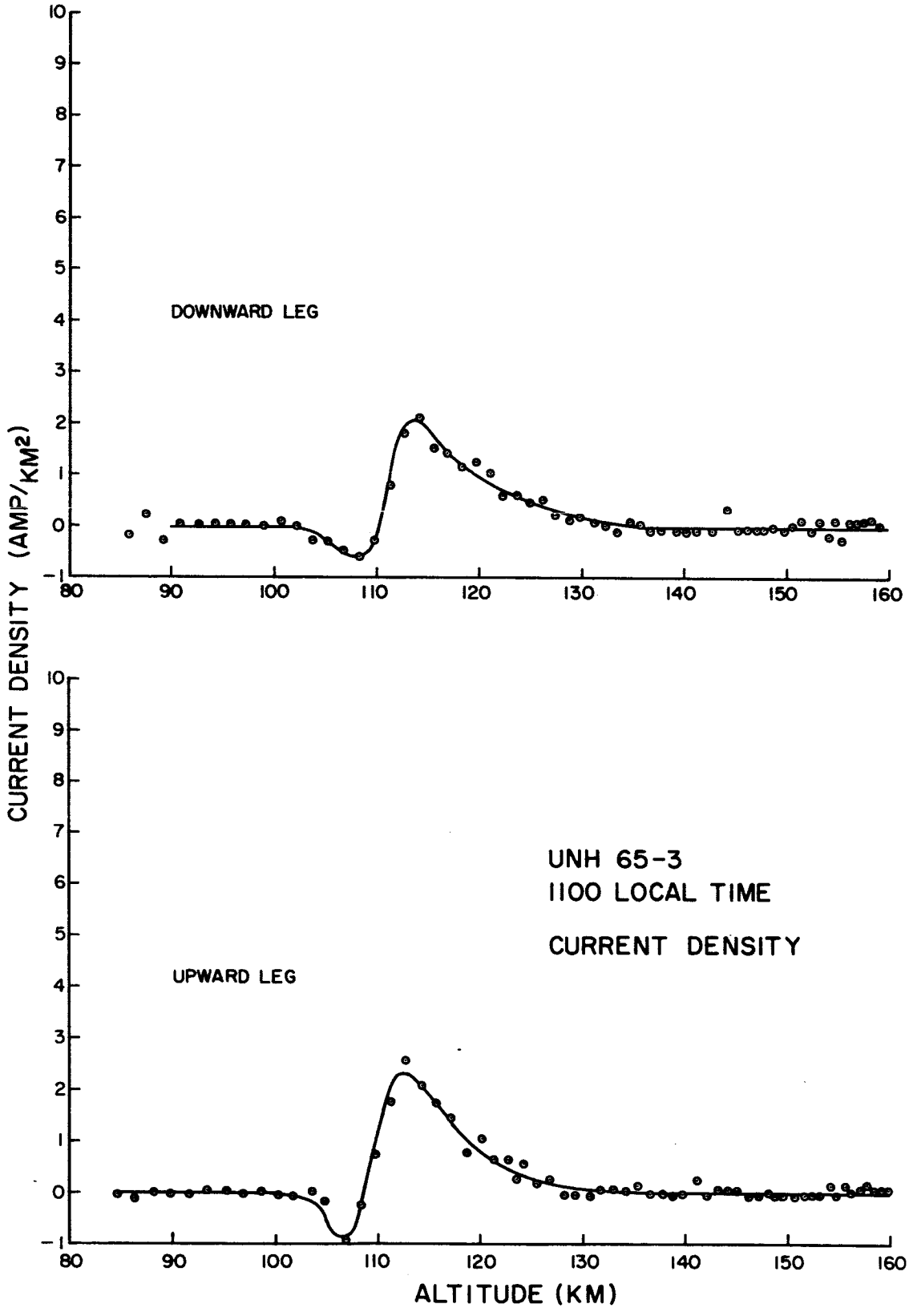
DOWNWARD LEG
UPWARD LEG
UNH 65-3
1100 LOCAL TIME
CURRENT DENSITY
CURRENT DENSITY (AMP/KM2)
ALTITUDE (KM)
10
9
8
7
6
5
4
3
2
1
0
-1
80
90
100
110
120
130
140
150
160

Figure 55

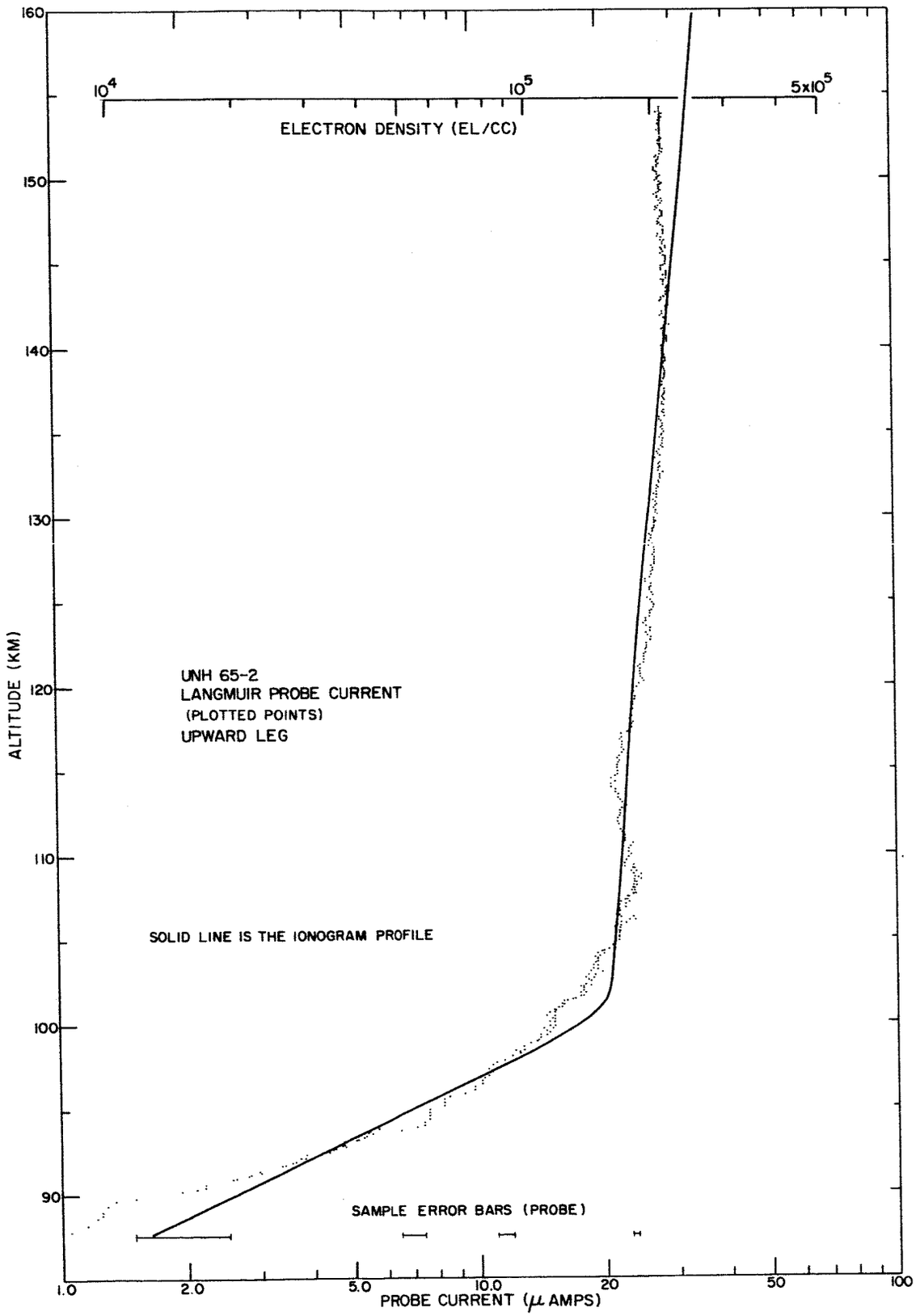
160
150
140
130
120
110
100
90
ALTITUDE (KM)
10^4
10^5
$5x10^5$
ELECTRON DENSITY (EL/CC)
UNH 65-2
LANGMUIR PROBE CURRENT
(PLOTTED POINTS)
UPWARD LEG
SOLID LINE IS THE IONOGRAM PROFILE
SAMPLE ERROR BARS (PROBE)
1.0
2.0
5.0
10.0
20
50
100
PROBE CURRENT (μ AMPS)

Figure 56

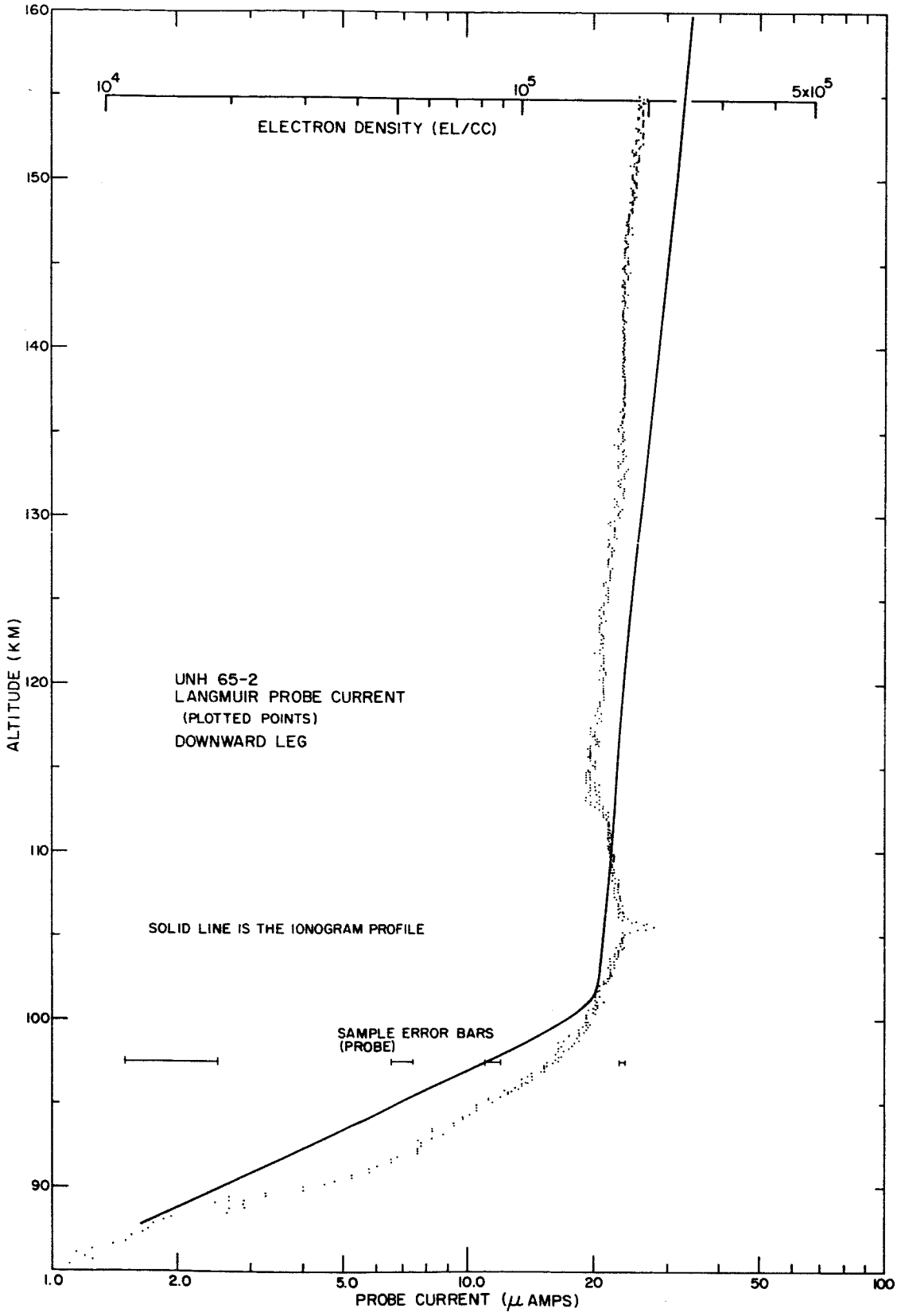
160
150
140
130
120
110
100
90
ALTITUDE (KM)
10^4
10^5
$5x10^5$
ELECTRON DENSITY (EL/CC)
UNH 65-2
LANGMUIR PROBE CURRENT
(PLOTTED POINTS)
DOWNWARD LEG
SOLID LINE IS THE IONOGRAM PROFILE
SAMPLE ERROR BARS
(PROBE)
1.0
2.0
5.0
10.0
20
50
100
PROBE CURRENT (μ AMPS)

Figure 57

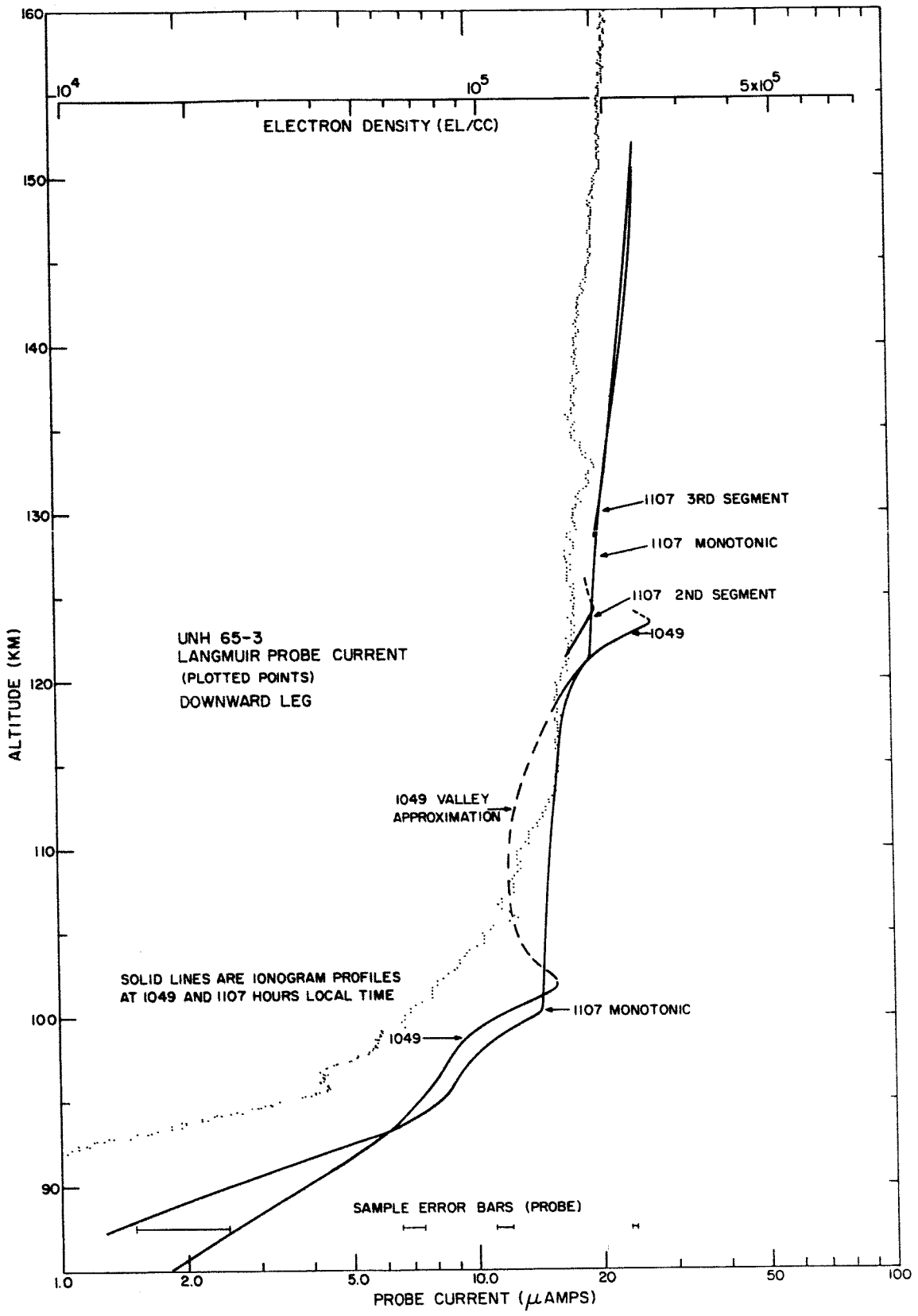
160
150
140
130
120
110
100
90
ALTITUDE (KM)
10^4
10^5
$5x10^5$
ELECTRON DENSITY (EL/CC)
UNH 65-3
LANGMUIR PROBE CURRENT
(PLOTTED POINTS)
DOWNWARD LEG
1107 3RD SEGMENT
1107 MONOTONIC
1107 2ND SEGMENT
1049
1049 VALLEY
APPROXIMATION
SOLID LINES ARE IONOGRAM PROFILES
AT 1049 AND 1107 HOURS LOCAL TIME
1107 MONOTONIC
1049
SAMPLE ERROR BARS (PROBE)
1.0
2.0
5.0
10.0
20
50
100
PROBE CURRENT (μAMPS)

Figure 58

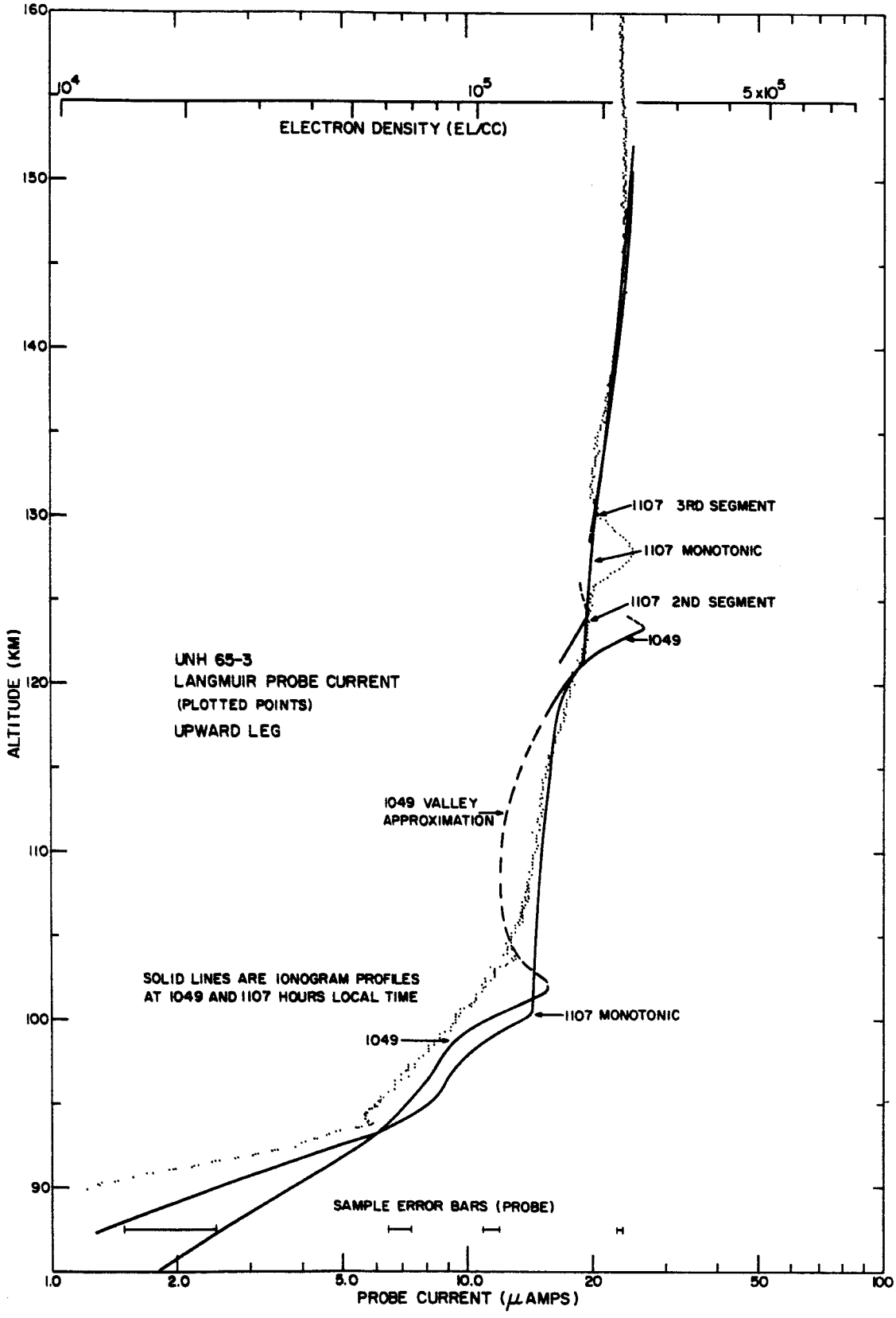
160
150
140
130
120
110
100
90
ALTITUDE (KM)
10^4
10^5
5×10^5
ELECTRON DENSITY (EL/CC)
1107 3RD SEGMENT
1107 MONOTONIC
1107 2ND SEGMENT
1049
UNH 65-3
LANGMUIR PROBE CURRENT
(PLOTTED POINTS)
UPWARD LEG
1049 VALLEY
APPROXIMATION
SOLID LINES ARE IONOGRAM PROFILES
AT 1049 AND 1107 HOURS LOCAL TIME
1107 MONOTONIC
1049
SAMPLE ERROR BARS (PROBE)
1.0
2.0
5.0
10.0
20
50
100
PROBE CURRENT (μ AMPS)

Figure 59

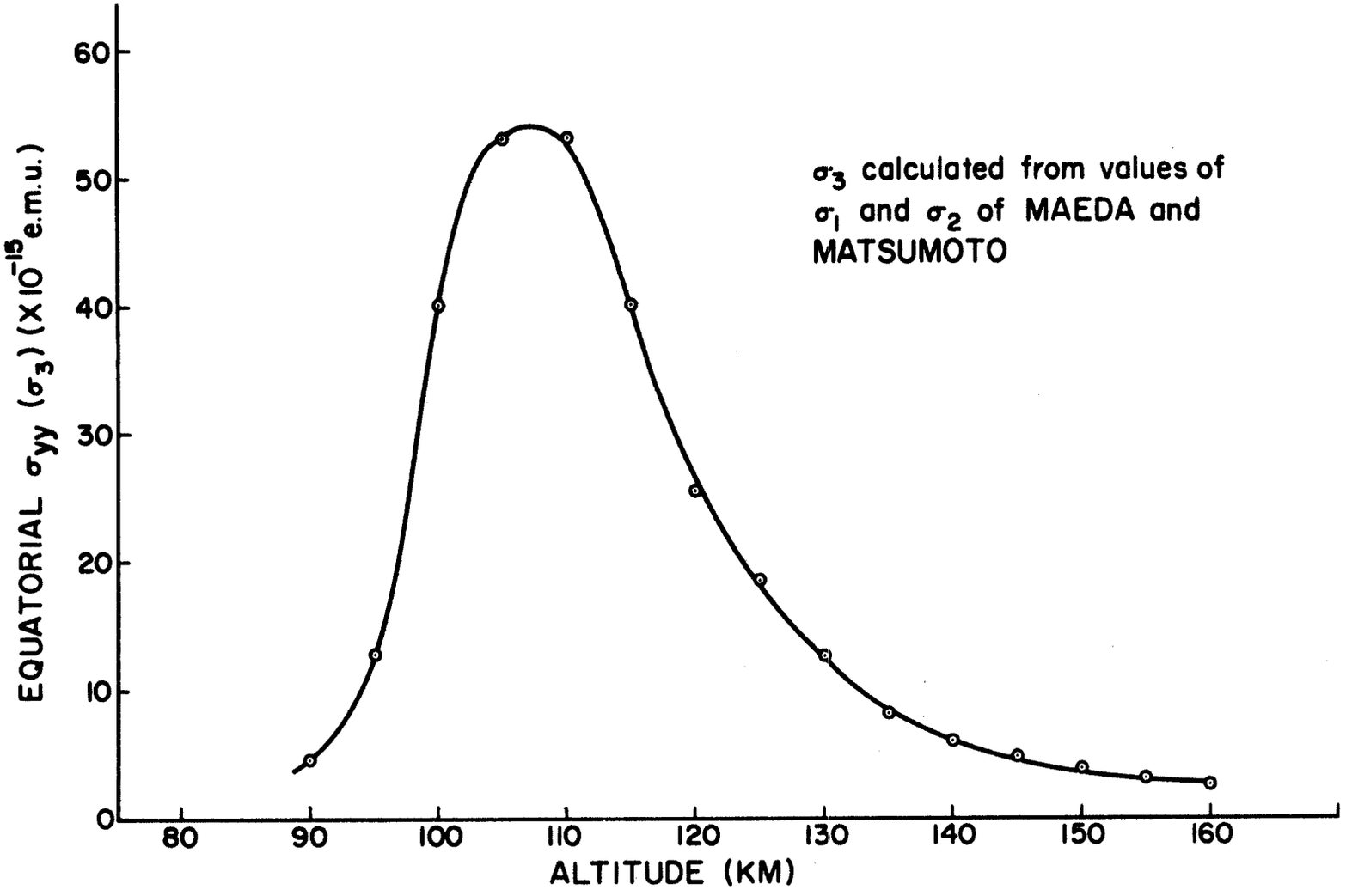
EQUATORIAL σ_{yy} (σ_3) (X 10^{-15} e.m.u.)
60
50
40
30
20
10
0
80
90
100
110
120
130
140
150
160
ALTITUDE (KM)
σ_3 calculated from values of σ_1 and σ_2 of MAEDA and MATSUMOTO

Figure 60

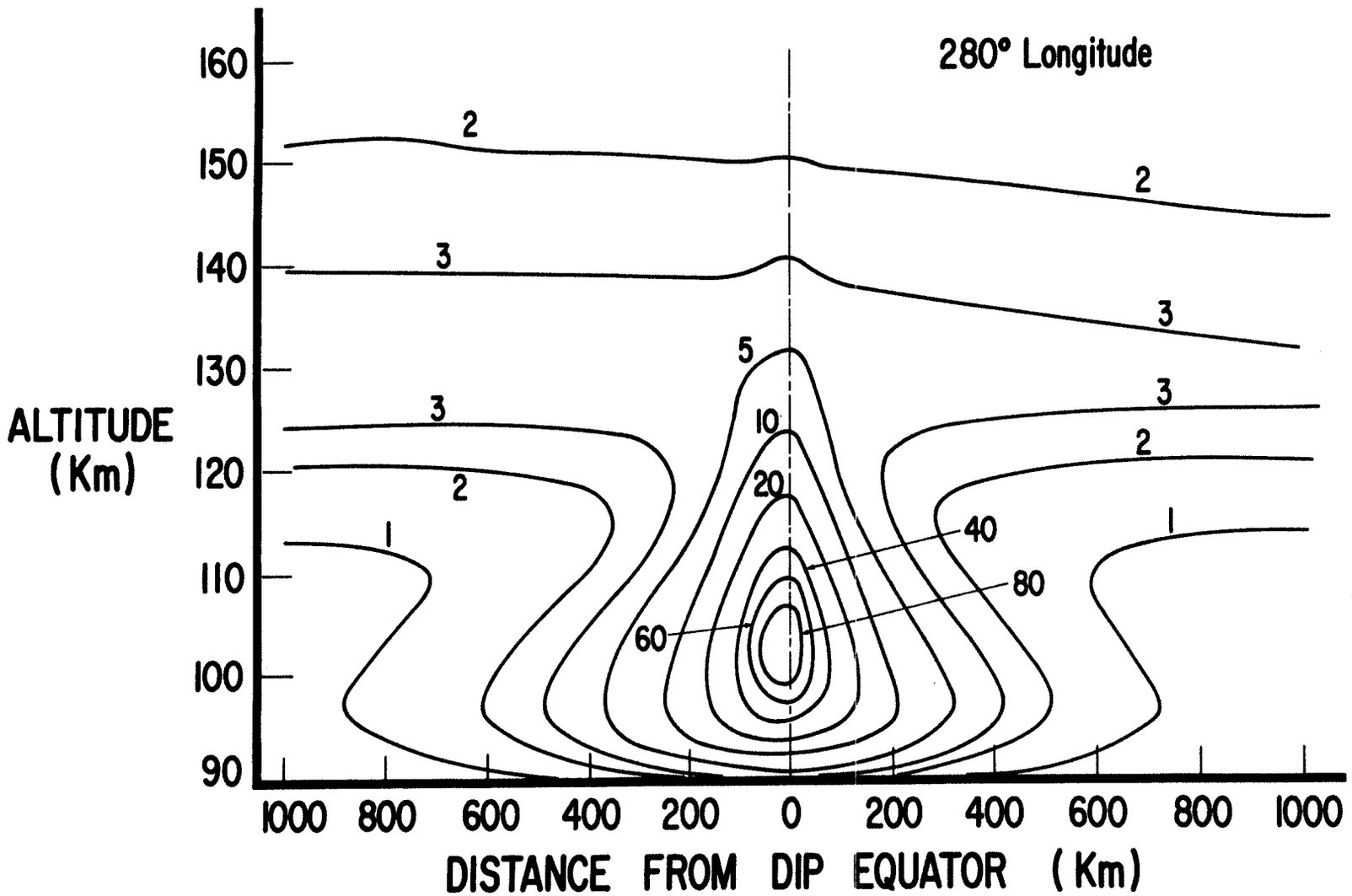
280° Longitude
ALTITUDE (Km)
160
150
140
130
120
110
100
90
1000 800 600 400 200 0 200 400 600 800 1000
DISTANCE FROM DIP EQUATOR (Km)
1
2
3
5
10
20
40
60
80

Figure 61

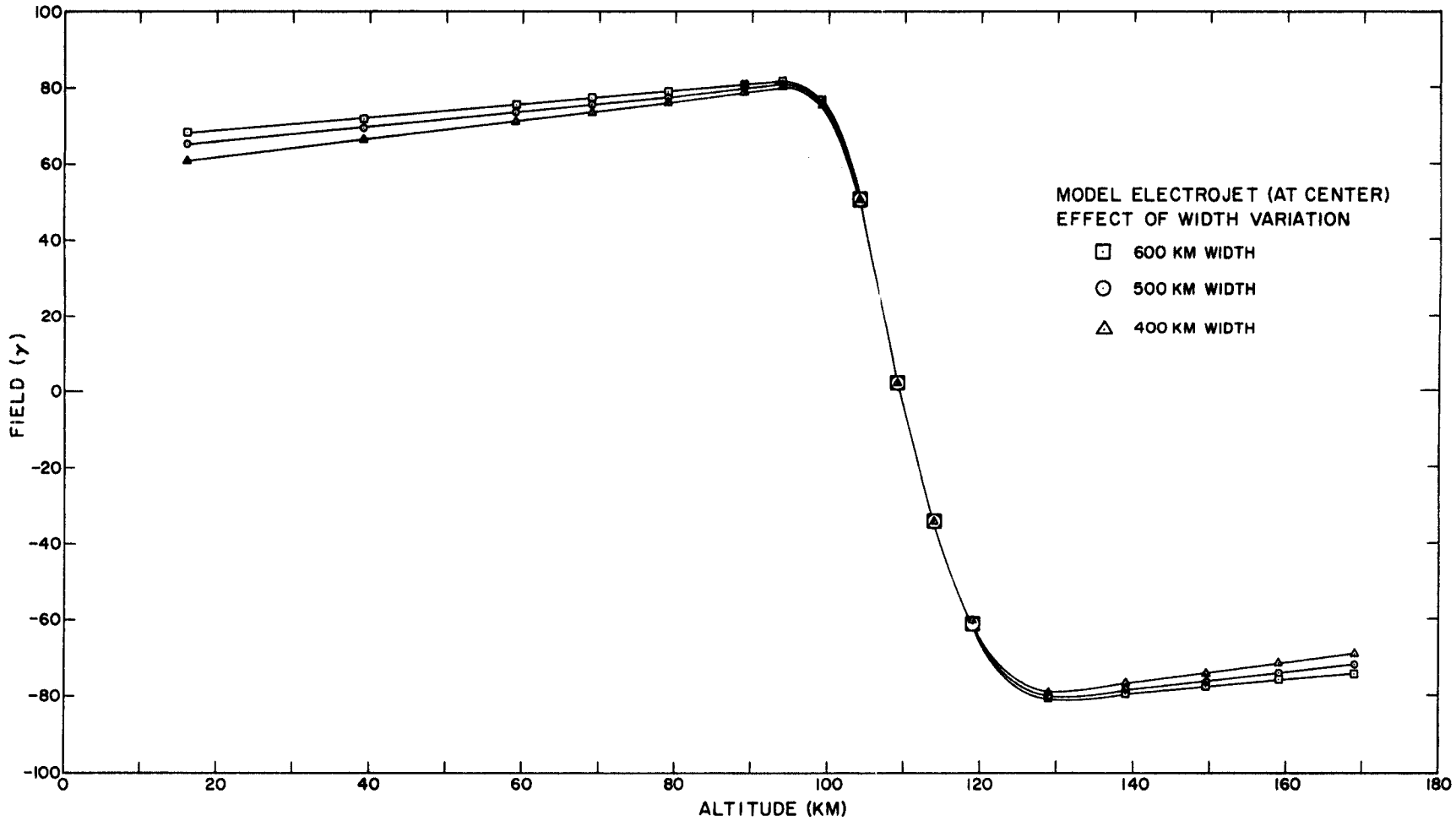
MODEL ELECTROJET (AT CENTER)
EFFECT OF WIDTH VARIATION
600 KM WIDTH
500 KM WIDTH
400 KM WIDTH
FIELD (γ)
ALTITUDE (KM)
100
80
60
40
20
0
-20
-40
-60
-80
-100
0
20
40
60
80
100
120
140
160
180

Figure 62

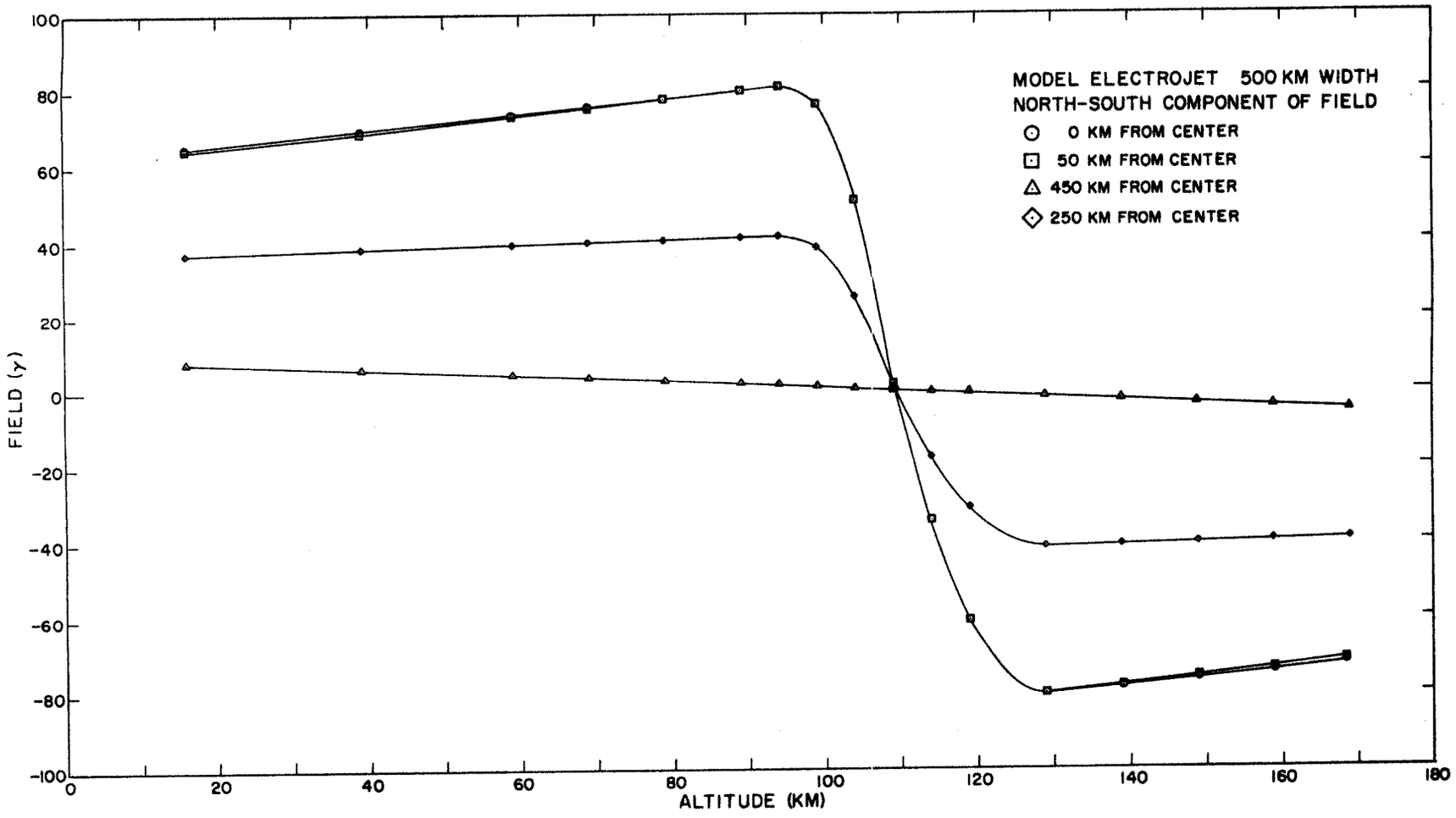
MODEL ELECTROJET 500 KM WIDTH
NORTH-SOUTH COMPONENT OF FIELD
0 KM FROM CENTER
50 KM FROM CENTER
450 KM FROM CENTER
250 KM FROM CENTER
FIELD (γ)
ALTITUDE (KM)
100
80
60
40
20
0
-20
-40
-60
-80
-100
0
20
40
60
80
100
120
140
160
180

Figure 63

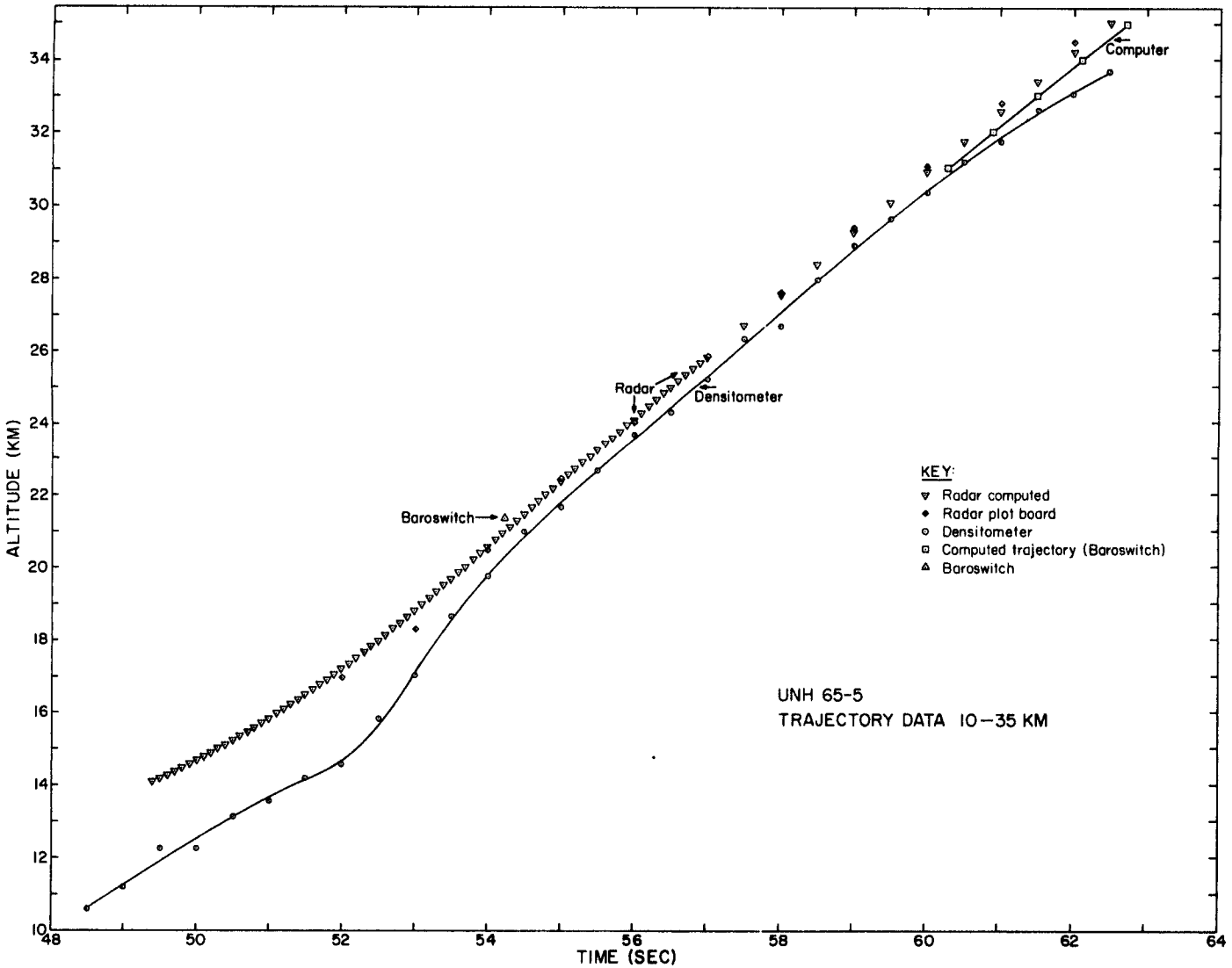
ALTITUDE (KM)
TIME (SEC)
Computer
Radar
Densitometer
Baroswitch
KEY:
Radar computed
Radar plot board
Densitometer
Computed trajectory (Baroswitch)
Baroswitch
UNH 65-5
TRAJECTORY DATA 10—35 KM

Figure A-1

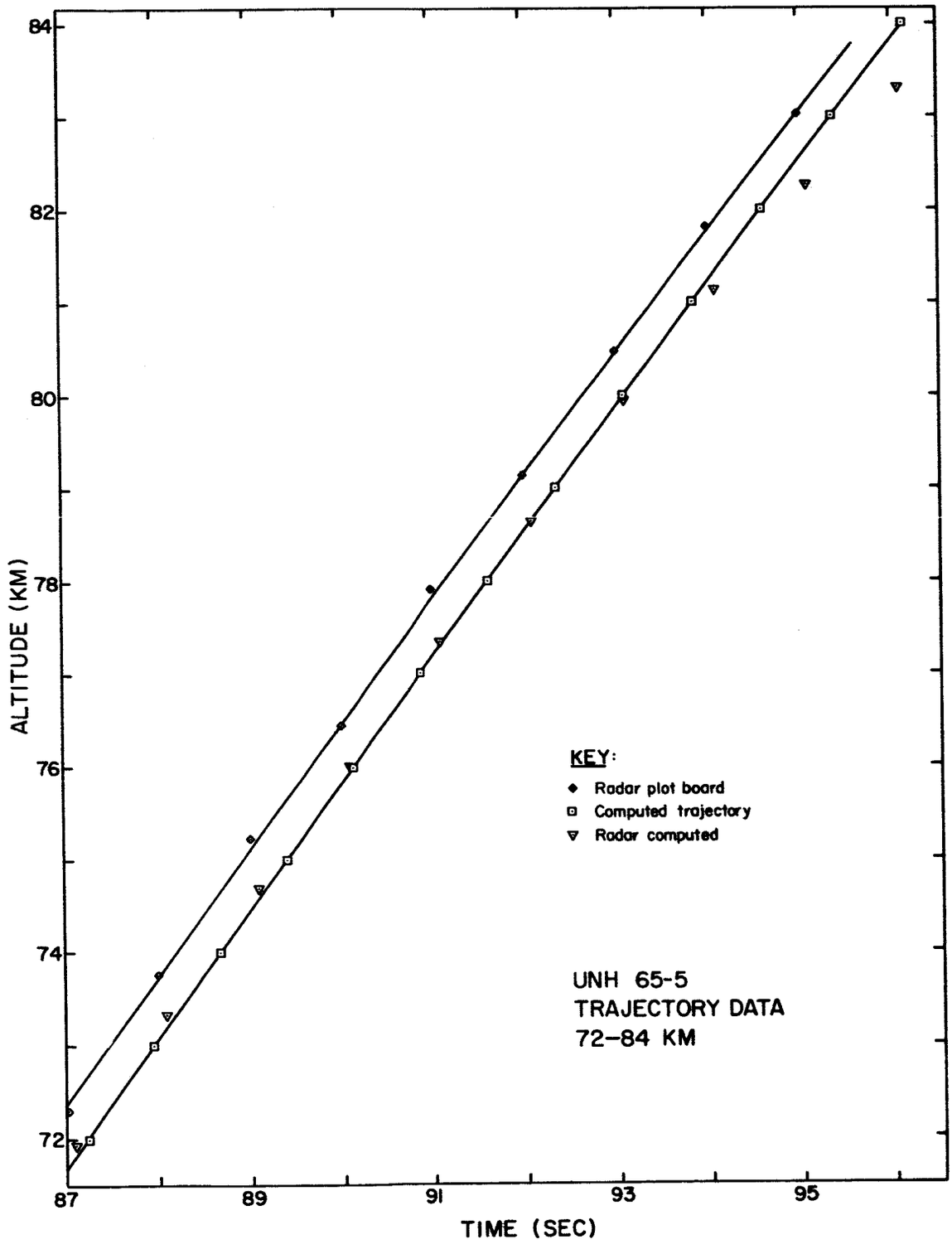
84
82
80
78
76
74
72
ALTITUDE (KM)
87
89
91
93
95
TIME (SEC)
KEY:
Radar plot board
Computed trajectory
Radar computed
UNH 65-5
TRAJECTORY DATA
72-84 KM

Figure A-2

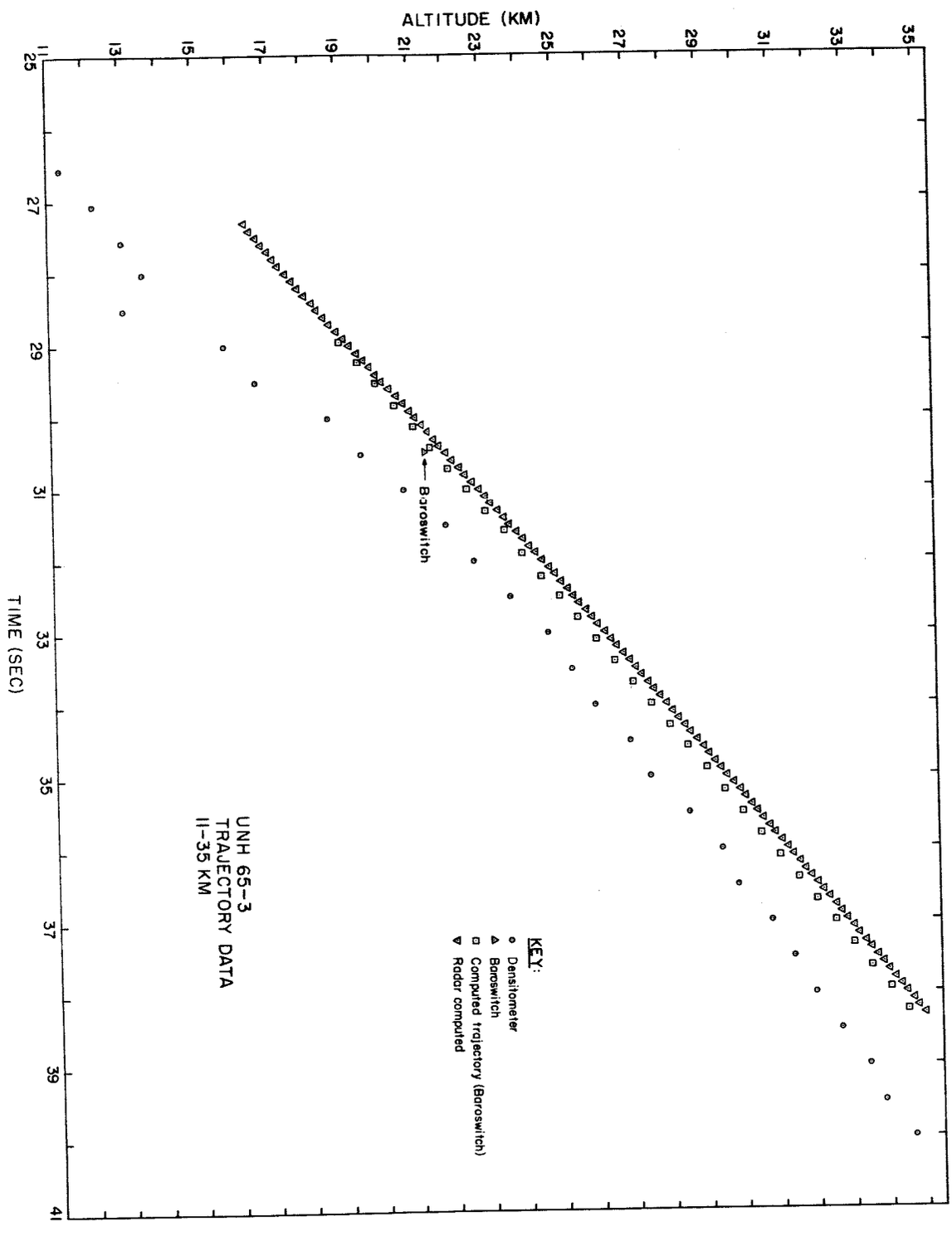
ALTITUDE (KM)
TIME (SEC)
Baroswitch
KEY:
Densitometer
Baroswitch
Computed trajectory (Baroswitch)
Radar computed
UNH 65-3
TRAJECTORY DATA
11-35 KM

Figure A-3